E.O. Paton Electric Welding Institute of the National Academy of Science of Ukraine
International Association “Welding”

The Paton Welding Journal

04
2024

International Scientific-Technical and Production Journal ♦ Founded in January 2000 (12 Issues Per Year)

EDITORIAL BOARD

Editor-in-Chief
Igor Krivtsun
E.O. Paton Electric Welding Institute of the NASU, Kyiv, Ukraine

Deputy Editor-in-Chief
Serhii Akhonin
E.O. Paton Electric Welding Institute of the NASU, Kyiv, Ukraine

Deputy Editor-in-Chief
Leonid Lobanov
E.O. Paton Electric Welding Institute of the NASU, Kyiv, Ukraine

Editorial Board Members

Olena Berdnikova
E.O. Paton Electric Welding Institute of the NASU, Kyiv, Ukraine
Yunlong Chang
School of Materials Science and Engineering, Shenyang University of Technology, China
Chunlin Dong
Guangzhou Jiao Tong University, China
Michael Gasik
Aalto University Foundation, Finland
Len Gelman
The University of Huddersfield, UK
Andrey Gumenyuk
Bundesanstalt für Materialforschung und –prüfung (BAM), Berlin, Germany
Jacob Kleiman
Integrity Testing Laboratory, Markham, Canada
Vitalii Knysh
E.O. Paton Electric Welding Institute of the NASU, Kyiv, Ukraine
Volodymyr Korzhyk
E.O. Paton Electric Welding Institute of the NASU, Kyiv, Ukraine
Victor Kvasnytskyi
NTUU «Igor Sikorsky Kyiv Polytechnic Institute», Ukraine
Eric Macdonald
The University of Texas at El Paso, USA
Serhiy Maksymov
E.O. Paton Electric Welding Institute of the NASU, Kyiv, Ukraine
Dhanesh G. Mohan
School of Engineering University of Sunderland England, United Kingdom
João Pedro Oliveira
Universidade NOVA de Lisboa, Portugal
Mykola Pashchin
E.O. Paton Electric Welding Institute of the NASU, Kyiv, Ukraine
Valeriy Pozniakov
E.O. Paton Electric Welding Institute of the NASU, Kyiv, Ukraine
Uwe Reisgen
Welding and Joining Institute, Aachen, Germany
Massimo Rogante
Rogante Engineering, Civitanova Marche, Italy
Cezary Senderowski
Mechanics and Printing Institute, Warsaw University of Technology, Poland
Magdalena Speicher
Kempten University of Applied Sciences, Germany
Mattias Thuvander
Chalmers University of Technology, Goteborg, Sweden
Valentyn Uchanin
Karpenko Physico-Mechanical Institute, Lviv, Ukraine
Yongqiang Yang
South China University of Technology, Guangzhou, China

Executive Editor
Oleksandr Zelnichenko
International Association “Welding”, Kyiv, Ukraine

Address of Editorial Office
E.O. Paton Electric Welding Institute, 11 Kazymyr Malevych Str., 03150, Kyiv, Ukraine
Tel./Fax: (38044) 205 23 90, E-mail: journal@paton.kiev.ua, patonpublishinghouse@gmail.com
https://patonpublishinghouse.com/eng/journals/tpwj

State Registration Certificate 24933-14873 ПР from 13.08.2021**,** ISSN 0957-798X, DOI: http://dx.doi.org/10.37434/tpwj
Subscriptions, 12 issues per year:
$384 — annual subscription for the printed (hard copy) version, air postage and packaging included;
$312 — annual subscription for the electronic version (sending issues in pdf format or providing access to IP addresses).

Representative Office of “The Paton Welding Journal”:

Bulgarian Welding Society
Address: Blvd. Asen Yordanov No.10, Sofia 1592, **BULGARIA**
Pavel Popgeorgiev, Tel: +359 899 96 22 20, E-mail: office@bws-bg.org

China-Ukraine Institute of Welding, Guangdong Academy of Sciences
Address: Room 210, No. 363 Changxing Road, Tianhe, Guangzhou, 510650, **CHINA**
Zhang Yupeng, Tel: +86-20-61086791, E-mail: patonjournal@gwi.gd.cn

PATON EUROPE Sp. z o. o.
Address: ul. Kapitałowa 4, 35-213, Rzeszów, **POLAND**
Anton Stepakhno, Tel: +38067 509 95 67, E-mail: Anton.Stepakhno@paton.ua

The content of the Journal includes articles received from authors from around the world in the field of welding, cutting, cladding, soldering, brazing, coating, 3D additive technologies, electrometallurgy, material science, NDT and selectively includes translations into English of articles from the following journals, published in Ukrainian:

- Automatic Welding (https://patonpublishinghouse.com/eng/journals/as);
- Electrometallurgy Today (https://patonpublishinghouse.com/eng/journals/sem);
- Technical Diagnostics & Nondestructive Testing (https://patonpublishinghouse.com/eng/journals/tdnk).

© E.O. Paton Electric Welding Institute of NASU, 2024
© International Association “Welding” (Publisher), 2024

CONTENTS

ORIGINAL ARTICLES

---

*Translated Article(s) from “Automatic Welding”, No. 2, 2024.

**Translated Article(s) from “Electrometallurgy Today”, No. 1, 2024.

***Translated Article(s) from “Technical Diagnostics & Nondestructive Testing”, No. 1, 2024.

****Translated Article(s) from “Technical Diagnostics & Nondestructive Testing”, No. 2, 2024.

DOI: https://doi.org/10.37434/tpwj2024.04.01

PARAMETERS AND CHALLENGES FOR RELIABLE HYDROGEN DETERMINATION IN WELDED JOINTS BY CARRIER GAS HOT EXTRACTION

M. Rhode[1,2], **T. Mente**[1], **T. Kannengiesser**[1,2]

[1]Bundesanstalt für Materialforschung und -prüfung (BAM),
Department 9 - Component Safety, Berlin, Germany
[2]Otto-von-Guericke-University, Institute for Materials Testing and Research, Magdeburg, Germany

ABSTRACT

For the hydrogen-based energy economy of tomorrow, the construction of the necessary infrastructure will play a central role. Most materials used to date, such as welded steels, can be prone to hydrogen embrittlement under certain conditions. This includes the classic delayed cold cracking during welding as well as degradation phenomena during service of components in hydrogen-containing environment. For the evaluation of any hydrogen effect, for example, on the mechanical properties of a welded metallic material, the hydrogen content must be precisely determined. In the case of weld seams, the carrier gas hot extraction (CGHE) according to ISO 3690 is meanwhile state-of-the-art. CGHE is based on accelerated hydrogen degassing due to the thermal activation of hydrogen at elevated temperatures. In addition to the quantification of hydrogen, thermal desorption analysis (TDA) with varying heating rates can be used to determine and evaluate the hydrogen trapping at microstructural defects in the material. For both techniques, experimental and metrological influences must be considered, which have a major effect on the result. For example, ISO 3690 suggests different sample geometries and minimum extraction times for CGHE. This study summarizes the results and experiences of numerous investigations at the Federal Institute for Materials Research and Testing (BAM) with different sample temperatures and geometries (ISO 3690 type B and cylindrical TDA samples) regarding the influence of the sample surface (polished/welded), measurement accuracy depending on the sample volume and the insufficient monitoring of the effect of PI control on the extraction temperature. A deviating extraction temperature from the target temperature can significantly falsify the measurement results. Based on the results, methods are shown which allow the desired extraction temperature to be reached quickly without physically interfering with the measuring equipment. This serves to significantly improve the reliability of the hydrogen measurement through increased signal stability and accelerated hydrogen desorption. In general, an independent temperature measurement with dummy samples is recommended for the heating procedure of choice to exclude possible undesired temperature influences before the measurement. The methods described can be transferred directly to industrial applications.

KEYWORDS: welding, hydrogen measurement, carrier gas hot extraction, ISO 3690, thermal desorption analysis

HYDROGEN MEASUREMENT IN WELDED SAMPLES

For the hydrogen-based economy of tomorrow, the construction of the necessary infrastructure (encompassing transportation and storage) will play an important role. In that connection, joining and welding plays a central role in component manufacturing [1]. For example, the most pipeline materials in the (German) natural gas grid have recently been labeled “H2-ready” [2]. However, a key parameter of degradation by hydrogen, the effective local hydrogen concentration, is not typically quantified and evaluated. Knowledge of this concentration enables the practical evaluation of hydrogen absorption during production or operation. This is particularly important for the welding manufacturing of components, e.g. to avoid hydrogen-assisted cracking or embrittlement. For the determination of hydrogen in a weld seam, the ISO 3690 [3] is a widely applied standard or ANSI/AWS A4.3-93 [4]).

In accordance with reference [3], the mercury method (Hg) and two carrier gas-based methods, gas chromatography (GC) and hot extraction (HE), can be used. In GC and HE, a thermal conductivity detector (TCD) is used to quantify hydrogen. The Hg-method is discussed critically regarding health risks and environmental protection and is increasingly being replaced by GC or HE [5]. An additional disadvantage of the Hg-method is the time required for hydrogen collection which takes from 15 to 21 days. With the GC-method, the hydrogen from the welding sample is collected in a closed chamber at elevated temperatures. For this reason, the collection time can be reduced to a few hours [6]. The chamber is then purged with the carrier gas and the corresponding gas mixture is fed into the GC unit. The HE-method is based on the thermal activation of hydrogen atoms in the solid metallic and welded sample, which desorbs and recombines to molecular hydrogen and is collected in a chamber or transported with carrying medium as described in the next sub-section.

Carrier gas hot extraction (CGHE) is a special HE-method. It is characterized by a half-open hydrogen collection chamber that is accessible from one

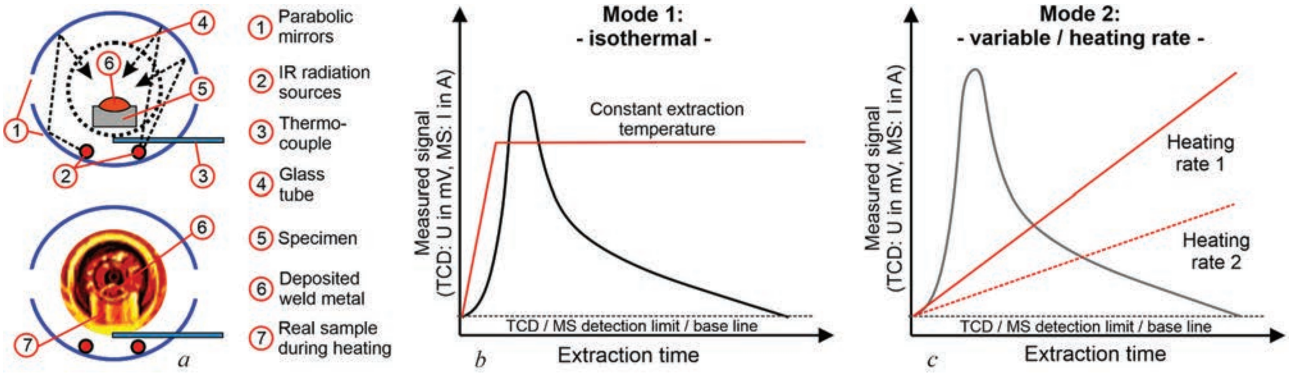

Figure 1. Carrier gas hot extraction: *a* — components and working principle of IR-furnace, in accordance with [7]; *b* — extraction mode 1: Isothermal HE; *c* — extraction mode 2: HE using variable temperatures/special case of constant heating rates

side only and is continuously purged with an inert carrier gas (e.g., nitrogen). This carrier gas stream transports the desorbed hydrogen to the analyzer. For this purpose, the application of a TCD is defined in ISO 3690 [3]. However, mass spectrometers (MS) are also used now in industrial applications, which offer significantly higher precision. Various heating methods are possible for the CGHE like infrared (IR) radiation, inductive heating, or resistance heating. IR-radiation offers the advantage that the sample can be heated without contact, as well as a wide range of adjustable extraction temperatures and times. Typically, the measured sample itself is not melted if welded samples are investigated [3, 4]. The basic components of the IR extraction system are shown in Figure 1, *a*. In principle, two operating modes are available, whereas in both cases, the absolute hydrogen concentration can be determined. Mode 1 is shown in Figure 1, *b*, it encompasses the so-called isothermal HE. This mode is useful for the determination of hydrogen transport data (such as diffusion coefficients) and temperature-dependent trapped hydrogen quantities as shown in [3, 5, 7, 8]. For this purpose, the temperature is kept isothermal during the measurement. Mode 2 is shown in Figure 1, *c*), it encompasses the HE with variable temperature programs. It is useful to identify the binding energy, the so-called activation energy, of hydrogen at distinct microstructural defects (traps) in the material. For this purpose, sufficiently low heating rates (typically < 0.5 K/s) are applied. The activation energy required to release the hydrogen from the traps is calculated from values obtained using thermal desorption analysis (TDA) [5, 8, 10]. The TDA is also being used more and more in an industrial context but is currently mostly focused on academic issues (characterization of hydrogen diffusion and trapping).

This study summarizes the results and experience of numerous investigations at the Bundesanstalt für Materialforschung und -prüfung (BAM) with different specimen temperatures and geometries (ISO 3690 type B and cylindrical TDA specimens) for welded samples. For a detailed description, references are given to suitable secondary literature at the relevant positions in this manuscript.

MATERIALS AND METHODS

MATERIALS

The creep-resistant steel T24 / /7CrMoVTiB10-10 and the high-strength structural steel S690Q were used for the investigations and welding experiments presented here. Table 1 briefly shows the chemical composition. Further details of the materials can be found in [7]. The chemical composition was determined from an average of five measurements using an optical spark emission spectrometer (from Spectro GmbH).

USED SAMPLE GEOMETRIES AND SPECIFIC HYDROGEN CHARGING CONDITIONS

The first sample geometry was a cylinder (machined from T24) with Ø = 3 mm, 20 mm length and ground surface, see Figure 2, *b*. Some samples were electrochemically charged with hydrogen. For this purpose, a 0.05 M H_2SO_4 acidic aqueous solution with addition of 12 mg/l $NaAsO_2$ (as recombination inhibitor) was used and various current densities (galvanostatic loading) were applied. After charging with hydrogen, the samples were stored in liquid nitrogen until

Table 1. Chemical composition of tested materials (in wt.%, Fe — balance)

Material	C	Cr	Mo	V	Ti	B	Al	Nb	Mn	Si	P+S
T24 / 7CrMoVTiB10-10	0.08	2.44	1.00	0.26	0.07	0.005	0.01	N/A*	0.52	0.25	< 0.01
S690Q	0.12	0.50	0.11	0.05	N/A*	N/A*	N/A*	0.01	1.52	0.40	< 0.02

*N/A — not available due to measurement uncertainties as impurification in respective steel grade.

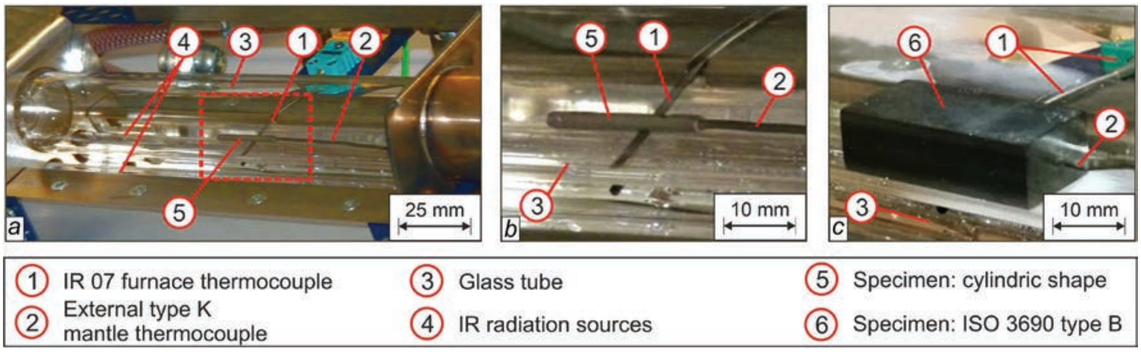

Figure 2. IR 07 furnace as part of G4 and G8 analyzer: *a* — sample position in glass chamber surrounded by IR furnace and magnified view with position of thermocouples inside center position; *b* — cylindrical TDA sample; *c* — ISO 3690 type B sample (taken and rearranged from [7], with permission and licensed by Springer Nature)

CGHE. The complete description of the experiment can be found in [8, 10].

The second specimen type was an ISO 3690 type B specimen (machined from S690Q) with dimensions of 30 mm length, 15 mm width and 10 mm thickness, see Figure 2, *c*. Two representative conditions were investigated to determine the influence of surface finish on temperature development during HE of the ISO Type B specimens: (1) polished/ground surface and (2) in the welded/oxidized condition. For welding, a metal active gas (MAG) welding process with M21 shielding gas (18 % CO_2/82 % Ar) and identical welding consumable was used. The aim of this study was to determine the temperature characteristics during the CGHE, not to determine potential material influences on the hydrogen concentration. However, to maintain realistic conditions, the samples were quenched after welding and stored in liquid nitrogen. For further details on test procedure, we refer to reference [3] and for detailed test results to reference [7].

HYDROGEN AND TEMPERATURE MEASUREMENT

The CGHE analyzer G4 PHOENIX with TCD was used for the hydrogen determination. For some experiments, a G8 GALILEO (both from Bruker AXS, Germany) with coupled mass spectrometer ESD100 (InProcess Instruments, Germany) was also used. The advantage of both analyzers is that the same IR furnace type (IR07) is used for the HE. For comparison and precision of the measuring methods, we refer to reference [9]. Figure 2, *a* shows the IR-furnace, with the dashed square indicating the position of the sample during extraction. The center of the longitudinal axis of the sample should always be positioned above the furnace thermocouple. Calibration or dummy samples were used to determine the exact sample temperature. These had identical surface properties and geometry as the later samples for hydrogen measurement. This separation is necessary because an in-situ temperature measurement directly on the sample could falsify the hydrogen content (hydrogen in the thermowire, moist coating, etc.). The cylindrical samples used for the TDA are shown in Figure 2, *b* and the ISO 390 type B sample in Figure 2, *c*. Detailed information on specimen selection and temperature measurement can be found in the reference [7, 8]. As shown in Figure 2, *b* and *c*, an additional blind hole was drilled in the center of the test specimens, into which a type K mantle-thermocouple was inserted. This external thermocouple ensured an independent temperature measurement of the sample bulk temperature and was compared with the adjusted/real furnace temperature. In the case of the ISO 3690 type B specimen, the measurements were taken in the center of the specimen to ensure that the bulk temperature was recorded and not the surface temperature (in case of the isothermal mode 1).

RESULTS

INFLUENCE OF SAMPLE SIZE AND GEOMETRY

In addition to the sample geometry, the sample surface and the ratio to the volume have a significant influence on the extraction temperature or the time to reach the respective temperature. The reason is that the IR-radiation is absorbed at the sample surface. The heating of the material happens due to the heat conduction into the bulk material. For that reason, the temperature change of the sample is primarily influenced by the thermal conductivity coefficient λ (in W/m·K) and the thickness of the sample. Figure 3, a shows the ISO 3690 type B and cylinder sample with their heating behavior to 200 and 400 °C respectively (original data shown in references [7, 8]. The desired isothermal extraction temperature (labeled as "furnace)" at the specified temperature is also shown as a comparative value. Of course, smaller samples (such as the cylinders with 3 mm diameter) heat-up faster compared to thicker samples (like the ISO 3690 type B with 10 mm in our case). This applies to both mode 1 "isothermal" and 2 "variable temperature".

Especially for the TDA (using mode 2), an accelerated heating of the sample (i.e., minimizing the tem-

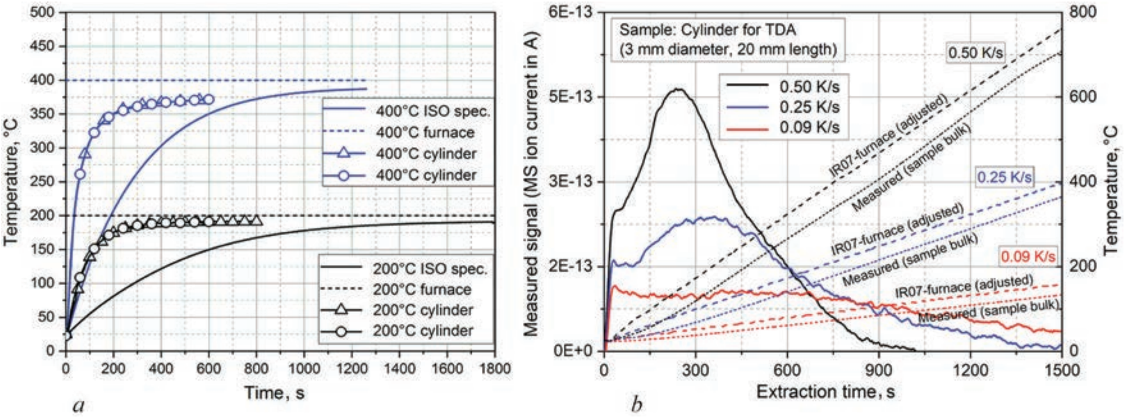

Figure 3. Heating behavior of sample for: a) mode 1 "isothermal holding" for various sample dimensions (taken from reference [7], with permission and licensed by Springer Nature), b) mode 2: measured signal (MS ion current in A) vs. heating rate and deviation between adjusted and measured sample temperature (cylindrical TDA samples), based on [10]

perature gradient in the sample) plays an essential role for reliable desorption curves, see Figure 3, *b*. If the sample temperature is incorrectly assigned, the calculated activation energy can be misleading regarding the share of "diffusible" and "trapped" hydrogen. For example, trapped hydrogen can be detected in low-alloy steels above 100 °C [10]. Only by correctly measuring the temperature directly in or at the sample (i.e., not by an idealized linear heating rate), a realistic activation energy can be calculated. This demonstrates the necessity of using the exact extraction temperature in the sample during the CGHE experiments. This is achieved by previous calibration samples (see Figure 2) without active hydrogen measurement, using the same extraction time-temperature cycle.

INFLUENCE OF SAMPLE SURFACE CONDITION

Figure 4 shows three measured temperature curves of ground (polished) and oxidized ISO 3690 type B samples for a target extraction temperature of 400 °C (according to mode 1). The polished surface ensured a significant delay in the heating. In this condition, the sample only reaches 350 °C after 1,000 to 1,200 s compared to the oxidized sample with 600 to 620 s. The reason is the different reflectivity (polished steel: 0.1 vs. oxidized: 0.7 to 0.9 in accordance with reference [11]. This means that a polished surface reflects 90 % of the total radiation energy and just 10 % are absorbed, whereas an oxidized surface reflects 10 % to 30 % and absorbs 90 % to 70 %! At constant power level of the IR-radiation emitting furnace, the oxidized sample is therefore heated much faster. Any temperature evaluation of CGHE samples must therefore always be carried out with the identical surface condition that the sample has before the measurement (e.g., oxidized condition for a representative welded ISO 3690 sample or blank metal after electrochemical hydrogen charging). It is therefore generally recommended to carry out an independent temperature measurement by use of the already mentioned calibration or dummy samples (see Sect. 3.1 and shown in Figure 2, *b* and Figure 2, *c*), if economically justifiable.

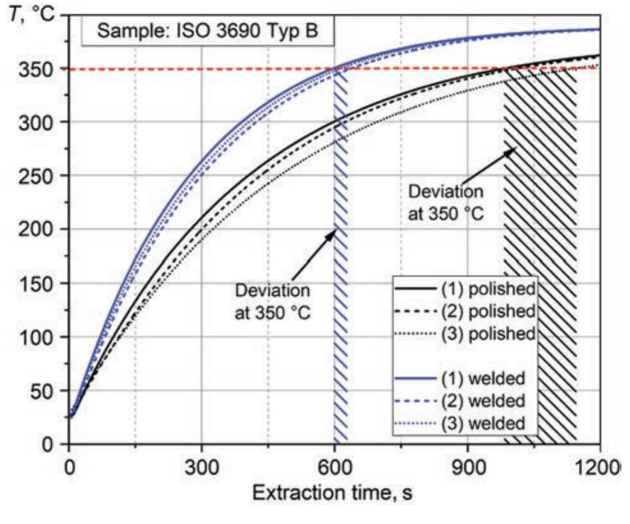

Figure 4. Real heating behavior for mode 1: comparison of a highly reflective and real (oxidized) surface for ISO 3690 type-B sample, targeted extraction temperature 400 °C, (scheme in accordance to [7])

EFFECT OF FURNACE CONTROLLER SETTINGS ON TARGETED TEMPERATURE

The heating process of the sample can be "accelerated" somewhat by changing the heating and preheating settings of the IR07 furnace. The effective controller is of the PID type, whereby the P-component has the greatest effect on the temperature increase. However, this can only be understood in conjunction with the sample geometry. Large samples in relation to the furnace volume, such as ISO 3690 type B, i.e. large sample volumes to be heated, heat up differently compared to the smaller "cylindrical" samples (see Figure 1, *b* and *c*). These react almost instantaneously to temperature changes specified by the heating program, e.g. for mode 1 (isothermal HE) presented in [7, 8] and for mode 2 (variable temperature program/TDA) in reference [10]. It is therefore not expedient

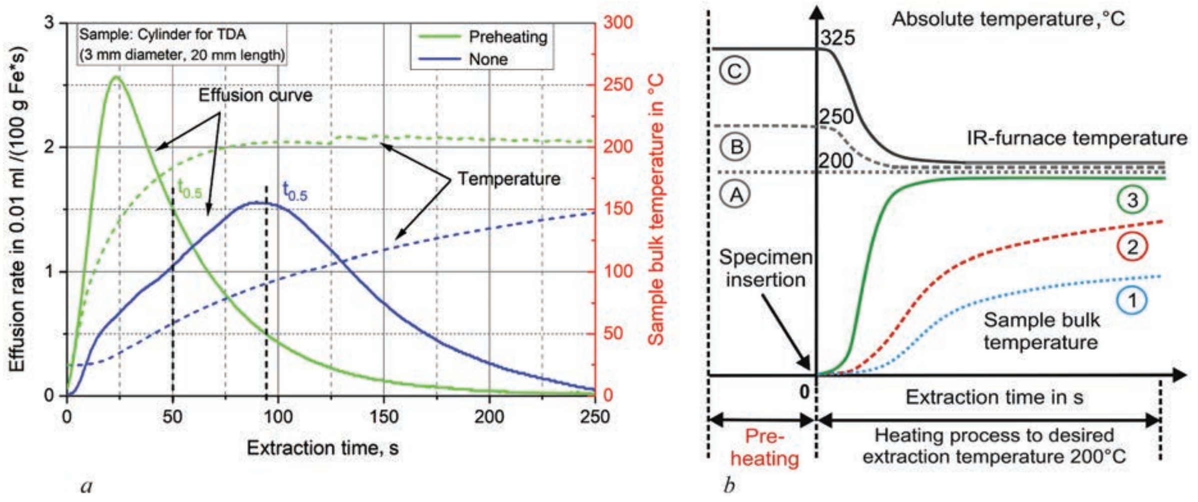

Figure 5. Accelerated sample heating for mode 1: *a* — effect of preheating on effusion curve and time "$t_{0.5}$" after 50 % of the hydrogen is effused from the sample for indented isothermal holding at 200 °C (cylindrical sample), in accordance with [7, 12]; *b* — schematic representation of furnace preheating before sample insertion on effective sample bulk temperature, in accordance with [8]

to recommend "optimum" controller settings. In addition, the temperature of the sample is ALWAYS below the set one and adjusted targeted extraction temperature of the furnace. The effect on the heating profile of the respective sample geometry should therefore always be checked a-priori using dummy samples. As a best practice recommendation, the desired maximum extraction temperature should be selected 20 K higher. Nevertheless, the ISO 3690 specifies binding minimum extraction temperatures for certain extraction times, but the interpretation is ultimately left to the user. From the point of view of measurement accuracy, a possible difference in the maximum temperature is a matter of interpretation, especially at high temperatures.

EFFECT OF ACCELERATED THERMOSTATING OF IR-FURNACE BY "PREHEATING" ON SAMPLE BULK TEMPERATURE AND CORRESPONDING HYDROGEN EFFUSION

Figure 5, *a* clearly shows the practical effect of an accelerated heating in mode 1. The measured signal rises much faster in the case of an optimized heating. Figure 5, *b* exemplarily shows the optimized curve no. "3" (green solid line) compared to the conventional heating procedure shown in curve no. "1" (blue dotted curve) using a preheating concept for the IR-furnace. It is obvious that the sample shows a significantly faster heating. This behavior is particularly important for further considerations of diffusion coefficients. For their calculation, the time "$t_{0.5}$" is used as standard, at which 50 % of the hydrogen has been extracted from the sample, i.e. 50 % of the respective area of the effusion curve [7, 8, 12]. Using fast heating, the "$t_{0.5}$" is reached after approx. 50 s at 180 °C, whereas with slow heating it is only reached after at approximately 90 s at 95 °C! This means two things: (1) any calculated diffusion coefficient differs significantly as both "$t_{0.5}$" — times differ by factor 2) and (2) the temperature assignment itself would be already incorrect. In any case, accelerated heating is therefore essential to reach the desired extraction temperature. In addition to the controller settings described in Sect. 3.3, this can be achieved very easily by setting a certain preheating temperature of the furnace in advance to the sample insertion. The principle for accelerated heating to different isothermal extraction temperatures is shown in Figure 5, *b*. For this purpose, the IR07 furnace is preheated to higher temperature than for the hydrogen extraction needed. From the moment the sample is inserted, the IR-furnace temperature drops freely as an exponential function in accordance with the thermodynamic inertia of the "furnace with sample" system. As a result, considerably more energy is available for the sample, as the furnace itself must not be additionally heated up during the isothermal hydrogen extraction. Further details were presented e.g. in [7, 8, 12].

CALCULATION OF RELIABLE HYDROGEN CONCENTRATIONS WITH AUTOMATED SOFTWARE SETTINGS

Typically, the total hydrogen concentration is calculated by the integrated measured signal over time (e.g., in mV for the TCD or in A as ion current for the MS) using a calibration factor and related to a certain sample mass. The most frequently used unit is "ml/100 g Fe". This means a certain volume of hydrogen dissolved in a virtual deposited metal of 100 g. An essential factor for reliable measurements is the human being in terms of literally "blind trust" in automatically generated values. This applies regardless of the manufacturer. The extraction time and the temperature program for mode 1 or 2 are usually set by

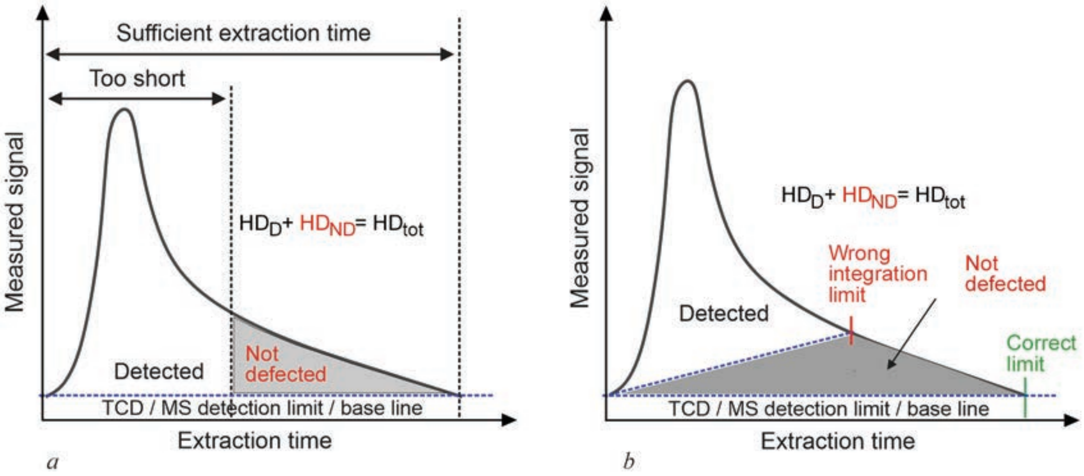

Figure 6. Possible errors when evaluating the measurement signal: *a* — extraction time selected too short; *b* — incorrect settings for integration limits or insufficient knowledge of signal switch-off threshold, see [7]

humans, but the total hydrogen concentration “HD_{tot}” is usually calculated automatically (by the respective controller software). Two effects can occur here:

At first, an insufficient extraction time (e.g., using mode 1). This is usually the case if the hydrogen measurement is carried out with a maximum pre-set holding time, for example in accordance with ISO 3690 [3] as shown in Figure 6, *a*. In the case of 400 °C, an extraction time of 21 minutes is recommended in the standard. If this time is set as the maximum extraction time or the measurement is aborted before the total hydrogen “HD_{tot}” effused from the sample, this results in an error due to the “not detected” hydrogen (gray shaded area and labeled as “HD_{ND}”). In addition, only a sufficient extraction time duration at the desired temperature ensures that the total hydrogen “HD_{tot}” can desorb from the sample and be measured by either TCD, MS or others.

Secondly, the determination of “HD_{tot}” is mostly based on the pre-set start and end points (by certain signal cut-off thresholds) to automatically calculate the detected hydrogen. The baseline is usually set by the software itself, based on the lower signal integration limits (in the case of a TCD, set as the mV threshold value in the control software). This cut-off limit is the most important limit for the integration limit of the signal, i.e. the amount of hydrogen extracted from the sample. This is particularly the case for long desorption/extraction times with a low signal-to-noise ratio. For very long measurements/very low hydrogen effusion rates, the hydrogen detector (TCD or MS) is virtually operated at the detection limit. It is always advisable to check the measurement curves afterwards manually and ensure that the integration limits are set precisely. Especially for small amounts of hydrogen dissolved in small samples, it may be recommended to switch to a measuring system with higher precision such as a MS. As shown in Figure 6a, errors in the evaluation (i.e., underestimation of the calculated “HD_{tot}”) may otherwise occur. In this case, a part of the hydrogen quantity present in the sample would not be detected (gray shaded area “HD_{ND}” in Figure 6, *b*). This was also the subject of controversial discussions at a regular review of ISO 3690 [13, 14]. For further details on these extreme cases discussed in this sections (including the assessment of signal quality) can be found in the references [7, 8].

CONCLUSIONS FOR A RELIABLE HYDROGEN DETERMINATION VIA CGHE

The following chapter briefly summarizes the results described. It is important to note that additional special metrological specifics apply when using an IR furnace for extraction. These are:

The IR radiation is absorbed at the sample surface. This process depends strongly on the surface conditions of the sample, i.e. polished/ground or oxidized and is expressed by the absorption or emission coefficient.

At constant power of the radiation source, a larger proportion of reflected radiation leads to delayed heating of the sample to the desired extraction temperature. This effect intensifies with greater thickness. The measurement time required for hydrogen extraction is therefore directly linked to the heating behavior of the sample to the desired temperature.

The sample is heated exclusively by heat conduction from the surface to the interior, which is characterized by the specific thermal conductivity. This means that there is ALWAYS a temperature deviation between the set furnace temperature and the temperature of the sample due to the system. For a pure hydrogen determination according to mode 1, this behavior is secondary, but for the evaluation of the diffusion behavior mode 2 is essential.

Materials with higher thermal conductivity (such as copper) could be heated faster compared

Table 2. Experimental and analyzer influence on hydrogen detection and countermeasures for limitation

Influence	Effect	Countermeasure
Sample geometry	● "Thermodynamic inertia" → maximum IR-furnace power limits the heating efficiency of the samples ● Thicker samples require prolonged time for heating to elevated temperature	● Mode 2: Prefer thinner samples for TDA ● Use of dummy samples and recording of temperature development ● Restriction to „known geometries, e.g. according to ISO 3690
Sample surface	● IR radiation is absorbed at sample surface ● Heating of bulk via heat conduction → delay and temperature gradient ● Blank metal surfaces heat up slowly ● Highly reflective materials have a limited suitabiltiy for application of CGHE	● Adjust surface to the desired heating mode ● Application of mode 1: Determination of hydrogen concentration (e.g., according to ISO 3690) or diffusion coefficients ● Application of mode 2: Electrochemical and/or pressurized hydrogen-loaded samples ● Consideration of the influence especially for TDA (temperature offset) ● Use of dummy samples and recording of temperature development (determination of temperature off-set)
Temperature monitoring	● Difference of sample bulk and surface temperature ● Occurrence of unavoidable but limitable temperature gradient	● Sample position in extraction chamber should be identical with IR-furnace thermocouple ● Use of dummy samples ● Recording of temperature profiles (determination of temperature offset)
Settings of PID-controller	● Consideration of the heating behavior of the samples and effect on ex-traction behavior	● „Calibration" of representative temperature curves and optimization of the setting values ● „Preheating" of IR-furnace to accelerate sample heating
Quantitative measurement	● Precision of the measuring system vs. effusion rate ● Consideration of signal stability (signal-to-noise ratio) TCD vs. MS	● MS enables use of smaller sample geometries and weight ● Better measurement resolution and sensitivity
Hydrogen concentration	● Observing the signal thresholds ● Correct setting of integration limits	● Critical assessment of results ("visual inspection" of measured values)

Table 3. Material effect on hydrogen detection and countermeasures for limitation

Influence	Effect	Countermeasure
Micro-structure	● Austenite with increased hydrogen solubility compared to Ferrite ● Diffusion in Austenite decreased	● Variation of extraction time necessary ● Avoidance of underestimation of hydrogen concentration → Consideration of dummy samples ● In case of unknown materials → "Trial and error"
Chemical composition	● "The more complex the alloy, the more complex the hydrogen trapping…" ● Shift of desorption temperatures/time ● "Unknown" materials require special attention	● Variation of extraction time necessary ● Consideration of dummy samples ● In case of unknown materials → "Trial and error"

to iron or steel, but the high reflectivity is usually in contrast to this.

The effect of reaching the isothermal extraction temperature over time (mode 1) is of secondary interest if the extraction time is sufficiently long (i.e., only determination of the water content is of interest). As already mentioned, the temporal interpretation of the heating behavior (and thus the correct temperature assignment) in mode 2 is essential. This is the only way to correctly calculate the activation energy of the hydrogen traps via the TDA. The facts described above provide options for influencing the HE without having to physically intervene in the process. Table 2 briefly presents the main influences presented in Sect. 3.1 to 3.5 and derives measures to limit them (shown in bold).

The countermeasures presented in Table 2 allow the desired extraction temperature to be reached without physically interfering with the measuring equipment. They can be directly transferred to industrial applications by adapting the software of the analyzer (further details can be found in [7, 8]). Table 3 gives additional examples of issues to be considered when comparing different metallic materials or processing conditions. Especially, "new" or unknown materials require special attention [15].

ACKNOWLEDGEMENT

We thank Dr.-Ing. C. Münster und Mrs. S. Groth, who had a big share in conducting the underlying and evaluated welding and temperature measurement experiments.

REFERENCES

1. Rhode, M., Kannengießer, T. (2021) *Fügetechnik für die Wasserstoffökonomie - Werkstoffe, Schweißtechnologien, Perspektiven*. In: DVS-Berichte 373. DVS-Media GmbH, Düsseldorf.
2. Steiner, D., Marewski, U. et al. (2023) *DVGW-Project SyWeSt H2 – Final report*. Study funded by DVGW e.V. https://www.dvgw.de/medien/dvgw/forschung/berichte/g202006-sywesth2-staehle.pdf
3. ISO 3690:2018: *Welding and allied processes — Determination of hydrogen content in arc weld metal*.
4. ANSI/AWS A4.3-93:2006: *Standard methods for determination of the diffusible hydrogen content of martensitic, bainitic, and ferritic steel weld metal produced by arc welding*.
5. Padhy, G.K., Komizo, Y.I. (2013) Diffusible hydrogen in steel weldments — a status review. *Transact. of the Japanese Welding Research Institute*, **1**, 39–62.
6. Jenkins, N., Hart, P.H.M. et al. (1997) An evaluation of rapid methods for diffusible weld hydrogen. *Welding J*. 76(**1**), 1s–10s.
7. Rhode, M., Schaupp, T. et al. (2019) Hydrogen determination in welded specimens by carrier gas hot extraction — a review on the main parameters and their effects on hydrogen measurement. *Welding in the World*, **63**, 511–526.
8. Rhode, M. (2016) *Hydrogen diffusion and effect on degradation in welded microstructures of creep-resistant low-alloyed steels*: BAM-Dissertationsreihe 148, Berlin.
9. Salmi, S., Rhode, M. et al. (2015) Hydrogen determination in 22MnB5 steel grade by use of carrier gas hot extraction technique. *Welding in the World*, **59**, 137–144.
10. Rhode, M., Mente, T. et al. (2018) Hydrogen trapping in T24 Cr–Mo–V steel weld joints — microstructure effect vs. experimental influence on activation energy for diffusion. *Welding in the World*, **62**, 277–287.
11. N.N. (2023) Emission coefficients of different materials, accessed on 2023-05-18. http://www.scigiene.com/pdfs/428_InfraredThermometerEmissivitytablesrev.pdf
12. Rhode, M., Muenster, C. et al. (2017) Influence of experimental conditions and calculation method on hydrogen diffusion coefficient evaluation at elevated temperatures. In: *Proc. of Inter. Hydrogen Conf. (IHC 2016) on Materials Performance in Hydrogen Environments*. Eds by B.P. Somerday, P. Sofronis. ASME Press, 495–503.
13. (2017) ISO/DIS 3690: Result and Comment. IIW-Doc. II-E-760-18: Intermediate Meeting of IIW Commission II-E, Genua, Italy.
14. (2017) Comments on ISO/DIS 3690 by Japan Welding Engineering Society. IIW-Doc. II-E-750-17: Intermediate Meeting of IIW Commission II-E, Genua, Italy.
15. Rhode, M., Nietzke, J. et al. (2022) Hydrogen diffusion and desorption characteristics of a CoCrFeMnNi high entropy and a CoCrNi medium entropy alloy. In: *Proc. of 4th Inter. Conf. on Steel and Hydrogen*. Pap. H03, 11 pages. Ed. by Duprez L. OCAS, Ghent, Belgium.

ORCID

M. Rhode: 0000-0003-4490-4688,
T. Mente: 0009-0007-8325-9657

CONFLICT OF INTEREST

The Authors declare no conflict of interest

CORRESPONDING AUTHOR

M. Rhode
Bundesanstalt für Materialforschung und -prüfung (BAM), Department 9 - Component Safety,
Berlin, Germany
E-mail: michael.rhode@bam.de

SUGGESTED CITATION

M. Rhode, T. Mente, T. Kannengiesser (2024) Parameters and challenges for reliable hydrogen determination in welded joints by carrier gas hot extraction. *The Paton Welding J*., **4**, 3–10.

JOURNAL HOME PAGE

https://patonpublishinghouse.com/eng/journals/tpwj

Received: 14.03.2024
Received in revised form: 09.04.2024
Accepted: 13.05.2024

DOI: https://doi.org/10.37434/tpwj2024.04.02

COMPUTATIONAL EVALUATION OF THE INFLUENCE OF THE THICKNESS OF WELDED JOINTS OF AMg6 ALLOY ON THEIR STRESS-STRAIN STATE AFTER ELECTRODYNAMIC TREATMENT IN THE PROCESS OF WELDING

L.M. Lobanov[1], **M.O. Pashchyn**[1], **O.L. Mikhodui**[1], **N.L. Todorovych**[1],
Yu.M. Sydorenko[2], **P.R. Ustymenko**[2]

[1]E.O. Paton Electric Welding Institute of the NASU
11 Kazymyr Malevych Str., 03150, Kyiv, Ukraine
[2]National Technical University of Ukraine “Igor Sikorsky Kyiv Polytechnic Institute”
37 Prospect Beresteiskyi (former Peremohy), 03056, Kyiv, Ukraine

ABSTRACT

A calculated evaluation of the efficiency of electrodynamic treatment (EDT) effect on the stress state of butt-welded joints of plates of aluminium AMg6 alloy with an increase in their thickness δ was carried out. Mathematical modelling of the kinetics and residual stress states of butt-welded joints δ = 2, 4 and 8 mm was carried out as a result of their EDT at different values of temperature T of the plates, at which the treatment was performed. The value of the vertical velocity V_0 of the electrode-indenter (EDT tool) was taken as V_0 = 5 m/s, which corresponds to the modern electrophysical characteristics of the equipment for EDT. The values of T were set reflecting the conditions of EDT after welding (T = 20°C) and during fusion welding (T = 150 and 300 °C). The problem was solved in a three-dimensional formulation using the ANSYS softare. The conditions for the formation of stresses in the plates at EDT after and during welding were determined by the mechanical characteristics of AMg6 alloy at temperatures T = 20, 150, and 300 °C without taking cooling into account. The results of the computation of residual stresses in welded joints are presented. It is shown that at a value of T = 150 °C, EDT provides the most optimal residual stress states of the plates in the entire experimental range of δ. It was proved that EDT in the welding process (at T = 150 °C) is more efficient compared to EDT of metal after cooling (T = 20 °C). It was established that at EDT of welded joints δ = 2–4 mm, residual compressive stresses are formed over the entire thickness of the plates, the values of which are close to the yield strength of AMg6 alloy. At EDT of welded joints δ = 8 mm, residual compressive stresses are formed on the outer surface of the plates, and on the back side — tensile ones.

KEYWORDS: electrodynamic treatment, residual welding stresses, aluminium alloy, electric current pulse, shock interaction, finite element model, electrode-indenter, theory of elastic-plastic flow, fusion welding

INTRODUCTION

Residual stresses have a negative impact on the life and corrosion resistance of welded structures of aluminium-based alloys, thereby reducing their service life. In the world practice, an increase in the volumes of manufacturing of such structures is observed, which replace high-strength steel products. Considering the abovementioned, the problem of reducing residual tensile stresses or forming compression stresses in welded joints of aluminium-based alloys is relevant. Traditional technologies for control of residual stress state (RSS) require the use of metal-intensive tooling and/or significant energy consumption and do not always meet the requirements of modern engineering practice [1, 2], which requires innovative energy-saving approaches to production.

RESEARCH RELEVANCE

Electrodynamic treatment (EDT) of welded joints with electric current pulses is an innovative approach to controlling RSS of welded structures based on the use of pulsed electromagnetic fields and their derivatives [3–6].

It has been proved that preheating of the electric pulse effect zone to a temperature T stimulates RSS relaxation mechanisms [7]. This contributes to the development of technologies for the use of EDT in combination with the welding process. It has been experimentally proved that the implementation of EDT at elevated T during welding contributes to more intensive RSS relaxation as a result of EDT compared to the treatment of weld metal at room T [8].

However, the electrophysical characteristics of the existing EDT equipment provide the value of the stored energy E_C (the value of E_C is the defining characteristic of EDT efficiency) of the capacitive storage C, which does not exceed 1.0 kJ. This predetermines the evaluation of the boundary capabilities of EDT application as a means of effective influence on RSS of welded structures. As is known from the results of previous experimental studies, the effectiveness of

EDT decreases with an increase in the thickness δ of the metal to be treated [9]. Until now, no theoretical evaluation of the effect of δ of welded joints on EDT efficiency has been carried out, including when treating metal at different T values, to which the metal is heated during welding. The results of such studies allow determining the maximum boundary δ of welded joints within which EDT is an effective RSS regulator with the existing capabilities of EDT equipment, i.e., at the condition $E_C \leq 1$ kJ, which corresponds to the kinetic energy of the electrode-indenter at a velocity of up to 5 m/s. The way to solve the problem is the mathematical modelling, first of all, of the dynamic (shock) component of EDT to determine the effect of different δ of welded joints on RSS after their EDT during and after welding. This should facilitate the optimization of the EDT technology by determining the boundary capabilities of its application for effective RSS control of welded joints.

The aim of the study is the computational evaluation of the influence of the thickness of welded joints on their RSS as a result of treatment of metal by shock EDT component after and during welding (at elevated temperatures).

PROCEDURE AND COMPUTATIONAL SCHEME OF THE PROBLEM

The object of research is the process of numerical computation of SSS of model welded joints as a result of shock treatment as a component of EDT under conditions of elevated temperatures, which was performed in a finite element formulation using the ANSYS/AUTODYN software [10] in an explicit form. A three-dimensional prismatic finite element SOLID 164 was used to build the finite element mesh (FEM) of the problem, and the modelling was performed with the use of a moving FEM, that was rigidly connected with the medium and deformed together with it. The computational scheme and boundary conditions of the problem regarding the process of shock interaction of the electrode-indenter with a plate, described in [8], are shown in Figure 1. The presence of the geometric symmetry of the dynamically interacting electrode *1* and plate *2* allows considering only their fourth part in the computational scheme with the limitation of bodies' displacements on the symmetry planes.

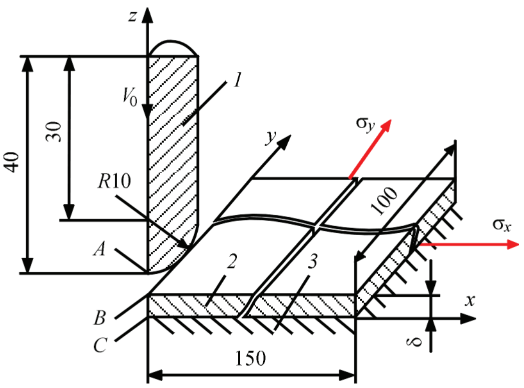

Figure 1. Computational diagram of the process of dynamic loading of the plate at EDT: *1* — electrode-indenter; *2* — treated specimen; *3* — absolutely rigid base; *A* — point on the outer surface of the electrode-indenter; *B* — point on the outer surface of the plate; *C* — point on the back surface of the plate; V_0 — velocity of the electrode-indenter movement [8]; *x*, *y*, *z* — coordinate axes

As the subject of the research, a model of a butt-welded joint of AMg6 alloy of the Al–Mg alloying system in the form of a plate preliminary stressed by uniform uniaxial tension was used. Residual welding stresses in the plate plane were modelled by setting the T value of the longitudinal tensile stress component σ_x (along the x-axis in Figure 1). Since the effect of EDT on the stress state of the treated plate is quite local in size, for example, not more than 10–15 mm, it can be assumed that in the zone of residual tensile stresses at EDT, these stresses can be taken as constant. The applied computational scheme is simplified, it does not reproduce the actual distribution of residual stresses in the welded joint, but requires the minimal computation time. Based on the results of comparing σ_x in the weld centre (in the contact interaction zone) after EDT at different T values, it is possible to select the temperature treatment mode that provides optimal residual stresses. The scheme for computation of the real stress distributions in the cross-section of a welded joint, taking into account the active zone – tension and reactive – compression zone, will be implemented in further studies.

In the mathematical formulation, the behaviour of the materials of the plate (aluminium AMg6 alloy) and the electrode-indenter (M1 copper) under the action of an external pulse load was described using an ideal elastic-plastic material model. This model in the materials library of the ANSYS/AUTODYN software is called PLASTIC-KINEMATIC [10]. The contact interaction was frictionless.

The interaction of the electrode-indenter with the plates of 300×200 mm and a thickness δ = 2, 4 and 8 mm was considered, which according to the accepted classification belong to thin-sheet structures [11].

The effect of temperature without taking the cooling of the model welded joint into account was described by changing such mechanical characteristics as modulus of elasticity E and yield strength σ_y of AMg6 alloy at temperatures $T = 150$ and 300 °C, where the choice of T values was justified in [8]. The modeling was also performed for $T = 20$ °C to compare the efficiency of EDT after and during welding. The values of residual welding stress component σ_x were respectively assumed to be equal to σ_y of AMg6 alloy at T = 20, 150, and 300 °C. The mechanical

Table 1. Mechanical characteristics of structural elements of the EDT model of AMg6 alloy in the welding process

Number	Structural element of the model	Material	Density ρ, kg/m^3	Poisson's ratio μ	*T*, °C	Modulus of elasticity *E*, GPa	Yield strength σ_y, MPa	Relative elongation δ, %
1	Plate of 300×200×2–8 mm	AMg6	2640	0.34	20	71	150	22
2					150	60	120	40
3					300	55	50	55
4	Electrode with a diameter of 15 mm	M1	8940	0.35	20	128	300	6

characteristics of metal materials used in the modelling at $T = 20$, 150, and 300 °C are given in Table 1.

The set *T* values correspond to the location of the electrode-indenter along the weld line at a distance L_{EDT} behind the welding heat source (Figure 2).

According to the results of previous experimental studies, it was found that the electrode-indenter obtained a value of $V_0 = 5$ m/s (at the condition $E_C = 1$ kJ), and its temperature during welding did not exceed 20 °C [8]. Therefore, the properties of the electrode-indenter during its contact interaction with the plate were set exclusively for $T = 20$ °C (Table 1).

MODELLING RESULTS AND THEIR DISCUSSION

As is known, σ_x component has a much greater influence on RSS of welded joints compared to σ_y [11]. As a result of modelling, the axonometric surfaces of the distribution of σ_x stress component (instantaneous stresses) across the metal thickness at the moment of completion of the contact interaction at $T = 20$, 150 and 300 °C of the electrode-indenter with a plate δ = 2 mm (Figure 3), δ = 4 mm (Figure 4) and δ = 8 mm (Figure 5) along the shock line (SL) at the points *B* and *C* (Figure 1), as well as on the *X* axis at a distance of 5 mm (Figure 3, *a*) from SL to evaluate the stress distribution along the center line of the weld.

Analysing the results of Figures 3–5 in general, it should be noted that after EDT at $T = 150$ and 300 °C, stresses are formed in the plates that slightly exceed the value of $\sigma_y = f(T)$ (Table 1). However, the mod-

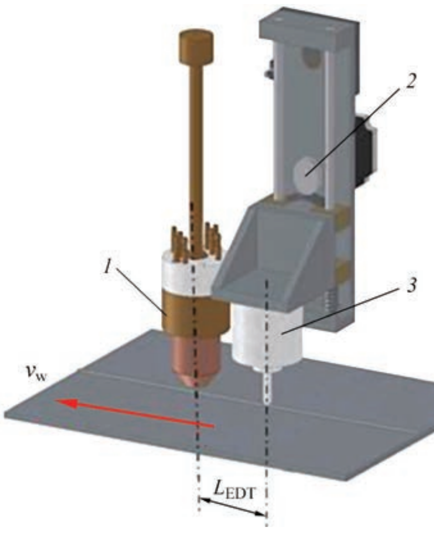

Figure 2. Scheme of EDT in the welding process, where V_w is the welding direction; *1* — welding torch; *2* — system for dynamic loading of EDT electrode; *3* — electrode device for EDT; L_{EDT} — distance between the axes of the electrodes for welding and EDT [8]

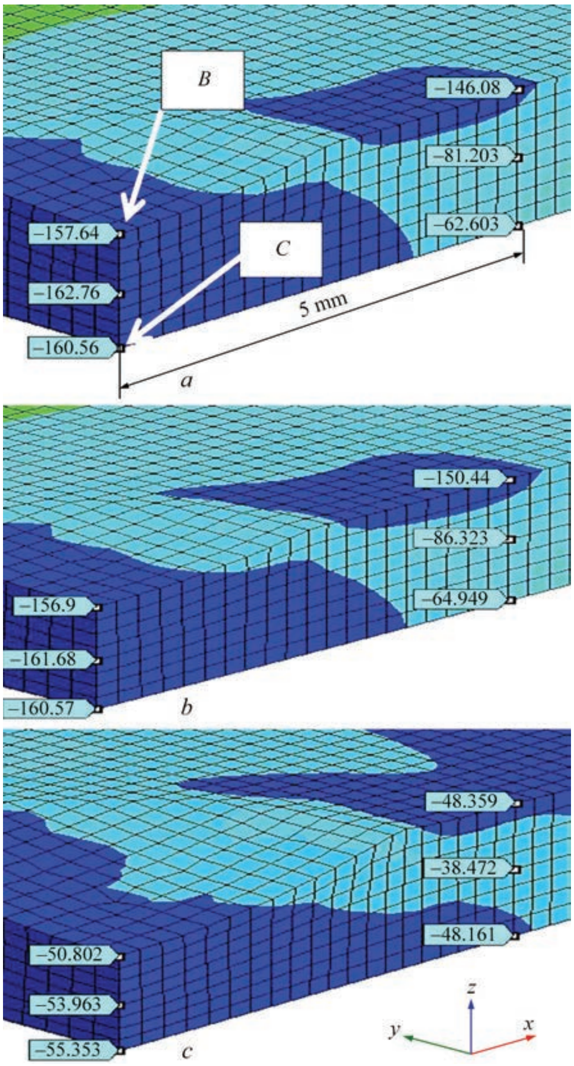

Figure 3. Instantaneous patterns of the distribution of values (MPa) of stress σ_x components in the plate of AMg6 alloy δ = 2 mm at the moment of completion of the EDT action along the shock line (SL) between the points *B* and *C* (Figure 2) and at a distance of 5 mm from the line *B–C*: *a* — σ_x at $T = 20$ °C; *b* — σ_x at $T = 150$ °C; *c* — σ_x at $T = 300$ °C

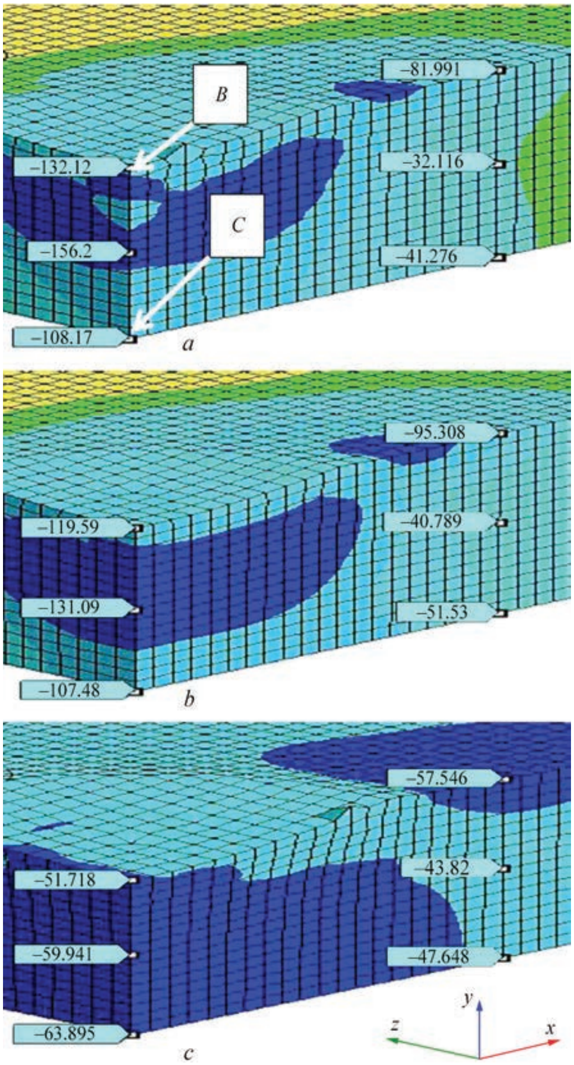

Figure 4. Instantaneous patterns of the calculated distribution of values (MPa) of stress σ_x components in the plate of AMg6 alloy $\delta = 4$ mm at the moment of completion of the EDT action along the shock line (SL) between the points *B* and *C* and at a distance of 5 mm from the line *B–C*: *a* — σ_x at $T = 20$ °C; *b* — σ_x at $T = 150$ °C; *c* — σ_x at $T = 300$ °C

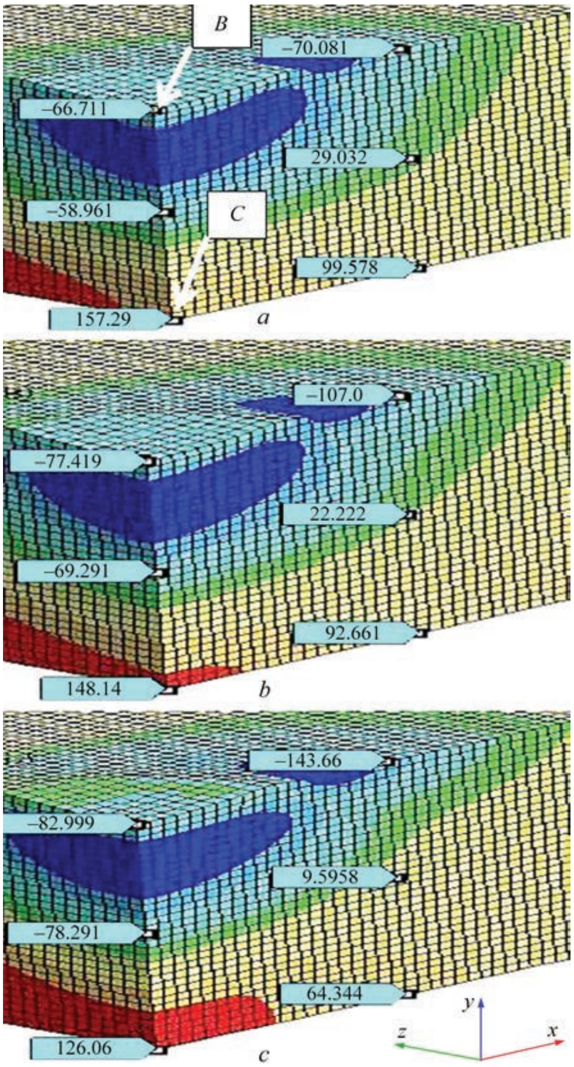

Figure 5. Instantaneous patterns of the calculated distribution of values (MPa) of stress σ_x, σ_y components in the plate of AMg6 alloy $\delta = 8$ mm at the moment of completion of the EDT action along the line between the points *B* and *C* (Figure 2) and at a distance of 5 mm from the line *B–C*: *a* — σ_x at $T = 20$ °C; *b* — σ_x at $T = 150$ °C; *c* — σ_x at $T = 300$ °C

elling results allow (in terms of quality) comparing RSS of plates $\delta = 2$–8 mm after EDT at different *T* and determining the optimal *T* value, at which the highest efficiency of EDT action on RSS of welded joints is achieved. The dominance of instantaneous compression σ_x stresses along SL in the entire considered range of δ and T can be seen. At a distance of 5 mm from SL, the pattern is slightly different. Thus, if for σ_x components in the range of $\delta = 2$–4 mm at all T values, compression stresses dominate, then for $\delta = 8$ mm, a change in the sign of stresses across the thickness of the plate from compression at the point *B* to tension at the point *C* is characteristic.

Figure 3 shows the results of computation of the instantaneous distributions of σ_x in the plates $\delta = 2$ mm. It can be seen that along SL, σ_x components are exclusively compression stresses on the contact (point *B*) and back (point *C*) surfaces of the plates. The values of stresses along SL reach $\sigma_y = f(T)$ for AMg6 alloy at $T = 20$ °C (Figure 3, *a*) and 300 °C (Figure 3, *c*) and grow to $1.3\sigma_y$ at 150 °C (Figure 3, *b*). At a distance of 5 mm from SL, the compression σ_x values decrease from σ_y on the outer surface to $0.4\sigma_y$ on the back one at $T = 20$ °C (Figure 3, *a*) from 1.25 to $0.5\sigma_y$ at $T = 150$ °C (Figure 3, *b*) and are close to σ_y at 300 °C on both surfaces (Figure 3, *c*).

Comparing the instantaneous distributions of σ_x component at $T = 20$, 150 and 300 °C, which is dominant during the formation of residual welding stresses, it should be noted that the optimal temperature for EDT is 150 °C, at which the maximum level of compression (instantaneous) stresses is achieved at the moment of completion of contact interaction.

Figure 4 shows the results of computation of the instantaneous distributions of σ_x in the plates $\delta = 4$ mm. It is possible to see some differences in stress distributions from the previous results ($\delta = 2$ mm), which are associated with an increase in the thickness of the treated plates. Thus, along SL and at a distance of 5 mm from it, the values of σ_x compression are generally lower than at $\delta = 2$ mm.

The components of compression σ_x along SL (from the point *B* to the point *C*) reach the values respectively from $0.9\sigma_y$ to $0.7\sigma_y$ for AMg6 alloy at $T = 20$ °C (Figure 4, *a*), $1.1\sigma_y$ at 150 °C (Figure 4, *c*, *d*), i.e., lower than for $\delta = 2$ mm. At $T = 300$ °C, the distributions of σ_x compression are close to σ_y (Figure 4, *e*, *f*), as well as for the plates $\delta = 2$ mm. Even on the back surface, the values of σ_x compression grow to $1.2\sigma_y$. Comparing the values of σ_x stresses at $T = 20$ and 150 °C (Figure 4, *a*, *b*), it is possible to see that, as for the plates $\delta = 2$ mm, heating to 150 ° C contributes to higher instantaneous stresses compared to EDT at $T = 20$ °C. But the further increase in the temperature of the contact interaction of up to 300 °C does not cause noticeable differences in the instantaneous stress state compared to those obtained at lower *T* values.

The σ_x compression component at $T = 20$ °C at a distance of 5 mm from SL reaches the values from $0.54\sigma_y$ on the outer to $0.27\sigma_y$ on the back surface of the plate (Figure 4, *a*). The compression σ_x stresses at a distance of 5 mm from SL reach the values from $0.79\sigma_y$ on the outer to $0.42\sigma_y$ on the back surfaces of AMg6 alloy at $T = 150$ °C (Figure 4, *b*). Instantaneous stresses reach the maximum values at 300 °C. Thus, the σ_x compression component at a distance of 5 mm from SL reaches the values from $1.4\sigma_y$ on the outer to $0.94\sigma_y$ on the back surfaces of AMg6 alloy at $T = 300$ °C (Figure 4, *c*).

Figure 5 shows the results of computation of the instantaneous distributions of σ_x in the plates $\delta = 8$ mm, which differ significantly from the stress states of the plates $\delta = 2$ and 4 mm. It can be seen that both along SL, as well as at a distance of 5 mm from it, σ_x transfer from compression stresses on the outer surface to tensile stresses on the back one in the entire investigated temperature range.

Thus, at $T = 20$ °C, the values of σ_x along SL change from $0.48\sigma_y$ compression on the outer surface to σ_y tensile on the opposite one, and at a distance of 5 mm from SL — from $0.46\sigma_y$ compression on the outer to $0.6\sigma_y$ tensile on the opposite one (Figure 5, *a*). At $T = 150$ °C, the values of σ_x along SL change from $0.64\sigma_y$ compression on the outer surface to $1.2\sigma_y$ tensile on the opposite one, and at a distance of 5 mm from SL — from $0.9\sigma_y$ compression on the outer surface to $0.76\sigma_y$ tensile on the opposite one (Figure 5, *b*).

When *T* grows to 300 °C, the metal undergoes intense elastic-plastic flow during EDT, which can be explained by high-temperature heating of a significant volume (compared to $\delta = 2$–4 mm) of metal in the contact zone. Thus, the values of compression σ_x on the contact surface (point *B*) and tension on the back surface (point *C*) of the plate along SL and at a distance of 5 mm from SL exceed σ_y (Figure 5, *c*).

Table 2 presents the generalized results of modeling RSS of the σ_x component along SL and at a distance of 5 mm from SL for the plates $\delta = 2$–8 mm after EDT at different T. The stress values are given in relation to $\sigma_y = f(T)$ (Table 1), which correspond to *T* value, for which the contact interaction was calculated. The lines 1, 4, and 7 show the values of the

Table 2. Relative values of RSS σ_x component in the butt joints of AMg6 alloy $\delta = 2$; 4 and 8 mm after their EDT under conditions of heating to $T = 20$, 150 and 300 °C

Number	δ, mm	*T*, °C	Values of $\sigma_x \times \sigma_y$ at the points along the line *B*–*C*			Values of $\sigma_x \times \sigma_y$ at the points at a distance of 5 mm from the line *B*–*C*		
			B	δ/2	*C*	*B*	δ/2	*C*
1	2	RSS at 20 °C*	–1	–1	–1	–1	–0.5	–0.4
2		RSS at 20 °C* after EDT at *T* = 150 °C	–1.2	–1.26	–1.23	–1.16	–0.66	–0.5
3		RSS at 20 °C* after EDT at *T* = 300 °C	–0.43	–0.45	–0.46	–0.4	–0.32	–0.4
4	4	RSS at 20 °C*	–0.88	–1.0	–0.72	–0.54	–0.2	–0.27
5		RSS at 20 °C* after EDT at *T* = 150 °C	–0.93	–1.0	–0.83	–0.73	–0.34	–0.43
6		RSS at 20 °C* after EDT at *T* = 300 °C	–0.44	–0.5	–0.54	–0.49	–0.38	–0.41
7	8	RSS at 20 °C*	–0.48	–0.4	1	–0.46	0.2	0.6
8		RSS at 20 °C* after EDT at *T* = 150 °C	–0.59	–0.53	1.15	–0.83	0.17	0.72
9		RSS at 20 °C* after EDT at *T* = 300 °C	–0.7	–0.66	1.0	–1.2	0	0.5

*RSS values are given in relation to $\sigma_y = f(T)$ in Table 1.

σ_x RSS component of the plates, respectively, $\delta = 2$, 4, and 8 mm after EDT at $T = 20$ °C. In the lines 2, 5 and 8, residual σ_x for $\delta = 2$, 4 and 8 mm after cooling from $T = 150$ to 20 °C and in 3, 6 and 9 similarly after cooling from $T = 300$ to $T = 20$ °C.

When comparing the data of the lines 1, 4, and 7 for $T = 20$ °C, the lines 2, 5, and 8 for $T = 150$ °C, and the lines 3, 6, and 9 for 300 °C, it can be seen that EDT of the plates $\delta = 2–4$ mm at $T = 20–300$ °C along SL promotes the formation of compression σ_x. However, the effect of treatment is significantly reduced when δ grows to 8 mm, which contributes to the reduction of peak values of compression stresses and transition from compression on the contact (at the point *B*) to tensile on the back (point *C*) surfaces.

For the section "5 mm from SL" the pattern is somewhat different. For example, when δ grows from 2 to 4 mm, the values of compression σ_x decrease almost by half from the outer surface — point *B* to the back one — point *C*. Thus, with an increase in δ, the effect of EDT on the metal of welded joint near the fusion line decreases. An increase in δ to 8 mm determines a decrease in the peak compression σ_x stresses compared to $\delta = 2–4$ mm and the formation of tensile stresses on the sections $\delta/2$ and on the back surface at the point *C*.

Summarizing the abovementioned data, it should be noted that for EDT application when $\delta = 2–4$ mm, the optimal *T* value is 150 °C, at which AMg6 alloy does not significantly lose its elastic properties (see Table 1).

However, for $\delta = 8$ mm, the action of *T* does not have such a noticeable effect on the efficiency of EDT for RSS correction (at a set V_0 value), as for $\delta = 2–4$ mm. When comparing the lines 7, 8 and 9, it is possible to see a slight difference in σ_x values, that were obtained as a result of EDT at $T = 20–300$ °C for $\delta = 2–4$ mm.

Based on the results of Figures 3–5 and Table 2, it should be noted that at a set vertical velocity V_0 of the electrode-indenter (Figure 1), one-sided EDT contributes to the formation of compression RSS on both surfaces of the welded joints of AMg6 alloy plates $\delta = 2–4$ mm in contrast to $\delta = 8$ mm, where tensile stresses are formed on the back surface. Thus, at $V_0 = 5$ m/s, it is advisable to carry out double-sided EDT of AMg6 alloy plates $\delta = 8$ mm to obtain compression RSS on both sides of the welded joints.

The obtained results can be explained by the fact that EDT at $T = 150$ °C initiates the formation of higher relative instantaneous σ_x stresses compared to stresses at $T = 20$ °C. This contributes to the formation of higher compression RSS when the plate cools down compared to RSS after EDT at $T = 20$ °C. The given results can be explained by the fact that at $T = 150$ °C, AMg6 alloy does not yet lose its elastic properties, and thermal exposure additionally stimulates stress relaxation mechanisms, which is confirmed by the data [7]. However, during EDT at $T = 300$ °C, instantaneous stresses, the values of which are lower than at $T = 150$ °C, respectively, contribute to the formation of lower compressive RSS (compared to RSS after EDT at $T = 150$ °C).

The presented computational results showed that EDT of the welded joint metal $\delta = 2–8$ mm of AMg6 alloy, performed at $T = 150$ °C (which models treatment in a single process in simultaneously with fusion welding), is more efficient compared to EDT at $T = 300$ °C or with separate EDT after welding (which corresponds to EDT at $T = 20$ °C). The efficiency of EDT is determined by the formation of higher compression RSS values of the produced welded joint. At the same time, to form compression RSS across the thickness of welded joints $\delta = 2–4$ mm, it is enough to perform one-sided EDT (at a set V_0 value) and double-sided EDT for $\delta = 8$ mm.

CONCLUSIONS

1. On the basis of the developed mathematical model of the dynamic interaction of the electrode-indenter with a butt welded joint of AMg6 alloy $\delta = 2–8$ mm, a numerical evaluation of the effect of δ on the kinetics of stresses and RSS of plates as a result of electrodynamic treatment (EDT) at elevated temperatures was carried out.

2. According to the results of computations, it was proved that the use of EDT of AMg6 alloy weld metal $\delta = 2–8$ mm, performed at $T = 150$ °C (condition for modelling EDT in a single process simultaneously with fusion welding), contributes to the formation of higher compression RSS stresses compared to EDT at $T = 300$ °C or separate EDT after welding at $T = 20$ °C.

3. At the same time, to form compression RSS across the thickness of welded joints $\delta = 2–4$ mm, it is sufficient to perform one-sided EDT (at a set value of contact velocity V_0), and double-sided for $\delta = 8$ mm.

REFERENCES

1. Madi, Y., Besson, J. (2014) *Effect of residual stresses on brittle fracture. Mat. ECRS-9.* UTT, Troyes, France.
2. (2022) *Welding and technical diagnostics for the recovery of the economy of Ukraine*: Abstr. of Reports Sci. Conf. Kyiv, IAW.
3. Lobanov, L.M., Pashchin, N.A., Mikhodui, O.L., Sidorenko, Y.M. (2018) Electric pulse component effect on the stress state of AMg6 aluminum alloy welded joints under electrodynamic treatment. *Strength of Materials*, 50(**2**), 246–253. DOI: https://doi.org/10.1007/s11223-017-9862-8
4. Sydorenko, Y.M., Pashchyn, M.O., Mikhodui, O.L. et al. (2020) Effect of pulse current on residual stresses in AMg6

aluminum alloy in electrodynamic treatment. *Strength of Materials*, 52(**5**), 731–737. DOI: https://doi.org/10.1007/s11223-020-00226-2

5. Conrad, H., Sprecher, A. (1989) *The electroplastic effect in metals*. Ed. by F.R.N. Nabarro. Elsevier Sci. Publ. B.V., Dislocations in Solids, 500–529.
6. Shao, Quan, Kang, Jiajie, Xing, Zhiguo et al. (2019) Effect of pulsed magnetic field treatment on the residual stress of 20Cr2Ni4A steel. *J. of Magnetizm and Magnetic Materials*, **476**, 218–224.
7. Stepanov, G.V., Babutskii, A.I., Mameev, I.A. (2004) High-density pulse current-induced unsteady stress-strain state in a long rod. *Strength of Materials*, **36**, 377–381. DOI: https://doi.org/10.1023/B:STOM.0000041538.10830.34
8. Lobanov, L.M., Pashchyn, M.O., Mikhodui, O.L. et al. (2022) Stress-strain state of welded joints of AMg6 alloy after electrodynamic treatment during welding. *Strength of Materials*, 54(**6**), 983–996. DOI: https://doi.org/10.1007/s11223-023-00474-y
9. Lobanov, L.M., Pashchin, N.A., Mikhodui, O.L. (2012) Efficiency of electrodynamic treatment of welded joints of AMg6 alloy of different thickness. *The Paton Welding J.*, **3**, 6–10.
10. http://www.ansys.com/.
11. Masubuchi, K. (1980) *Analysis of welded structures*. Pergamon Press, Oxford, United Kingdom.

ORCID

L.M. Lobanov: 0000-0001-9296-2335,
M.O. Pashchyn: 0000-0002-2201-5137,
O.L. Mikhodui: 0000-0001-6660-7540,
N.L. Todorovych: 0000-0002-3872-5790,
Yu.M. Sydorenko: 0000-0001-8780-9459,
P.R. Ustymenko: 0000-0002-5318-2675

CONFLICT OF INTEREST

The Authors declare no conflict of interest

CORRESPONDING AUTHOR

M.O. Pashchyn
E.O. Paton Electric Welding Institute of the NASU
11 Kazymyr Malevych Str., 03150, Kyiv, Ukraine.
E-mail: svarka2000@ukr.net

SUGGESTED CITATION

L.M. Lobanov, M.O. Pashchyn, O.L. Mikhodui, N.L. Todorovych, Yu.M. Sydorenko, P.R. Ustymenko (2024) Computational evaluation of the influence of the thickness of welded joints of AMg6 alloy on their stress-strain state after electrodynamic treatment in the process of welding. *The Paton Welding J.*, **4**, 11–17.

JOURNAL HOME PAGE

https://patonpublishinghouse.com/eng/journals/tpwj

Received: 13.11.2023
Received in revised form: 09.02.2024
Accepted: 07.05.2024

DOI: https://doi.org/10.37434/tpwj2024.04.03

DETONATION COATINGS PRODUCED BY SPRAYING OF ALLOYED POWDERS BASED ON Fe–Al INTERMETALLICS

N.V. Vihilianska, T.V. Tsymbalista, A.I. Kildii, C.V. Iantsevitch, Z.G. Ipatova, N.A. Vasylkivska

E.O. Paton Electric Welding Institute of the NASU
11 Kazymyr Malevych Str., 03150, Kyiv, Ukraine

ABSTRACT

The research results on the structure, phase composition and properties of detonation coatings produced by spraying a mechanical mixture of Fe powders and AlMg and TiAl alloys, as well as composite powders of the same composition synthesized by the mechanochemical method, are presented. It was found that in the coatings produced with the use of mechanical mixtures of powders, the synthesis of intermetallic compounds does not occur and the coatings consist of initial components and their oxides. Therefore, it is advisable to use powders produced by the method of mechanochemical synthesis as spray materials. This result in the formation of coatings, in which the main phase is the Fe–Al intermetallic compound. Coatings of the Fe–AlMg and Fe–TiAl systems, produced by spraying of composite powders, are characterized by a dense lamellar structure consisting of alternating layers of metal and oxide components. The coatings exhibit high oxidation resistance in the temperature range of 700–800 °C, comparable to the oxidation resistance of cast iron-aluminium alloys, and allow increasing the oxidation resistance of carbon steels by 6–20 times. The corrosion resistance of Fe–AlMg and Fe–TiAl detonation coatings in a 3 % NaCl solution exceeds the corrosion resistance of uncoated carbon steel by 13.3 und 28.0 times, respectively. The obtained results allow recommending the use of the developed coatings for protection of parts operating in aggressive environments at temperatures of up to 800 °C.

KEYWORDS: intermetallic compounds of the Fe–Al system, mechanochemical synthesis, composite powders, detonation spraying, coating, oxidation resistance, corrosion resistance

INTRODUCTION

Intermetallic alloys based on Fe–Al iron aluminides are challenging materials that are considered as substitutes for heat-resistant steels and alloys due to their combination of their physicomechanical and service properties, as well as low cost of their initial components [1–3]. In particular, iron aluminide-based intermetallic alloys are attractive materials for a number of industrial applications both as cast materials and as protective coatings at medium and high temperatures, due to their high mechanical properties, relatively low density, resistance to high-temperature oxidation and excellent corrosion resistance in oxidising and sulphurizing environments [4–6]. The disadvantages of Fe–A1 intermetallic alloys that limit their widespread practical use are their low ductility at room temperature, insufficient strength and creep resistance at temperatures above 600 °C. An increase in ductility and strength characteristics of Fe–Al intermetallics is achieved by introducing alloying elements into their composition through the formation of carbides and borides, solid solutions, and ternary intermetallic compounds in the alloy structure [7–10].

To deposit coatings based on intermetallics of the Fe–Al system with alloying elements, mostly methods of plasma, high-velocity oxygen fuel (HVOF) and detonation spraying are used [11]. As materials for spraying, powders produced by spraying and mechanical alloying are used; as alloying elements, Cr, B and Zr are used. The produced coatings based on Fe–A1 intermetallic are characterized by high corrosion resistance in various aggressive environments, wear resistance, resistance to thermal shock and high-temperature oxidation (up to 1000 °C); the hardness of the coatings is 3–5 GPa [11, 12].

The aim of this work was to study the structure, phase composition and properties of coatings produced by detonation spraying of powders based on Fe–A1 intermetallics alloyed with Mg and Ti.

MATERIALS AND RESEARCH PROCEDURES

For detonation spraying, composite powders (CP) of the compositions 86Fe + 14(Al5Mg) and 60.8Fe + 39.2 (62.5Ti37.5Al) (wt.%) were used, which were produced by the method of mechanochemical synthesis (MChS) by processing a mixture of powders in a planetary mill, and mechanical mixtures of the same composition (Table 1). The powder of iron as well as AMg-5 and T65Yu35 alloys was used as initial powders for producing mechanical mixtures and CP. The compositions of the powder mixtures were intended to produce Fe_3A1 intermetallic. When Ti and Mg are used as alloying elements, the properties of coatings based on Fe–Al intermetallic can be improved by forming solid solutions and incoherent compounds.

Spraying of the coatings was carried out in the detonation spraying unit “Perun-C” applying the previously selected mode of spraying coatings based on

Table 1. Characteristics of powders for spraying [13]

Composition, wt.%	Production method	Phase composition
86Fe + 14(Al5Mg)	Mechanical mixing	Fe, solid solution of Mg in Al
	MChS	Solid solution of Mg in Fe_3Al
60.8Fe + 39.2(62.5Ti37.5Al)	Mechanical mixing	Fe, TiAl
	MChS	Solid solution of Al in FeTi ($Fe_{1-x}TiAl_x$)

Fe_3Al intermetallic, in which CP particles are heated to 0.8–0.9T_m and accelerated to the maximum velocity [14]. The following operating parameters were used for the unit: combustible gas (propane-butane) flow rate — 0.5 m^3/h, oxygen flow rate — 1.3 m^3/h, diluent gas (air) flow rate — 0.6 m^3/h, transport gas (air) flow rate — 0.4 m^3/h, shot frequency — 400/min, powder loading — 120 mg/shot, spraying distance — 110 mm. Powders with a particle size of 40–80 μm were used for spraying.

To study the coatings structure, the method of metallography (Neophot-32 microscope with a digital imaging attachment), and to study the phase composition — X-ray diffraction analysis (XRD) in DRON-3 diffractometer in CuK_α-radiation with a graphite monochromator at a step movement of 0.1° and an exposure time of 4 s at each point were used, followed by computer processing of digital data. Phase identification was performed using the ASTM database.

The oxidation resistance of the coated specimens was studied when heated in a muffle furnace of the SNOL 1.6.2,5.1/11-42 type in air environment at a temperature of 700–800 °C with an isothermal holding time of 5 h. The temperature in the furnace was regulated automatically and monitored by a 4530 type device, PP-S-1300 °C with an accuracy of ±5 °C. The mass increment of the specimens was determined in a VLR-20 analytical balance with an accuracy of 10^{-5} mg. The coatings were deposited on "acorn"-shaped specimens of St45 steel with a diameter of ~10 mm and a total surface area of ~5 cm^2. The specimens were placed in the furnace on a special stainless steel stand with holes for the specimens, which allowed air to reach the surface of the coating. After the experiments, the oxidation curves were plotted based on the results of the mass increment of the specimens.

The electrochemical properties of the coatings were studied using the potentiostatic method in a P-5827 potentiostat at a scanning rate of 0.2 mV/s at a temperature of 18–20 °C. Stationary potentials were measured relative to a chloride electrode. A 3 % NaCl solution and a 10% H_2SO_4 solution were chosen as the test environment. In the work, the depth corrosion

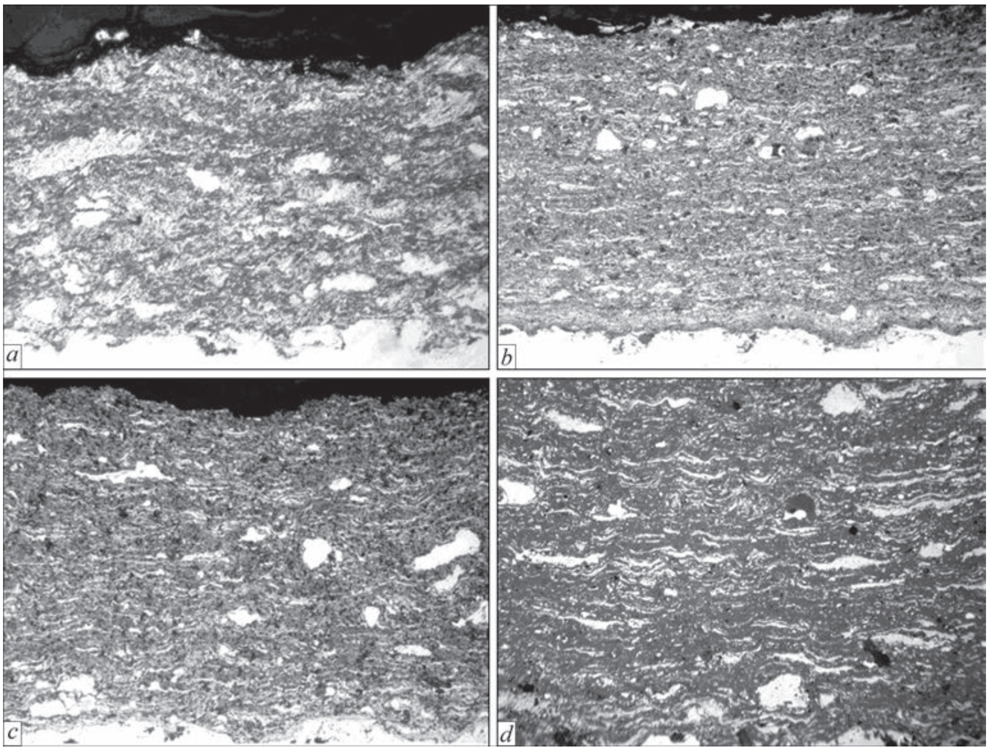

Figure 1. Microstructure (×400) of detonation coatings produced by spraying powders of the Fe–AlMg (*a*, *b*) and Fe–TiAl (*c*, *d*) systems using mechanical mixtures (*a*, *c*) and MChS powders (*b*, *d*)

index of coatings (K_c) and corrosion inhibition coefficient (γ) were calculated [15, 16].

RESEARCH RESULTS AND DISCUSSION

The coatings of the Fe–A1Mg and Fe–TiAl systems produced by spraying mechanical powder mixtures, exhibit a coarse lamellar structure consisting of alternating layers of light and dark oxide lamellae with the presence of melted partially deformed powder particles in the structure (Figure 1, *a*, *c*). In the case of using MChS powders for spraying, coatings are formed with a more homogeneous thin-lamellar structure with a small number of incompletely deformed particles (Figure 1, *b, d*). At the same time, in the coatings of the Fe–TiAl system, a smaller number of unmelted particles is observed, which may be associated with the phase composition of sprayed powders, which determines the degree of particles melting during the spraying process and the degree of their deformation during the formation of the coating layer.

Studies of the phase composition of the coatings produced by spraying powders of mechanical mixtures of the Fe–A1Mg and Fe–TiA1 systems have shown that synthesis of the Fe–A1 intermetallics formation does not have time to complete, and only oxidation of initial powder components Fe, A1, Mg and Ti occurs (Figure 2, *a*, *c*). The absence of Fe–A1 intermetallics formation during spraying of mechanical mixtures is explained by a low probability of collision and coagulation of particles in the spray jet and their high cooling rate during the formation of the coating layer, which limits the interaction of powders with the reaction of new phase formation between the initial components. In the case of spraying MChS powders, coatings are formed on the base of FeAl intermetallic with the presence of oxidation products of powder components (Figure 2. *b, d*). In contrast to coatings produced by spraying mechanical mixtures, coatings produced from MChS powders contain only a small amount of pure iron. The coating of the Fe–TiAl system contains the phase of the initial TiAl powder material and a product of iron and TiAl alloy interaction — Fe_2Ti phase. The magnesium component in the coating of the Fe–AlMg system, as in the case of spraying a mechanical mixture, is present in the form of a complex $MgAl_2O_4$ oxide.

Due to the fact that intermetallic Fe–Al phases are not formed in the coatings of the Fe–AlMg and Fe–TiAl systems produced by spraying mechanical mixtures, but initial components and their oxides remain, the coatings produced by spraying MChS powders were used for further studies of oxidation and corrosion resistance.

Figure 3 shows the kinetic dependences of the oxidation of detonation coatings and 45 steel in the

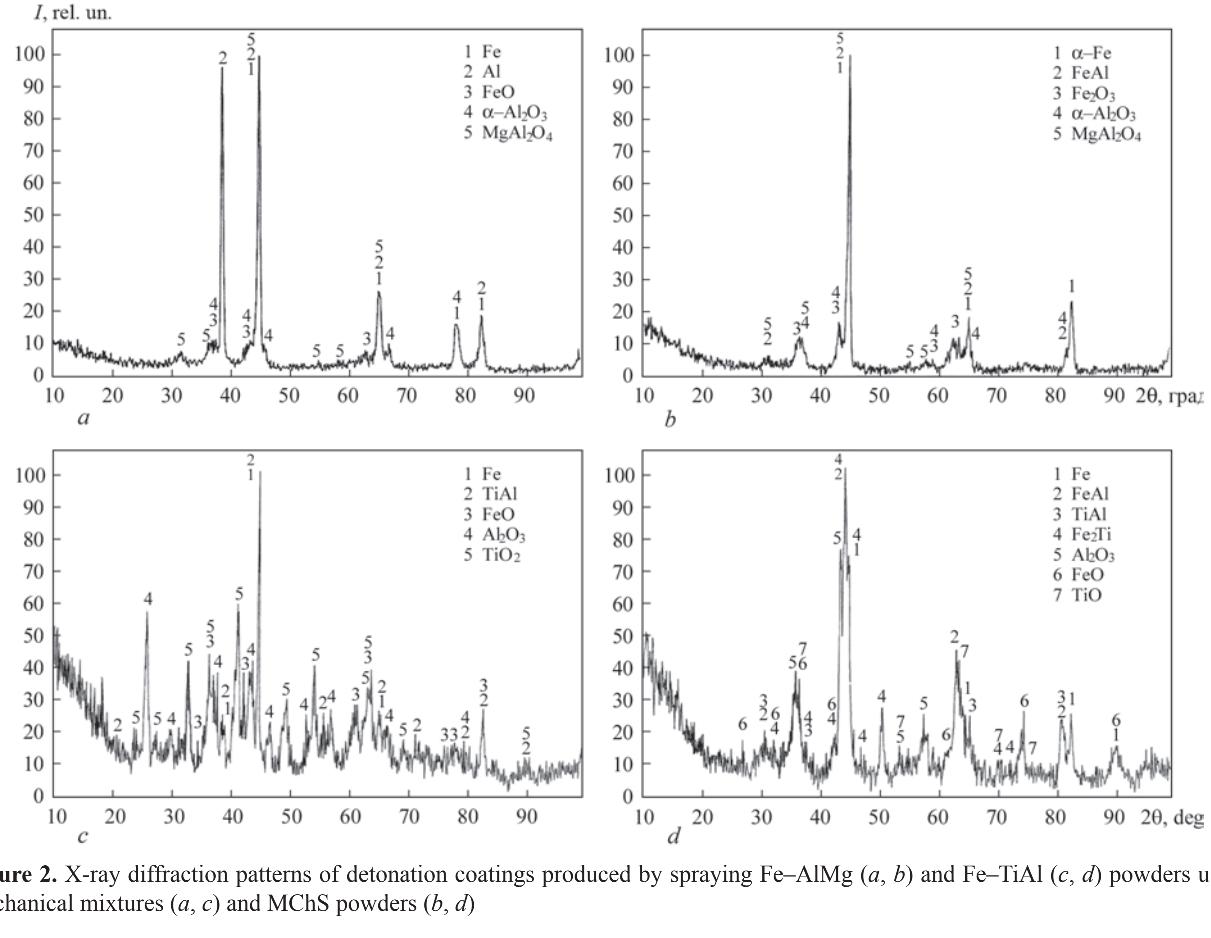

Figure 2. X-ray diffraction patterns of detonation coatings produced by spraying Fe–AlMg (*a*, *b*) and Fe–TiAl (*c*, *d*) powders using mechanical mixtures (*a*, *c*) and MChS powders (*b*, *d*)

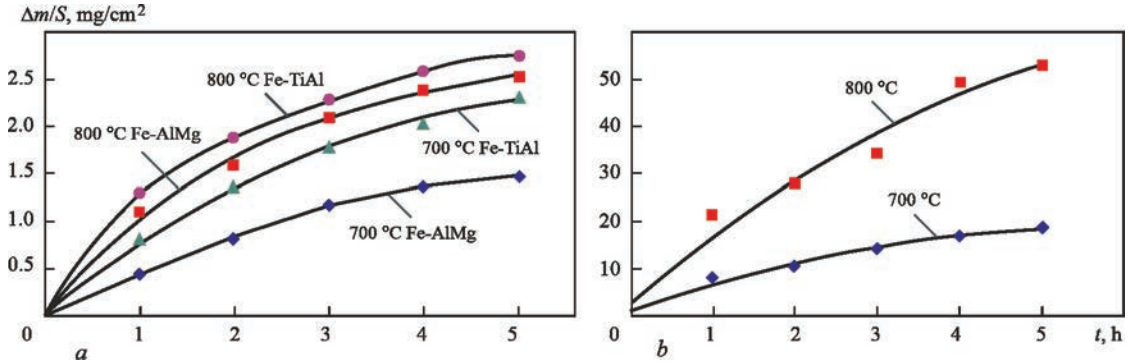

Figure 3. Kinetic oxidation curves: *a* — detonation Fe–A1Mg and Fe–TiAl coatings; *b* — steel 45 without coating

Table 2. Results of electrochemical tests of detonation Fe–AlMg and Fe–TiAl coatings in various aggressive environments

Coating	3 % NaCl solution				10 % H_2SO_4 solution			
	E_c, V	i_c, A/cm^2	K_c, mm/year	γ	E_c, V	i_c, A/cm^2	K_c, mm/year	γ
Fe–AlMg	–0.3	$3.5·10^{-6}$	0.038	13.3	–0.26	$4.4·10^{-5}$	0.452	1.3
Fe–TiAl	–0.28	$1.1·10^{-6}$	0.018	28.0	–0.22	$2.4·10^{-5}$	0.256	2.4
Steel 45 without coating	–0.50	$5.0·10^{-5}$	0.5035	–	–0.20	$2.5·10^{-4}$	0.6022	–

temperature range of 700–800 °C. From the nature of the curves in the entire studied temperature range, it follows that the oxidation mechanism in all cases is subject to a parabolic time law, which indicates that the diffusion stage is the limiting link in the process.

The obtained results indicate high oxidation resistance of Fe–AlMg and Fe–TiAl detonation coatings, which exceeds the oxidation resistance of carbon steel by 6–10 times at 700 °C and by 18–20 times at 800 °C. The value of the mass increment $\Delta m/St$ for all the coatings does not exceed 0.6 mg/cm·h, which is comparable to the oxidation resistance characteristics of cast iron-aluminium alloys and slightly exceeds the oxidation resistance of plasma coatings produced by spraying unalloyed FeAl powders [17, 18].

Comparing the results of the oxidation kinetics for detonation coatings from FeAl-based alloyed powders, one can note a higher oxidation resistance of the Fe–AlMg coating than the Fe–TiAl coating. This is most likely predetermined by the presence of aluminium-magnesium $MgAl_2O_4$ spinels in the Fe–AlMg coating, which have a higher resistance to high-temperature oxidation than aluminium, iron, and titanium oxides formed in the Fe–TiAl coating during the spraying process.

Electrochemical studies have shown that the protective properties of coatings in a 3 % NaCl solution are by an order higher than those in a 10 % H_2SO_4 solution, which may be associated with different types of depolarisation of the corrosion process (hydrogen in a sulphuric acid solution, oxygen in a 3 % NaCl solution) [16].

It has been shown that in a sulphuric acid solution, detonation coatings deposited on 45 steel reduce the corrosion current by an order and increase the corrosion resistance by 1.3–2.4 times (Table 2). The higher protective properties are demonstrated by detonation coatings in a 3 % NaCl solution. The carried out tests have shown that in a 3 % NaC1 solution, the corrosion rate of 45 steel with detonation coatings is reduced by 13.3–28.0 times compared to steel without coating. In terms of corrosion resistance, FeAl-based detonation coatings are not inferior to coatings deposited by the plasma method [19].

The difference in the corrosion resistance of Fe–AlMg and Fe–TiAl coatings is explained by the peculiarities of their microstructure. Corrosion can occur at the interfaces of the distribution of deformed particles (splats) in the coating layer, and thanks to the formation of a homogeneous structure with the presence of thin oxide layers over the entire coating area, Fe–TiAl coatings have higher corrosion properties in the studied electrolytes.

CONCLUSIONS

Fe–Al-coatings were developed, produced by detonation spraying, in which mechanical mixtures of iron powders with aluminium Al5Mg alloy and TiAl intermetallic were used as materials for spraying, as well as powders of the same compositions, produced by mechanochemical synthesis.

It was found that under the conditions of detonation spraying, when using mechanical mixtures of powders, it is impossible to provide an active interfacial interaction between the components and the formation of intermetallic phases in a coating does not occur. In the case of using MChS powders, coatings based on FeAl intermetallic with a dense lamellar structure are formed, consisting of layers of metal and alternating oxide components.

The results of studies of the oxidation resistance of detonation coatings of the Fe–A1Mg and Fe–TiAl systems indicate their high resistance to high-temperature oxidation in the temperature range of 700–800 °C. The use of Ti-alloyed powders for spraying allows increasing the oxidation resistance of carbon steel at 700 °C by 6 times, and at 800 °C by 18 times; in the case of Mg-alloyed powders, the oxidation resistance of carbon steel increases by 10 times at 700 °C and 20 times at 800 °C.

It was found that the application of Fe–AlMg and Fe–TiAl detonation coatings allows improving the corrosion resistance of carbon steel in a 3 % NaCl solution by 13.3 and 28.0 times, respectively.

REFERENCES

1. Deevi, S.C., Sikka, V.K. (1996) Nickel and iron aluminides: an overview on properties, processing, and applications. *Intermetallics*, 4(**5**), 357–375. DOI: https://doi.org/10.1016/0966-9795(95)00056-9
2. Stoloff, N.S. (1998) Iron aluminides: present status and future prospects. *Materials Sci. and Eng.*: A, 258(1–2), 1–14. DOI: https://doi.org/10.1016/s0921-5093(98)00909-5
3. Palm, M., Stein, F., Dehm, G. (2019) Iron aluminides. *Annual Review of Materials Research*, 49(**1**). DOI: https://doi.org/10.1146/annurev-matsci-070218-125911
4. Zamanzade, M., Barnoush, A., Motz, C. (2016) A review on the properties of iron aluminide intermetallics. *Crystals*, 6(**1**), 10. DOI: https://doi.org/10.3390/cryst6010010
5. Senderowski, C., Chodala, M., Bojar, Z. (2015) Corrosion behavior of detonation gun sprayed Fe–Al type intermetallic coating. *Materials*, 8(**3**), 1108–1123. DOI: https://doi.org/10.3390/ma8031108
6. Peng, J., Moszner, F., Rechmann, J. et al. (2019) Influence of Al content and pre-oxidation on the aqueous corrosion resistance of binary Fe–Al alloys in sulphuric acid. *Corrosion Sci.*, **149**, 123–132. DOI: https://doi.org/10.1016/j.corsci.2018.12.040
7. Baligidad, R.G., Prasad, V.V. Satya, Rao, A. Sambasiva (2007) Effect of Ti, W, Mn, Mo and Si on microstructure and mechanical properties of high carbon Fe–10·5 wt-%Al alloy. *Materials Science and Technology*, 23(**5**), 613–619. DOI: https://doi.org/10.1179/174328407x158631
8. Stein, F., Schneider, A., Frommeyer, G. (2003) Flow stress anomaly and order-disorder transitions in Fe_3Al-based Fe–Al–Ti–X alloys with X=V, Cr, Nb, or Mo. *Intermetallics*, 11(**1**), 71–82. DOI: https://doi.org/10.1016/s0966-9795(02)00187-5
9. Zamanzade, M., Vehoff, H., Barnoush, A. (2013) Effect of chromium on elastic and plastic deformation of Fe_3Al intermetallics. *Intermetallics*, **41**, 28–34. DOI: https://doi.org/10.1016/j.intermet.2013.04.01
10. Krein, R., Schneider, A., Sauthoff, G., Frommeyer, G. (2007) Microstructure and mechanical properties of Fe_3Al-based alloys with strengthening boride precipitates. *Intermetallics*, 15(**9**), 1172–1182. DOI: https://doi.org/10.1016/j.intermet.2007.02.005
11. Deevi, S.C. (2020) Advanced intermetallic iron aluminide coatings for high temperature applications. *Progress in Materials Science*, 100769. DOI: https://doi.org/10.1016/j.pmatsci.2020.100769
12. Cinca, N., Guilemany, J. M. (2012) Thermal spraying of transition metal aluminides: An overview. *Intermetallics*, **24**, 60–72. DOI: https://doi.org/10.1016/j.intermet.2012.01.020
13. Borisov, Yu.S., Borisova, A.L., Burlachenko, A.N. et al. (2017) Structure and properties of alloyed powders based on Fe_3Al intermetallic for thermal spraying produced using mechanochemical synthesis method. *The Paton Welding J.*, **9**, 33–39. DOI: https://doi.org/doi.org/10.15407/tpwj2017.09.06
14. Borisov, Yu.S., Borisova, A.L., Astakhov, E.A. et al. (2017) Detonation coatings of intermetallic powders of Fe–Al system produced using mechanical alloying. *The Paton Welding J.*, **4**, 23–29. DOI: https://doi.org/10.15407/tpwj2017.04.05
15. Pokhmurskyi, V.I., Khoma, M.S. (2008) *Corrosion fatigue of metals and alloys*. Lviv, SPOLOM [in Ukrainian].
16. Sakhnenko, M.D., Ved, M.V., Yaroshok, T.P. (2005) *Basics of the theory of corrosion and protection of metals*. Kharkiv, NTU KhPI [in Ukrainian].
17. Haušild, P., Karlík, M., Skiba, T. et al. (2012) High temperature oxidation of spark plasma sintered and thermally sprayed FeAl-based iron aluminides. *Acta Physica Polonica A*, **122**, 465–468. DOI: https://doi.org/10.12693/APHYSPOLA.122.465
18. Marx, V., Palm, M. (2016) Oxidation of Fe–Al Alloys (5–40 at.% Al) at 700 and 900 °C. *Materials Science Forum*, **879**, 1245–1250. DOI: https://doi.org/10.4028/www.scientific.net/msf.879.1245
19. Vihilianska, N.V., Gryshchenko, O.P., Iantsevych, K.V. et al. (2022) Corrosion resistance of plasma coatings based on composite powders with FeAl intermetallic. *The Paton Welding J.*, **12**, 35–39. DOI: https://doi.org/10.37434/tpwj2022.12.05

ORCID

N.V. Vihilianska: 0000-0001-8576-2095,
T.V. Tsymbalista: 0000-0001-9569-7776,
A.I. Kildii: 0000-0001-8133-8705,
C.V. Iantsevitch: 0000-0002-3975-7727,
Z.G. Ipatova: 0000-0003-2209-408X,
N.A. Vasylkivska: 0000-0001-8311-6428

CONFLICT OF INTEREST

The Authors declare no conflict of interest

CORRESPONDING AUTHOR

N.V. Vihilianska
E.O. Paton Electric Welding Institute of the NASU
11 Kazymyr Malevych Str., 03150, Kyiv, Ukraine.
E-mail: pewinataliya@gmail.com

SUGGESTED CITATION

N.V. Vihilianska, T.V. Tsymbalista, A.I. Kildii, C.V. Iantsevitch, Z.G. Ipatova, N.A. Vasylkivska (2024) Detonation coatings produced by spraying of alloyed powders based on Fe–Al intermetallics. *The Paton Welding J.*, **4**, 18–22.

JOURNAL HOME PAGE

https://patonpublishinghouse.com/eng/journals/tpwj

Received: 30.11.2023
Received in revised form: 16.02.2024
Accepted: 02.05.2024

DOI: https://doi.org/10.37434/tpwj2024.04.04

STUDY OF THE INFLUENCE OF GMAW-CMT AND PULSE PROCESSES OF ADDITIVE DEPOSITION OF SILICON BRONZE CuSi3Mn1 ON THE GEOMETRICAL CHARACTERISTICS OF THE SURFACE, STRUCTURE AND STRESS-STRAIN STATE OF FINISHED PRODUCTS

A.O. Perepichay, I.M. Lahodzinskyi

National Technical University of Ukraine “Igor Sikorsky Kyiv Polytechnic Institute”
37 Prospect Beresteiskyi (former Peremohy), 03056, Kyiv, Ukraine

ABSTRACT

Silicon bronzes of CuSi3Mn1 type (BrKMts3-1) are widely used in the machine-building, aerospace, and mining industries due to their properties. Given the rather high cost of copper-based nonferrous alloys, the use of wire-arc additive manufacturing (WAAM) technologies is relevant. Cold Metal Transfer (CMT) and pulse arc surfacing (Pulse process) are used to prevent overheating and reduce the heat input during surfacing of copper-based alloys. The results of studies of layer-by-layer surfacing of silicon bronze indicate a certain dependence of geometrical characteristics, structural composition, and susceptibility to defect formation on the applied surfacing method (GMAW-CMT/Pulse). Short-circuit surfacing provides a greater height of each bead than with pulse current supply (up to 25 %) and a reduction in the width of each bead, respectively. However, the surface unevenness also increases. The sample deposited by the GMAW-Pulse method contains critical defects in the form of transverse cracks. The stress-strain state modeling for the pulse surfacing method indicates a critical accumulation of normal tensile stresses, which, in combination with the anisotropic structure of the metal, may be the cause of crack formation.

KEYWORDS: WAAM, GMAW, Cold Metal Transfer, pulse arc surfacing, additive technologies, CuSi3Mn1, layer-by-layer surfacing

INTRODUCTION

Silicon bronzes CuSi3Mn1 (BrKMts3-1) are widely used in chemical, petroleum processing and mining industries, due to their high resistance to aggressive media, elasticity and antifriction properties. Production of unit repair parts (bushings, gears) or restoration of the already damaged ones opens up broad possibilities for application of Additive Manufacturing technologies to produce blanks for further finishing treatment instead of the traditional machining operations, as the rather high cost of nonferrous metals, and particularly copper alloys, makes it necessary to reduce machining wastes during manufacture of the finished part or product [1].

Additive synthesis with application of silicon bronze CuSi3Mn1 has already been considered in the sphere of application of concentrated heat sources of the type of Non-Vacuum Electron Beam (NV-EBM) [2]. However, using the laser or electron beam is problematic due to a high coefficient of surface reflection of copper and its alloys [3]. Therefore, application of Wire-Arc Additive Manufacturing (WAAM) technologies is justified from the viewpoint of economic characteristics: relatively low equipment cost and practical absence of limitations on the overall dimensions and shape of synthesized products. Additive layer-by-layer surfacing of CuSi3Mn1 can be performed by basic GMAW technology. Owing to the presence of active deoxidizers (silicon, manganese) in its composition, silicon bronze CuSi3Mn1 lends itself readily to welding and surfacing, although with some limitations on the thickness of the deposited material layer. In view of the high conductivity of copper and alloys on its base, there is the need to use powerful concentrated heat sources. At the same time, the high fluidity of the metal melt and rather high coefficient of thermal expansion ($18 \cdot 10^6$) in combination with a considerable [4] metal shrinkage at crystallization from the liquid state create the prerequisites for accumulation of considerable residual stresses at multilayer deposition. This, in its turn, can lead to formation of critical cracklike defects. Excess heat input also leads to structural growth of columnar grains oriented in the direction of heat removal, resulting in anisotropic mechanical properties. To control the heat input and avoid excess overheating at CuSi3Mn1 deposition, and to produce an equiaxed grain structure, the following variants of GMAW method are used: welding with short-circuiting — Cold Metal Transfer (CMT) process and heat input regulation with pulsed current feed (Pulse process).

A significant number of studies is devoted to GMAW-CMT deposition, using silicon bronze (CuSi3Mn1) as an additional component in tandem with AK5 aluminium alloy (AlSi5-ER4043) with the purpose of lowering the probability of intermetallic phase formation and improvement of mechanical properties of the finished products [5-7]. However, in work [5] there is clearly a problem of excess level of residual shrinkage of the deposited layers of the formed sample, leading to the deposited wall tearing from the copper base. In work [8] the authors considered the influence of deposition mode parameters (heat input level) on shaping and structural changes of layered deposit of CuSi3Mn1. The authors also established the fact of increase of the produced sample surface hardness at current rise. Such behaviour, in particular, increase of silicon bronze hardness, radically differs from low-alloyed steels [9]. At the same time, the roughness (unevenness) of the surface decreases with increase of current from 70 to 110 A, which is logical, as the time of existence of the weld pool melt becomes greater, and it promotes better spreading of liquid metal and leads to greater bead width [8].

In work [10], the influence of the method of short-circuiting surfacing (GMAW-CMT) and pulse surfacing mode (GMAW-Pulse) on the sample structure, using CuSi3Mn1 solid wire, was studied. The authors of work [10] have rather broadly considered the subject of the influence of mechanical transition of electrode metal drops (GMAW-CMT process) and contactless drop detachment at the moment of pulse current feed (GMAW-Pulse process) on the structural changes during weld pool crystallization. We have found that pulse current feed leads to local overheating of the liquid weld pool with a considerable temperature gradient from the melt surface to weld pool bottom. This causes growth of long grains of columnar type at metal crystallization, causing a deterioration of mechanical characteristics of the already deposited metal. Application of GMAW-CMT surfacing with short-circuiting, contrarily, promotes formation of equiaxed grains and their refinement, having a negative impact on mechanical characteristics of the products [10].

However, in works [8] and [10] investigations of the additive process were conducted at deboosted modes of surfacing (from 100 to 110 A) and quite small number of deposited layers (up to 5), which does not allow fully assessing the surface shaping characteristics and the influence on the stress-strain state of the finished product.

Other scientific works are considering application of CuSi3Mn1-containing fillers only as an intermediate material for braze-welding of bimetal compositions of TC4 titanium alloy — austenitic steel E304 [11] and other [12, 13], and are not related to the subject of additive manufacturing of products. Considering the small number of works highlighting complete additive synthesis with application of purely silicon bronzes CuSi3Mn1 by the methods of GMAW-CMT and Pulse surfacing methods, studying this direction is relevant.

The objective of the work is investigation of the possibility of additive manufacturing of 3D spatial products from silicon bronzes CuSi3Mn1 (BrKMts3-1) with application of arc heat sources and their variants in the form of CMT and Pulse processes, as well as their influence on the geometrical characteristics, structure, and tendency to defect formation in the produced samples.

The tasks for reaching the objective:

- perform analysis of literature sources as to the possibility of applying silicon bronzes in the processes of additive manufacturing of products, tendency to defect initiation, features of shape- and structure formation of the layers of the metal deposited using arc heat sources;
- produce samples by layer-by-layer arc surfacing using GMAW-CMT/Pulse methods with solid wire CuSi3Mn1 (BrKMts3-1) in pure argon atmosphere (100 % Ar) on a substrate from austenitic stainless steel E304;
- study the geometrical characteristics of the produced sample surface;
- study the structure of the deposited sample metal, produced by GMAW-CMT/Pulse methods of arc surfacing, and tendency to defect formation.

EXPERIMENTAL PROCEDURE

Experiments on GMAW-CMT/Pulse surfacing were performed in the experimental facility for welding rectilinear welds (*X* axis) with a cantilever for two-coordinate (along axes *Y*, *Z*) positioning of the welding torch (Figure 1, *a*). Fronius TransPulse Synergic 2700 welding source in tandem with PullMig CMT MHP 400i torch was used. As in the previous studies [9], a strategy of deposition in the reciprocal direction for each layer alternatively was selected (Figure 1, *b*). Research work was performed in the facilities of LLC “Science-Production Center “Plazer””.

Investigations of layer-by-layer synthesis were conducted on plates from 6 mm thick austenitic stainless steel AISI 304 (08Kh18N10). Layer-by-layer surfacing was performed by solid electrode wire CuSi3Mn1 (BrKMts3-1) of diameter $d_e = 1.2$ mm^2. Surfacing at both GMAW-CMT and Pulse processes was carried out at the same deposition rate ($V_w =$ $= 600$ mm/min) and filler wire feed ($V_{w.f} = 3.5$ m/min). Shielding gas was 100 % argon.

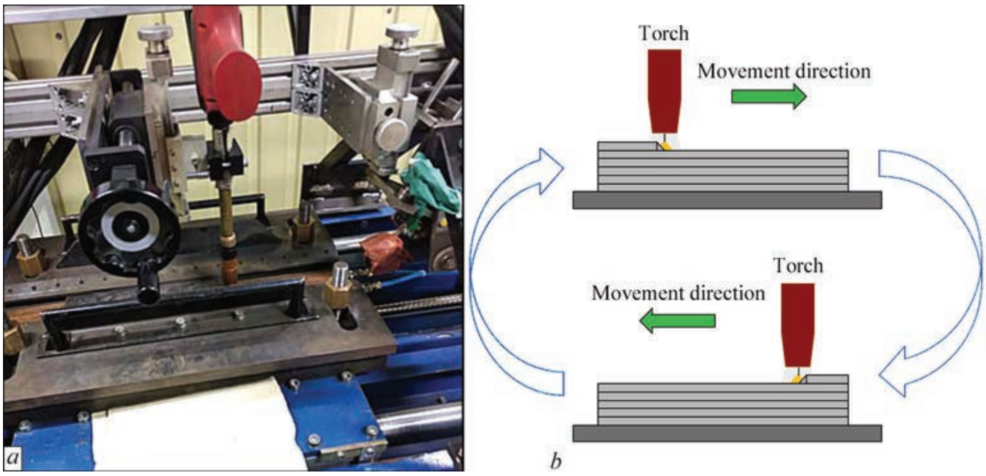

Figure 1. Surfacing equipment and procedure: *a* — facility for straight weld deposition; *b* — direction of torch movement at layer-by-layer deposition

Modes of layer-by-layer surfacing of samples are given in Table 1. Energy input and mode parameters (current, voltage) taken by mean arithmetic values, because of the difficulty of following the current parameters at the moment of pulse feed (Pulse method) and features of GMAW-CMT process with short-circuiting, are described in work [10].

Considering the gradual lowering of heat removal into the base and heat accumulation in the previous layers at alternative layer building up, a strategy of cooling to 120 °C after each layer was selected. It allows eliminating the influence of excess heat on the crystallization process and shaping of each individual layer, protecting the already deposited metal layers from excess overheating, which is confirmed by the results of the previous work [9, 10].

Samples for investigations of macro- and microstructure were prepared by the method of mechanical cutting out of the formed walls with addition of lubricant-coolant fluid to avoid metal overheating with distortion of its structure.

To study the structure, the samples were prepared on high-speed polishing wheels using diamond pastes. The structure of experimental sample metal was revealed by etching in a hot solution of nitric (HNO_3), orthophosphoric (H_3PO_4) and acetic (CH_3COOH) acids in the proportion of 10–30–60 %, respectively.

Structural studies were performed using metallographic microscope Neophot-32. Phase component hardness was determined by Vickers in LECO M-400 hardness meter. The load was 1N (100 g), time of load application was 10 s. Digital photos of the structures were taken with “Olympus C-500” camera.

Finite element method was used to analyze the stress-strain state (SSS) in the deposited samples. Modeling included plotting 3D finite element model of the deposited samples. A model of the type of equilateral triangle with side $l = 50$ mm having regions of deposition direction reversal was used in the studies. It allows assessment of the influence and distribution of nonuniform thermal load in case of a curvilinear trajectory [14]. The geometrical model of a sample, boundary conditions and finite element grid are shown in Figure 2.

The finite element model was used to perform analysis of the stress-strain state. The system of equations was solved in a series of small steps, beginning from the start of the printing process and up to cooling of the weld to ambient temperature. Each step included calculation of the increments of node displacements using Newton iteration method. The data on the level of stresses and strains were updated after each iteration, and calculation of residual shrinkage force was also performed. The theory of plasticity with kinematic strengthening was used in the model as a characteristic of metal behaviour. Such an approach to modeling provided a detailed understanding and analysis of the processes, occurring during 3D deposition by GMAW-Pulse process.

Table 1. Modes of layer-by-layer surfacing

Method	Filler wire	Shielding gas	Energy input, J/mm	Current, A	Voltage, V	Nozzle diameter, mm	Wire feed rate $V_{w.f}$, m/min	Deposition rate V_w, mm/min	Gas flow rate, l/min
GMAW-CMT	(BrKMts3)	100 % Ar	125	131	12	16	3.5	600	15
GMAW-Pulse			192	120	20				

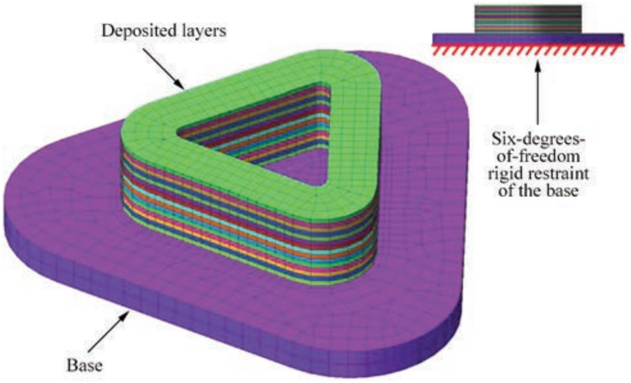

Figure 2. Finite element grid and boundary conditions for finite element modeling of GMAW-Pulse surfacing process

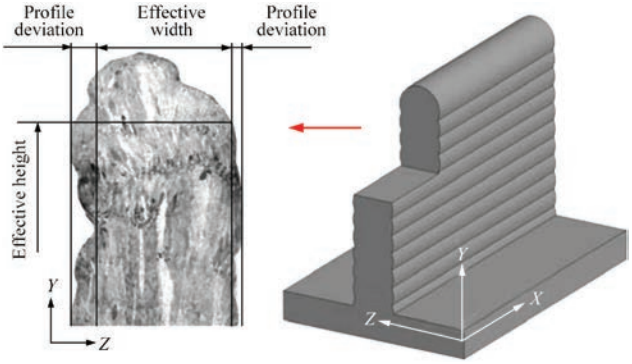

Figure 3. Determination of the parameters of effective height, effective thickness and maximal profile deviation [6]

INVESTIGATION RESULTS AND THEIR DISCUSSION

Figures 4, 5 shows the results of analysis of the dependence of changes in the geometrical characteristics of the produced samples from silicon bronze CuSi3Mn1 (BrKMts3-1) on the applied GMAW-CMT/Pulse surfacing method.

Geometrical characteristics of the surface of the samples were assessed, using an approach with determination of the parameters of effective height and width of the sample wall, which was proposed by the authors in work [15] and was used in previous experiments with low-carbon steels [9]. This approach allows with a rather high degree of accuracy establishing the share of useful deposited metal of the product and the percentage of metal envisaged for allowance for the subsequent finishing treatment. Maximal value of deviation of the wall profile symmetrically from the deposited layer axis (Figure 3) allows evaluation of the unevenness of the finished product surface. Maximal efficiency of metal utilization is achieved at minimal values of its surface unevenness. This is particularly urgent at application of nonferrous metals and copper alloys (CuSi3Mn1), in connection with their high cost compared to low-alloyed and low-carbon steels [12].

The height of 50 deposited layers of silicon bronze (CuSi3Mn1) of samples produced by GMAW-CMT

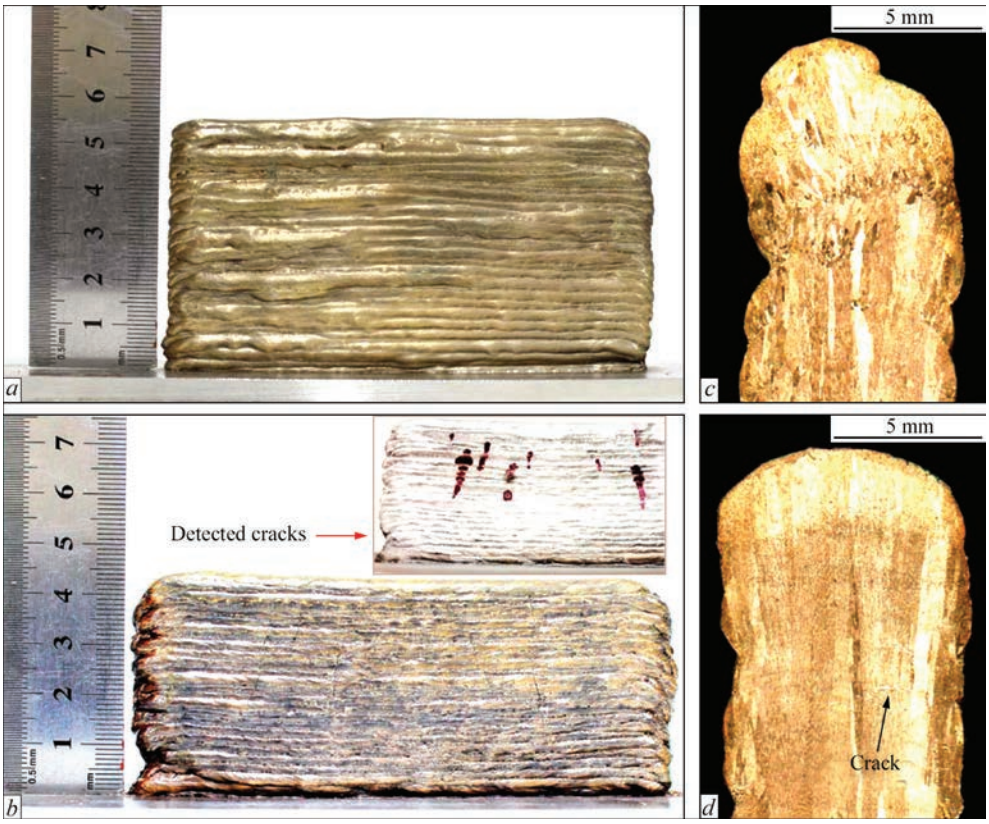

Figure 4. Samples of silicon bronze CuSi3Mn1 (BrKMts3-1) produced by different surfacing methods: *a* — GMAW-CMT; *b* — GMAW-Pulse with cracks detected by liquid-penetrant inspection; *c* — GMAW-CMT, macrostructure; *d* — GMAW-Pulse, macrostructure with cracks present in the transverse section

process (Figure 4, *a*) is 25 % greater (44.9 and 54.9 mm, respectively) at reduction of the effective layer thickness from 9.75 to 8.5 mm, compared to GMAW-Pulse process (Figure 4, *b*).

At GMAW-CMT surfacing method the wall surfaces have clearcut sagging of crystallized metal of individual layers, leading to increase of the characteristic of deviation of side surface profile from 0.5 to 1.13 mm. For GMAW-Pulse method, the unevenness characteristic is smaller, and it is in the range of 0.72–0.82 mm (Figure 4, *b*). On the whole, the parameters of the dependence of unevenness (Figure 5), effective width and height can be regarded as the consequences of the change in the level of the heat input in keeping with the applied GMAW process. The degree of overheating and time of weld pool staying in the liquid state influence the solidification rate with a change in the pattern of weld pool metal spreading.

In samples produced by GMAW-CMT process visual inspection did not reveal any surface defects. However, appearance of critical defects was found at GMAW-Pulse surfacing method. During deposition after reaching the 32nd layer, initiation of cracks is observed which are normal to the surfacing direction (Figure 4, *b*, *d*). Further deposition of new layers causes cracking both in the layers proper and in the previously deposited layers. It may be related to a much higher heat input at pulse current feed than at GMAW-CMT process.

Microstructural analysis of samples was performed on sections enclosing three zones of deposition: last deposited layer, transition zone of fusion of the last and previous layer, and previous layers.

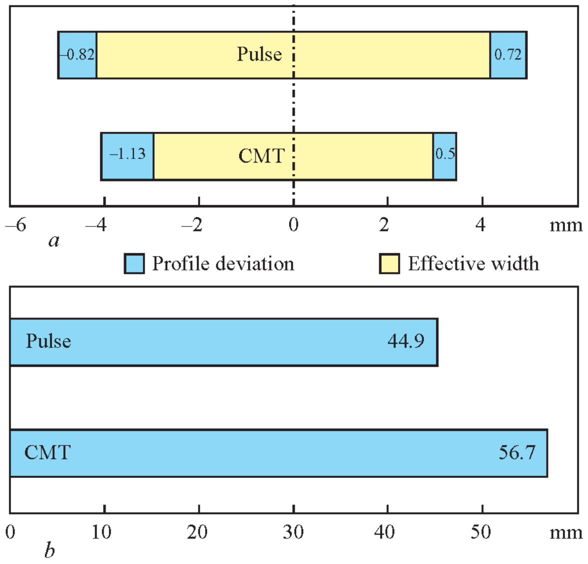

Figure 5. Parameters of the dependence of effective wall thickness (*a*) and effective height (*b*) for different methods of additive GMAW-CMT/pulse surfacing

Fine nonmetallic inclusions of an irregular shape and isolated transparent inclusions of gray-blue colour looking like pores were found on the polished surface of the microsections in all the studied samples. Inclusions are mostly observed along the central axis over the entire height of the studied deposit zones (Figure 6, *a*–*d*). No critical defects were found on the surface of a sample deposited by GMAW-CMT process. The mechanism of silicate inclusion formation during bronze deposition is described in [16] and it is attributed to remelting of CuO and SiO_2 thin films, which appeared as a result of ingress of adsorbed oxygen into the weld pool melt from the previous deposited layer.

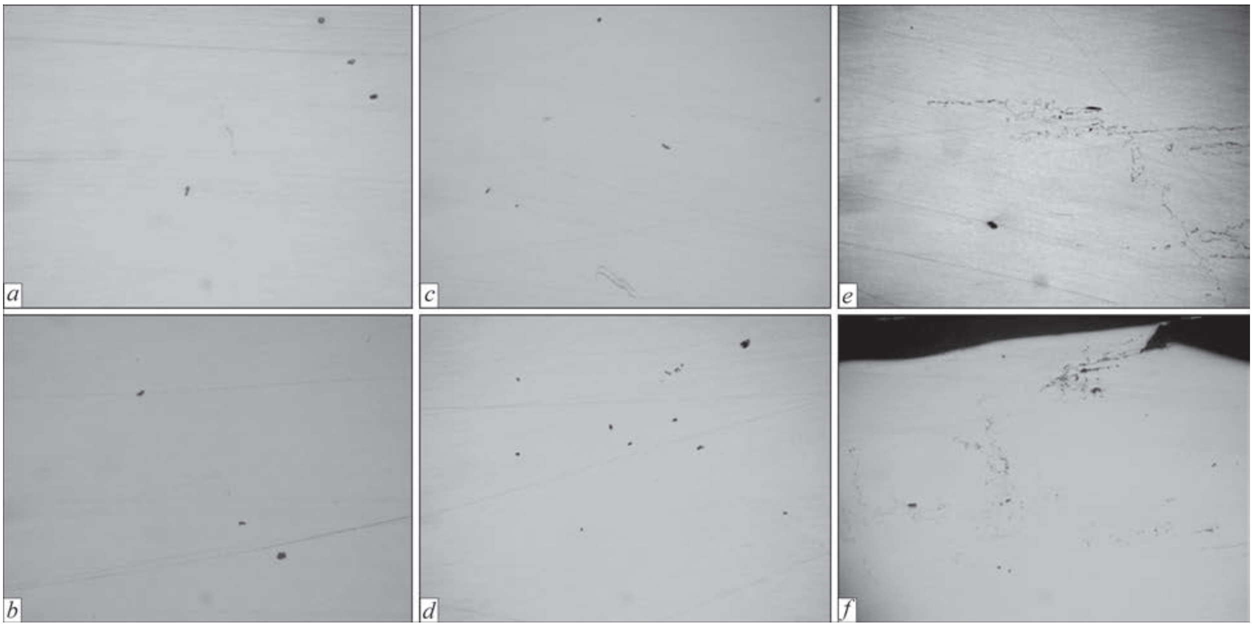

Figure 6. Macrostructures (×100) of samples of silicon bronze CuSi3Mn1 (BrKMts3-1) produced by different surfacing methods: *a*, *b* — GMAW-CMT; *c*, *d* — GMAW-Pulse; *e* — GMAW-Pulse, crack in the sample metal thickness; *f* — GMAW-Pulse, cracking from bead side edge

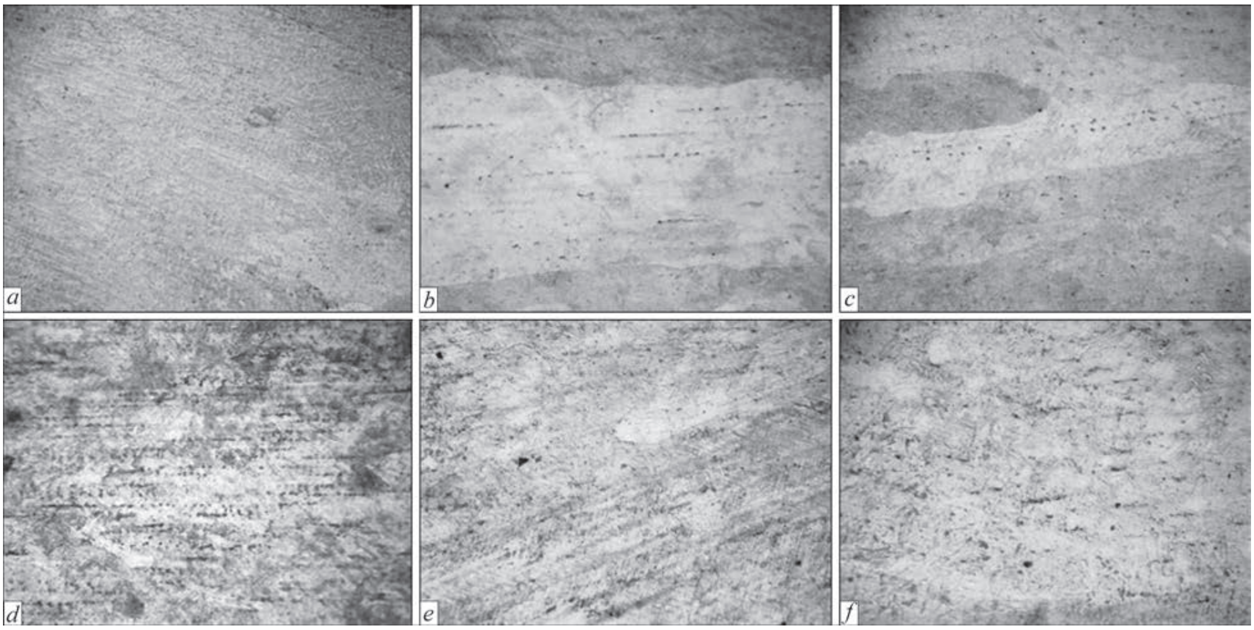

Figure 7. Microstructures (×800) of samples of silicon bronze CuSi3Mn1(BrKMts3-1) produced by different surfacing methods: *a–c* — GMAW-CMT; *d–f* — GMAW-Pulse; *a*, *d* — last deposited layer; *b*, *e* — transition zone; *c*, *f* — previous layers

On the surface of a sample deposited by GMAW-Pulse method numerous microcracks were found both near the side edge (Figure 6, *f*) and closer to the deposited bead center. Microcracks are also observed, which begin at the distance of approximately 6000 μm from the upper edge of the deposited bead and end in the region of the last layer (Figures 6, *e* and 8, *a*, *b*).

Metal of samples produced by GMAW-CMT/Pulse surfacing methods, consists of α-solid solution. For GMAW-CMT method the structure of the last layer is characteristic for multilayer deposits: columnar structure of cast metal points to crystallization direction, and is a fine dendritic structure (Figure 8, *a*). The transition zone structure consists of massive grains elongated along the specimen height and traces of primary structure in the form of intermittent strings of dark globular precipitates of subgrains of 100–150 μm size and substructures with a pronounced orientation (Figure 7, *b*). Structure of previous layers is similar to the transition zone and the last layer. However, a small quantity of a structure with a pronounced orientation appears also in light grains (Figure 7, *c*).

The structure of the last layer of samples produced by GMAW-Pulse surfacing differs from CMT process. No dendritic structure is observed in the last layer. Remains of cast metal in the form of intermittent bands and light matrix are present in the structure. A substructure in the form of plates of a pronounced orientation is observed in some regions of the light matrix (Figure 7, *d*). Structure of the transition layers is similar to the structure characteristic for GMAW-CMT surfacing (Figure 7, *e*). Previous layers have a structure similar to previous zones, remains of cast crystallites and massive grains with different degree of etching are present (Figure 7, *f*). In darker grains the same substructure is observed, as in the transition zone of layer fusion.

In the macrosection of a sample (Figure 4, *d*) deposited with pulse current feed one can see clear interfaces of individual layers with formation of massive columnar grains, which are oriented in the heat removal direction. Such a structure confirms the conclusions reached in work [10] as to residual overheating of the

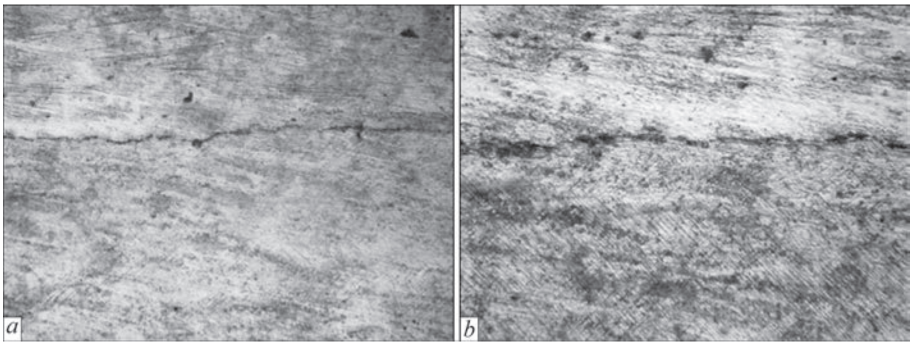

Figure 8. Structures (×200) of zones along the axis of the deposit produced by GMAW-Pulse method in the transition region (*a*) and the last layer (*b*)

weld pool with subsequent formation of an anisotropic structure of the deposited metal. Potentially, it can be the cause for appearance of critical defects of the type of cracks (Figure 8) at deposition of a sufficient number of layers with parallel accumulation of uncompensated tensile stresses from metal shrinkage at crystallization. GMAW-CMT process is characterized by a certain disorientation of the structure grains (Figure 4, *c*).

Microhardness of individual metal zones of the deposited samples is given in Table 2.

Microhardness of individual zones as a whole for Pulse surfacing, compared to CMT method, coincides with the authors' conclusions to some extent, which a given in work [8] in the context of increase of the deposited layer hardness at increase of the heat input.

FINITE ELEMENT MODELING

During creation of products by multilayer 3D printing, cracking can be the result of different factors. One of them is formation of thermal stresses, arising because of temperature difference between the layers during deposition. Technological parameters of the surfacing process also have an important role, in particular deposition rate, heat source power, and sequence of layer deposition. Inconsistency of any of these parameters may lead to cracking and other defects in the finished product.

Table 2. Average values of zonal microhardness of deposited samples, MPa

Surfacing method	Last layer	Transition zone	Previous layers
CMT	1190	1120	1190
Pulse	1160	1450	1400

Stress-strain state of the surfaced products depends on the kinetics of thermal deformation processes, occurring at deposition. At present the Goldak model of a 3D source with normal distribution of specific heat along all the coordinate axes in the heat flux, having the shape of an ellipsoid, is mainly used in research practice for analysis of thermal processes of arc welding and surfacing.

In order to analyze the stress-strain state and establish the possible causes of cracking in samples deposited by GMAW-Pulse process finite element modeling of layer-by-layer surfacing of a sample from silicon bronze CuSi3Mn1 on the substrate from austenitic stainless steel was performed.

Experimental model has the following geometrical parameters: length of the side of the triangle is 50 mm, substrate thickness is 6 mm, number of layers is 15, layer height (total height) is 1 mm (15 mm total). Material being deposited is CuSi3Mn1, substrate material is austenitic stainless steel AISI 304 (08Kh18N10).

Results of modeling the deposition process show that after achievement of 13–15 layers the level of equivalent and longitudinal normal tensile stresses arising along the trajectory of the torch movement grows significantly, as a result of reheating of previously deposited layers in the selected region (Fig-

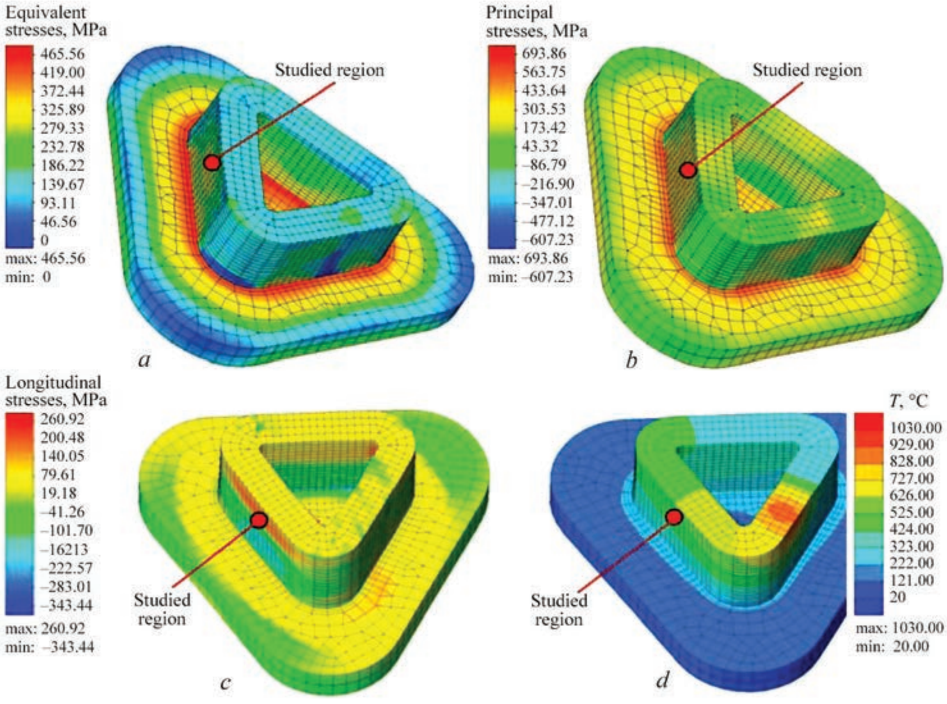

Figure 9. Fields of stress and temperature distribution: *a* — equivalent stresses (MPa); *b* — maximal principal stresses (MPa); *c* — normal stresses in the direction along the deposited layer (MPa); *d* — temperature distribution around the region of crack initiation after deposition of the 13th layer (°C)

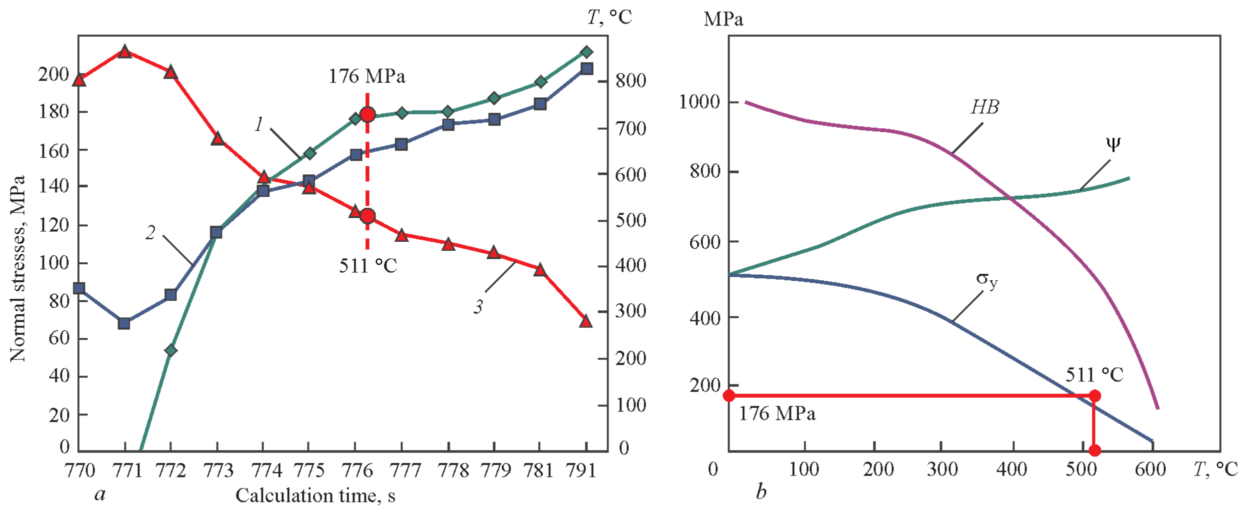

Figure 10. Graph of dependence of normal (*1*), equivalent stresses (*2*) and temperature (*3*) on time after deposition for the region of crack formation (*a*); change of mechanical properties of silicon bronze CuSi3Mn1 (BrKMts3-1), depending on temperature [4] (*b*)

ure 10, *a*). During multiple heating the level of longitudinal tensile stresses exceeds the bronze ultimate strength $\sigma_t \approx 140$ MPa and reaches $\sigma = 176$ MPa at actual temperature in the point of approximately 511 °C (Figures 9, *c* and 10, *a*, *b*).

This effect is observed as a result of reheating of previously deposited layers by the electric arc heat at deposition of the next bead. Analysis of the dependence of stress magnitude and distribution on temperature and time (Figure 10, *a*) shows that normal longitudinal tensile stresses reach the material ultimate strength in the temperature range of 550–490 °C (Figure 10, *b*), which leads to initiation of cracks detected at visual examination of shaping and metal structure.

CONCLUSIONS

The regularities of the influence of GMAW surfacing methods using the electric arc as the heat source on the change of geometrical characteristics and structure of stress-strain state components and probability of defect initiation at additive deposition of silicon bronze CuSi3Mn1were studied. Analysis of the derived data shows that:

1. Surfacing method (GMAW-CMT/Pulse) has an essential influence on geometrical characteristics of the deposited layers. The greatest height and minimal thickness of the deposited samples is ensured by GMAW-CMT method, which is related to smaller heat release, compared to GMAW-Pulse method. Reduction of the heat input leads to decrease of the depth of penetration into the previously deposited layers, lowering of weld pool metal temperature, shortening of the time of melt existence and, consequently, of its spreading.

2. No critical defects in the form of cracks or lacks-of fusion were found at application of GMAW-CMT process. An opposite result was obtained at application of arc Pulse process, in which initiation of transverse cracks along the entire length of the sample is recorded, after reaching the 30th deposited layer and higher. The geometrical shape of each layer, compared to CMT process, has greater width and smaller height of the bead.

3. Analysis of metal microstructure of samples produced by both the surfacing technologies points to formation of a single-phase structure of α-solid solution of a complex chemical composition. The structure of both the deposits mainly consists of massive grains with different degree of etching and orientation, which differ by their hardness. Grain microhardness differs in different deposit regions, and it is in the range of 876–1280 MPa for CMT and 1160–1460 MPa for the Pulse process.

4. The finite element modeling method revealed that crack formation in samples made by GMAW-Pulse method, is associated with greater heat input compared to GMAW-CMT surfacing, which leads to a significant increase in the level of longitudinal tensile stresses, reaching the material ultimate strength in the temperature range of 490–550 °C.

REFERENCES

1. Ding, D, Pan, Z, Cuiuri, D et al. (2016) Adaptive path planning for wire-feed additive manufacturing using medial axis transformation. *J. of Cleaner Production*, **133**, 942–952. DOI: https://doi.org/10.1016/j.jclepro.2016.06.036
2. Mukin, D., Valdaytseva, E., Hassel, T. et al. (2020) Modelling of heat transfer process in non-vacuum electron beam additive manufacturing with CuSi3 alloy wire. *Materials Today: Proceedings*, 30(**3**), 373–379. DOI: https://doi.org/10.1016/j.matpr.2019.12.380
3. Mukin, D.V., Ivanov, S.Yu., Valdaitseva, E.A. et al. (2019) An analytical model for filler wire heating and melting during wire feed laser deposition. *KEM*, **822**, 431–437. DOI: https://doi.org/10.4028/www.scientific.net/kem.822.431

4. Spittel, Marlene, Spittel, Thilo (2016) *Flow stress and plasticity of CuSi3Mn1*. DOI: http://dx.doi.org/10.1007/978-3-642-14174-4_62
5. Yanhu, W., Xizhang, C., Sergey, K. et al. (2019) In-situ wire-feed additive manufacturing of Cu–Al alloy by addition of silicon. *Applied Surface Sci.*, **487**, 1366–1375. DOI: https://doi.org/10.1016/j.apsusc.2019.05.068
6. Kun, L. et al. (2019) Location dependence of microstructure and mechanical properties of Cu–Al alloy fabricated by dual wire CMT. *Materials Research Express*, 6(**12**). DOI: https://doi.org/10.1088/2053-1591/ab583e
7. Wang, Y., Konovalov, S., Chen, X. et al. (2021) Research on Cu–6.6 % Al–3.2 % Si alloy by dual wire arc additive manufacturing. *J. of Materials Eng. and Performance*, **30**, 1694–1702. DOI: https://doi.org/10.1007/s11665-021-05470-4
8. Kazmi, K.H., Sharma, S.K., Das, A.K. et al. (2023) Development of wire arc additive manufactured Cu–Si alloy: Study of microstructure and wear behavior. *J. of Materials Eng. and Performance*. DOI: https://doi.org/10.1007/s11665-023-07972-9
9. Kvasnytskyi, V.V., Lahodzinskyi, I.M. (2023) Influence of GMAW and PAW methods of additive arc surfacing and shielding gas composition on surface geometry and metal structure. *Avtomatych. Zvar.*, **11**, 23–31. DOI: https://doi.org/10.37434/as2023.11.02
10. Baby, J., Amirthalingam, M. (2020) Microstructural development during wire arc additive manufacturing of copper-based components. *Welding in the World*, **64**, 395–405. DOI: https://doi.org/10.1007/s40194-019-00840-y
11. Gang, M., Xueming, H., Ye, H. et al. (2020) Study on the microstructure optimization and mechanical properties of dissimilar TC4-304L arc-brazing joints. *Materials Sci. and Eng.: A*, **788**. DOI: https://doi.org/10.1016/j.msea.2020.139566
12. Donghong, D., Zengxi, P., Dominic C. et al. (2016) Adaptive path planning for wire-feed additive manufacturing using medial axis transformation. *J. of Cleaner Production*, **133**, 942–952. DOI: https://doi.org/10.1016/j.jclepro.2016.06.036
13. Yu, Z.S., Li, R.F., Zhou, F.M. et. al. (2004) Joint evolution and strengthening mechanisms in arc brazed galvanised steels with Cu97Si3 filler. *Materials Sci. and Technol.*, 20(**11**), 1479–1483. DOI: https://doi.org/10.1179/026708304225022133
14. Kvasnytskyi, V., Korzhyk, V., Lahodzinkyi, I. et al. (2020) Creation of volumetric products using additive arc cladding with compact and powder filler materials. In: *Proc. of IEEE 10th Inter. Conf. on Nanomaterials: Applications & Properties*, 02SAMA16-1–02SAMA16-5. DOI: https://doi.org/10.1109/NAP51477.2020.9309696
15. Gurcik, T., Kovanda, K., Rohan, P. (2019) Influence of shielding gas on geometrical quality of WAAM technology. In: *Proc. of METAL 2019 of 28th Inter. Conf. on Metallurgy and Material*, 715–721. DOI: https://doi.org/10.37904/metal.2019.871
16. Mou, G., Hua, X., Wu, D. et al. (2017) Study on weld seam surface deposits of CuSi3 CMT brazing. *The Inter. J. of Advanced Manufacturing Technology*, **92**, 2735–2742. DOI: https://doi.org/10.1007/s00170-017-0349-3

ORCID

A.O. Perepichay: 0000-0002-8156-4515,
I.M. Lahodzinskyi: 0000-0002-7986-9440

CONFLICT OF INTEREST

The Authors declare no conflict of interest

CORRESPONDING AUTHOR

A.O. Perepichay
National Technical University of Ukraine
“Igor Sikorsky Kyiv Polytechnic Institute”
37 Prospect Beresteiskyi (former Peremohy),
03056, Kyiv, Ukraine.
E-mail: perepichayandrey@gmail.com

SUGGESTED CITATION

A.O. Perepichay, I.M. Lahodzinskyi (2024) Study of the influence of GMAW-CMT and pulse processes of additive deposition of silicon bronze CuSi3Mn1 on the geometrical characteristics of the surface, structure and stress-strain state of finished products. *The Paton Welding J.*, **4**, 23–31.

JOURNAL HOME PAGE

https://patonpublishinghouse.com/eng/journals/tpwj

Received: 06.12.2023
Received in revised form: 15.01.2024
Accepted: 30.04.2024

DOI: https://doi.org/10.37434/tpwj2024.04.05

STRUCTURE AND MECHANICAL PROPERTIES OF THICK COPPER CONDENSATES, DISPERSION-STRENGTHENED WITH CHROMIUM, ZIRCONIUM OXIDE AND THEIR MIXTURE

A.V. Demchyshyn, A.A. Demchyshyn, S.P. Egorov

[1]Frantsevich Institute for Problems of Materials Science of the NASU
3 Omelyan Pritsak Str. 03142, Kyiv, Ukraine
[2]National Technical University of Ukraine “Igor Sikorsky Kyiv Polytechnic Institute”
37 Beresteiskyi Prosp. (former Peremohy), 03056, Kyiv, Ukraine

ABSTRACT

The structure and mechanical properties of copper condensates with a thickness of 0.8–2.0 mm, dispersion-strengthened with chromium, zirconium oxide and their mixture, obtained by simultaneous electron beam evaporation of the selected components with subsequent condensation of the vapor phase onto flat steel substrates, were investigated. It is shown that the characteristics of the structure and the level of strength of the composites depend on the volumetric content of the strengthening phase, its dispersion and total action of the dispersoids.

KEYWORDS: electron beam vapour phase technology, thick vacuum condensates, copper, copper-chromium, copper-oxide, copper-chromium-zirconium oxide systems, microstructure, hardness, strength, ductility

INTRODUCTION

Copper-based composite materials are widely used in different sectors of modern industry, owing to a favourable combination of mechanical, thermal, thermal-physical and electric properties in such compositions, for instance, contacts of electrical equipment, electric motor commutators, electrodes for contact, spot and seam welding, part surfaces with a high resistance to arc erosion and wear at sliding friction, working surfaces of powerful laser mirrors, targets for neuron irradiation, etc [1–4]. Both metal (Cr, Mo, Nb, Be, Zr) and ceramic (Al_2O_3, ZrO_2, Y_2O_3, ThO_2, SiC, TiB_2, AlN) materials are used as strengthening phases in copper compositions. At the same time, dispersion-strengthening copper alloys (for instance chromium bronzes), have certain disadvantages, such as a significant lowering of hardness and strength at higher temperatures that considerably limits their application. On the other hand, such dispersion-strengthened copper alloys, as Cu–Al_2O_3, Cu–ZrO_2, demonstrate higher values of mechanical properties at higher temperatures that ensures a wider application of such compositions [5], which are usually produced by different powder metallurgy methods.

The objective of the proposed work is investigation of the structure and mechanical properties of Cu–Cr and Cu–ZrO_2 copper compositions, produced by electron beam vapour-phase technology, as well as studying the combined influence of two mechanisms of copper matrix strengthening by Cr and ZrO_2 particles on similar characteristics of binary systems.

EXPERIMENTAL MATERIALS AND PROCEDURE

Composite materials of Cu–Cr, Cu–ZrO_2 and BrKh0.5–ZrO_2 systems in the form of 120×200×(0.8–2.0) mm plates with a variable content of the dispersed phase along their length were produced by simultaneous electron beam evaporation of copper or BrKh0.5 bronze and the strengthening phase from two independent water-cooled copper crucibles with further condensation of the vapour mixture on the steel substrates. The block diagram of this method is shown in work [6]. Used as initial materials were copper ingots of 69 mm diameter and 160–200 mm length, produced by electron beam remelting of copper of M0 grade, ingots of BrKh0.5 chromium bronze and chromium of VKh-1 grade of 49 mm diameter and 80–90 mm length, as well as compacted from commercially pure ZrO_2 + 5 % CaO powder and sintered cylinders of 49 mm diameter and 60 mm height. The substrate temperature was 750 °C, which was selected with the purpose of producing optimal mechanical properties and structure of the metal matrix. The metal condensation rate was 5–7 μm/min, and for zirconium oxide it was 1.6–2.4 μm/min. The vacuum value was $(1.33\cdot10^{-2})$–$(0.66\cdot10^{-3})$ Pa. A thin layer of zirconium dioxide was pre-deposited on the substrates, in order to separate the condensates from them. The amount of the second phase in the condensates was determined by the chemical method.

Metallographic investigation of the condensate structure was conducted using MIN-7 and MIM-8 optical microscopes. The shape and dimensions of the second phase particles were studied in JEM-120 electron microscope. Mechanical properties of the condensates were determined by stretching the flat samples with 3 mm width and 10 mm length of the working part. The relative strain rate was $1.67\cdot10^{-3}$ s^{-1}. Vickers hardness was measured in KhPO-250 instrument at 10 kg load for 30 s.

INVESTIGATION RESULTS

Cu–Cr *SYSTEM*

When considering the copper-chromium system it should be noted that in keeping with the constitutional diagram, the solubility of chromium in solid copper is quickly reduced with temperature lowering, and it is equal to 0.15 and 0.03 vol.% at 750 and 20 °C, respectively. Thus, in the presence of chromium in the above-mentioned amounts in copper in a slightly diluted solid solution of copper-chromium it will have the form of dispersed particles. Chromium content in copper in this study varied in the range from 0 to 3.0 vol.% Cr.

Metallographic investigation of the transverse microsections of Cu–Cr condensates allowed determination of the influence of the amount of strengthening chromium additive on the microstructural pattern of the two-phase condensate. Figure 1 shows the structures of copper-chromium vacuum condensates with Cr content from 0.3 to 2.7 vol.% produced at substrate temperature of 750 °C.

Comparison of the given structures with the microstructure of pure copper condensate formed at the same temperature shows that addition of even a small amount of chromium to copper leads to a significant reduction of the matrix crystallite size. For instance, at chromium content of 0.3 vol.% the size of Cu–Cr condensate grains is reduced 3 times. Increase of the concentration of the strengthening chromium phase causes further structure refinement and at chromium content of 2.7 vol.% and higher, the elements of the condensate microstructure become so dispersed that large magnifications have to be used to detect them (Figure 1, *e*, ×900).

Transmission electron microscopy studies of specially prepared foils of Cu–Cr condensates allowed determination of the size and shape of the dispersed chromium particles, depending on the amount of strengthening phase added to the copper matrix. Proceeding from experimental data, we can come to the conclusion that chromium particles are of a round shape and their size becomes larger with increase of the second phase concentration. For instance, while at 0.3 vol.% Cr content in copper the size of the strengthening particles is close to 30 nm, at the second phase amount of 2.5 vol.% the particle size becomes 7 times larger and it is equal to 210 nm. Figure 2 shows electron microscopy images of the structures of Cu–Cr condensates at different chromium concentrations.

The second phase greatly increases the copper hardness. Addition of chromium in the amount of 0.5 % increases the vacuum condensate hardness 1.5 times. At further increase of chromium concentration to 2.7 vol.%, the hardness increases in proportion to the strengthening phase content (Figure 3). Comparison of the hardness of Cu–0.5 % Cr condensate with

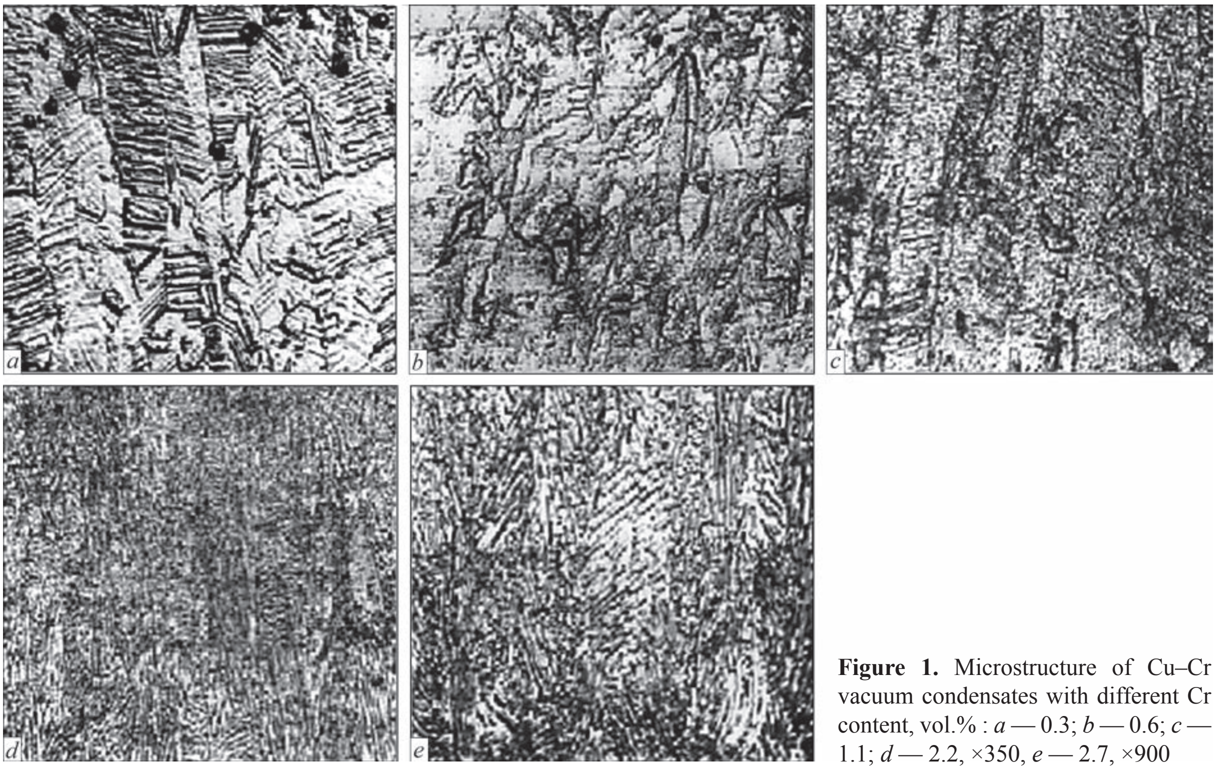

Figure 1. Microstructure of Cu–Cr vacuum condensates with different Cr content, vol.% : *a* — 0.3; *b* — 0.6; *c* — 1.1; *d* — 2.2, ×350, *e* — 2.7, ×900

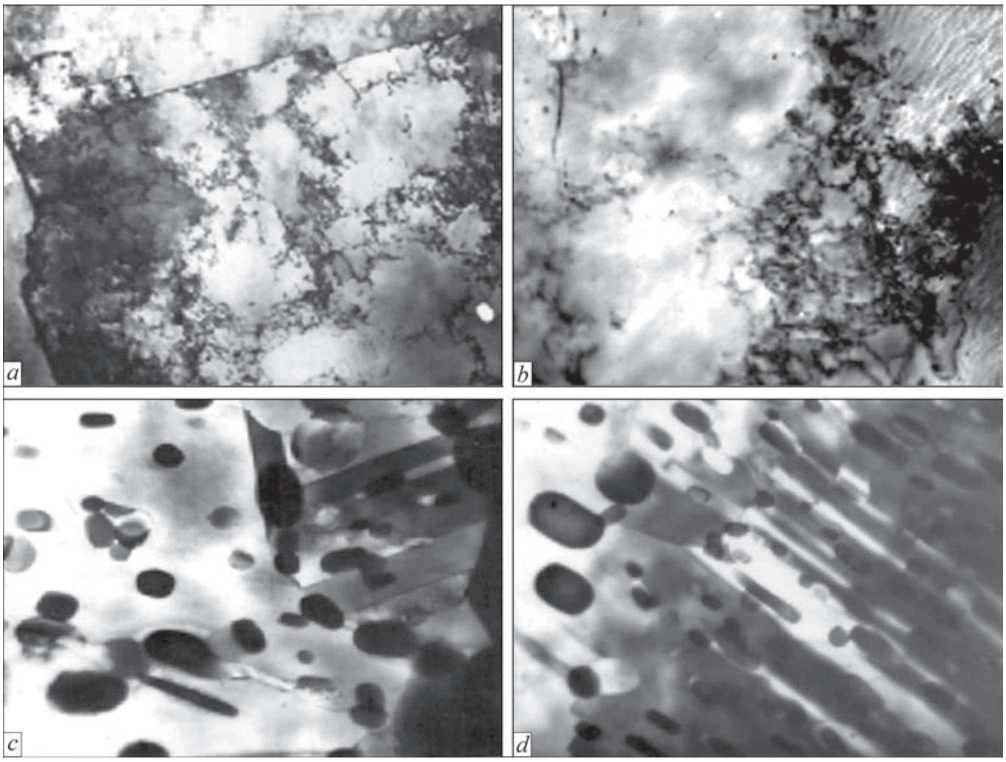

Figure 2. Structure of Cu–Cr condensates with different Cr content, vol.%: *a* — pure copper; *b* — 0.3; *c* — 2.5; *d* — 3.4, ×40000

that of BrKh0.5 chromium bronze produced by casting, is indicative of practical coincidence of absolute hardness values of the condensed chromium bronze (603 MPa) with that of bulk bronze after hardening (637 MPa) [7, 8].

Tensile mechanical properties of condensates of Cu–Cr system were determined at room temperature and 700 °C in air and in vacuum of $5\cdot10^{-5}$ mm Hg, respectively. Derived dependencies on strengthening phase content are shown in Figure 4. Strength characteristics of the two-phase condensates become higher with increase of chromium content. Chromium addition to copper in the amount of 3.2 vol.% increases the ultimate strength and yield limit by 1.9 and 2.0 times, respectively. Ductility of the two-phase condensates rises somewhat at addition of small amounts of chromium (up to 0.6–0.8 vol.%) into the copper matrix. At further increase of strengthening phase content, relative elongation decreases quickly and reaches 21 % at 3.2 vol.% chromium.

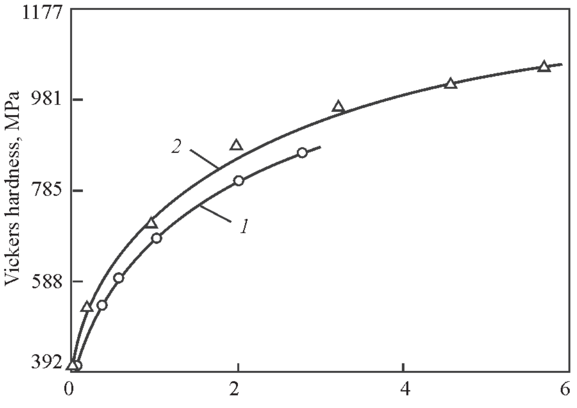

Figure 3. Dependence of hardness of condensates of Cu–Cr (*1*) and Cu–ZrO_2 (*2*) systems on strengthening phase content

Comparison of ultimate strength, yield limit and relative elongation of Cu–0.5 % Cr condensates with similar characteristics of BrKh0.5 chromium bronze, produced by casting or powder metallurgy, is indicative of practical coincidence of absolute values of the above-mentioned mechanical properties of the condensed chromium and bulk bronzes in the hardened condition [7, 8].

Tensile tests at 700 °C indicate an increase of ultimate strength and yield limit with increase of chromium content to 0.8 vol.%. Further increase of chromium content leads to lowering of strength characteristics. Relative elongation of Cu–Cr condensates decreases from 41 to 21 % with increase of strengthening phase content to 0.8–1.0 vol.%, and then it increases in proportion to increase of chromium content. At 2.5 % chromium elongation of Cu–Cr condensates reaches 36 %.

The noted lowering of strength characteristics at simultaneous increase of ductility of condensates with chromium content in the range of 0.8–2.5 vol.% should be associated with coagulation of chromium particles as a result of a combined action of temperature (700 °C) and deformation. This fact is indicative of a comparatively low thermal stability of Cu–Cr materials at such temperature.

Cu–ZrO_2 *SYSTEM*

Metallographic investigations of Cu–ZrO_2 condensates indicate that addition of ZrO_2 oxide to copper leads to reduction of the size of the crystallites in the matrix and formation of a columnar structure (Figure 5), as in the case of chromium addition. Oxide content in copper was varied in the range of 0–4.0 vol.% ZrO_2 in this study. The most marked grain refinement is observed in the region of second phase content of 0.2–0.7 vol.%. For instance, at oxide content of 0.6 vol.% in copper the composite grain size decreases 3.5 times, compared to the size of crystallites of pure condensed copper, formed at the same substrate temperature (750 °C). Increase of oxide phase content causes further refinement of the structure of copper-oxide composite, however, the rate of this process slows down significantly. At oxide content of 3–4 vol.% the condensate microstructure elements become so dispersed, that their detection requires application of high magnifications (Figure 5, *d*, ×900).

X-ray investigations of two-phase condensates of copper-zirconium oxide showed that the dioxide phase lines are not detected in the studied range of the second phase concentrations, copper lines are not blurred, and the matrix lattice parameter does not change depending on oxide content, and it coincides with that of pure copper condensate lattice. This is indicative of a practical absence of phase interaction at formation of condensates of Cu–ZrO_2 system. Absence of oxide lines in the roentgenograms can be accounted for by weak intensity of reflection of this refractory compound from the crystallographic planes and their subsequent absorption, in view of the small amount of the second phase in the composition. Transmission electron microscopy studies of foils of

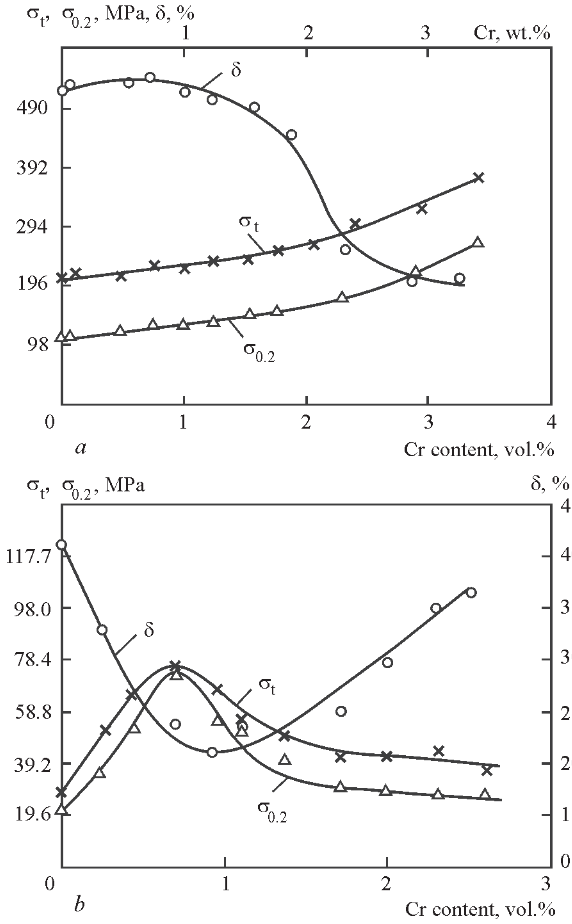

Figure 4. Dependence of mechanical properties of Cu–Cr condensates on the amount of strengthening phase at test temperatures , °C: *a* — 20; *b* — 700

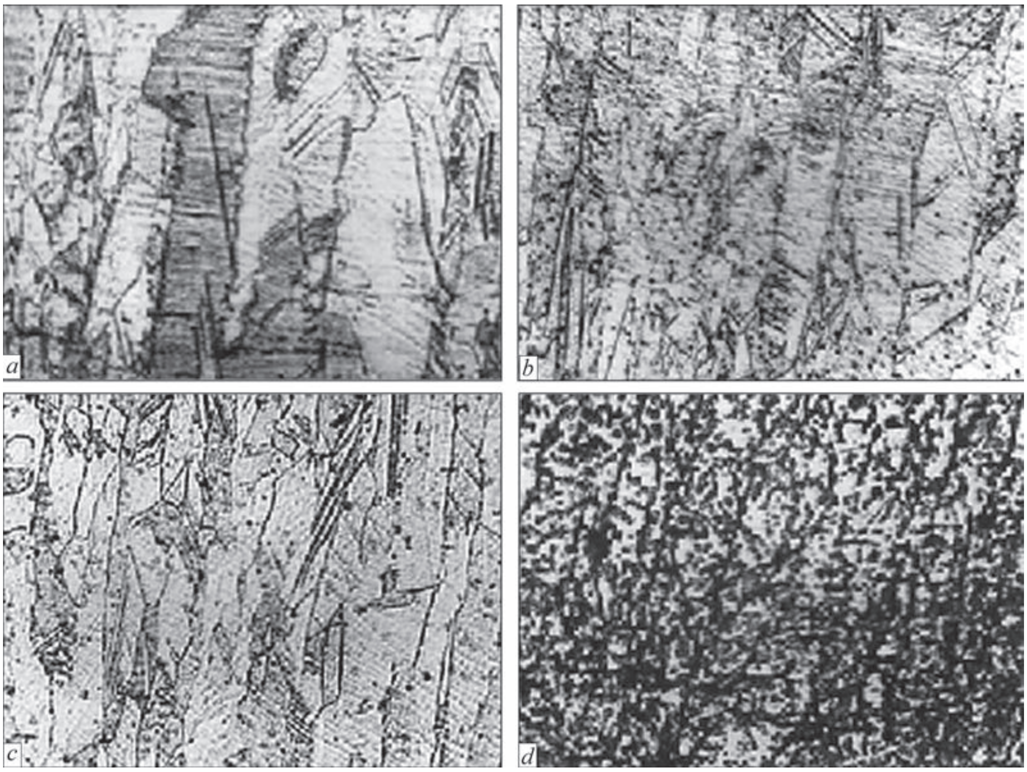

Figure 5. Microstructure of Cu–ZrO_2 vacuum condensates with different ZrO_2 content, vol.%: *a* — 0.2; *b* — 0.3; — 0.5, ×350; *d* — 4.0, ×900

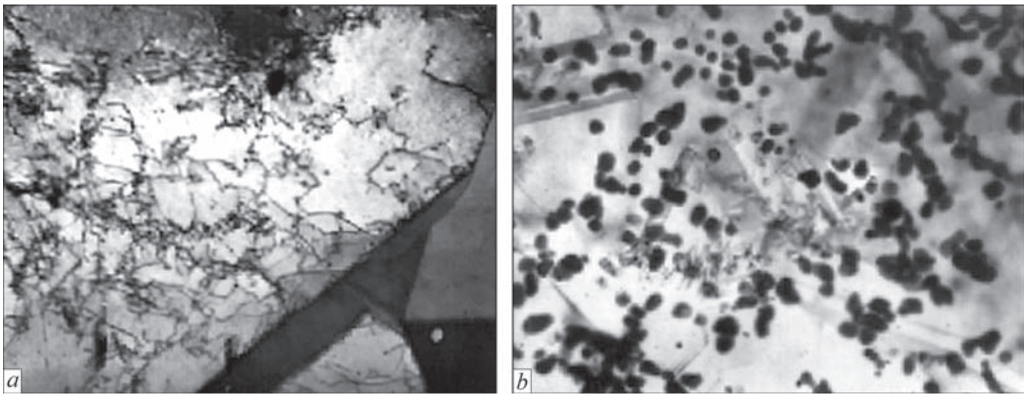

Figure 6. Microstructure of Cu–ZrO_2 condensates with different ZrO_2 content, vol.%: *a* — 0.3; *b* — 2.5, ×40000

Cu–ZrO_2 condensates showed that oxide particles are of a spheroidal shape and have rather uniform size (Figure 6). The size of strengthening particles also increases with increase of oxide content, similar to the case of copper-chromium composition.

It should be noted that at a small amount of ZrO_2 phase (up to 0.8 vol.%), the oxide particles have larger dimensions, compared to chromium particles. For instance, at the second phase concentration of 0.3 vol.% the size of oxide and chromium particles is 60 and 30 nm, respectively. However, the growth rate of dispersed particles with increase of the second phase amount is much lower in copper-oxide compositions, compared to Cu–Cr condensates. As a result, at the second phase content above 0.8 vol. % the size of chromium particles will start exceeding the size of oxide particles and at the second phase content of 3.4 vol.% chromium particles become much larger than oxide particles. The noted fact is attributable to a different extent of the second phase interaction with the copper matrix and different diffusion mobility of the strengthening phases in copper at formation of the condensed composition at the temperature of 750 °C, and chromium phase precipitation from the parent material in the matrix volume at substrate cooling from 750 °C to room temperature.

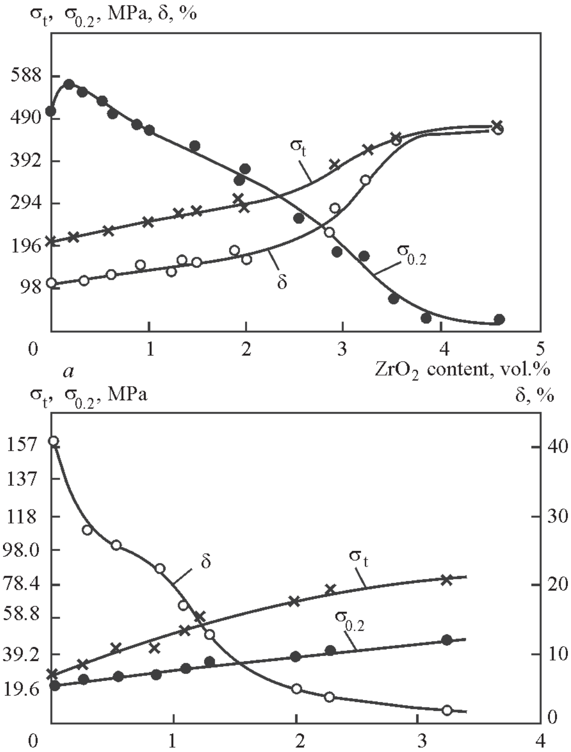

Figure 7. Dependence of mechanical properties of Cu–ZrO_2 vacuum condensates on strengthening phase content at test temperatures, °C: *a* — 20; *b* — 700

Addition of zirconium dioxide particles into copper causes an increase of its hardness from 40 for pure copper to 107 kg/mm^2 at 5.7 vol.% of oxide (Figure 3). Concentrational dependence of hardness of copper-oxide compositions is similar to hardness dependence on the phase amount for condensates of Cu–Cr system. The absolute hardness values of copper-oxide condensates, however, are somewhat higher at the same volumetric content of the strengthening phase. Comparison of the hardness of Cu–0.5 vol.% ZrO_2 condensate with that of samples of a similar composition, produced by powder metallurgy method of inner oxidation with further hot extrusion and cold drawing by 56 % is indicative of practical coincidence of absolute values [9, 10].

Mechanical properties of Cu–ZrO_2 condensates were determined at room temperature in air and at 700 °C in the vacuum of $5 \cdot 10^{-5}$ mm Hg. Derived dependencies are given in Figure 7. Addition of zirconium oxide particles into the copper matrix leads to increase of ultimate strength and yield limit of the two-phase condensates at simultaneous lowering of their ductility.

Concentrational dependence of strength of Cu–ZrO_2 condensates at room temperature is similar to the dependence of strength characteristics on the strengthening phase amount for condensates of Cu–Cr system. However, absolute values of ultimate strength and yield limit of the copper-oxide system are somewhat higher. At test temperature of 700 °C strength characteristics of Cu–ZrO_2 condensates also become higher with increase of oxide content in the studied range of second phase concentrations, and ductility decreases.

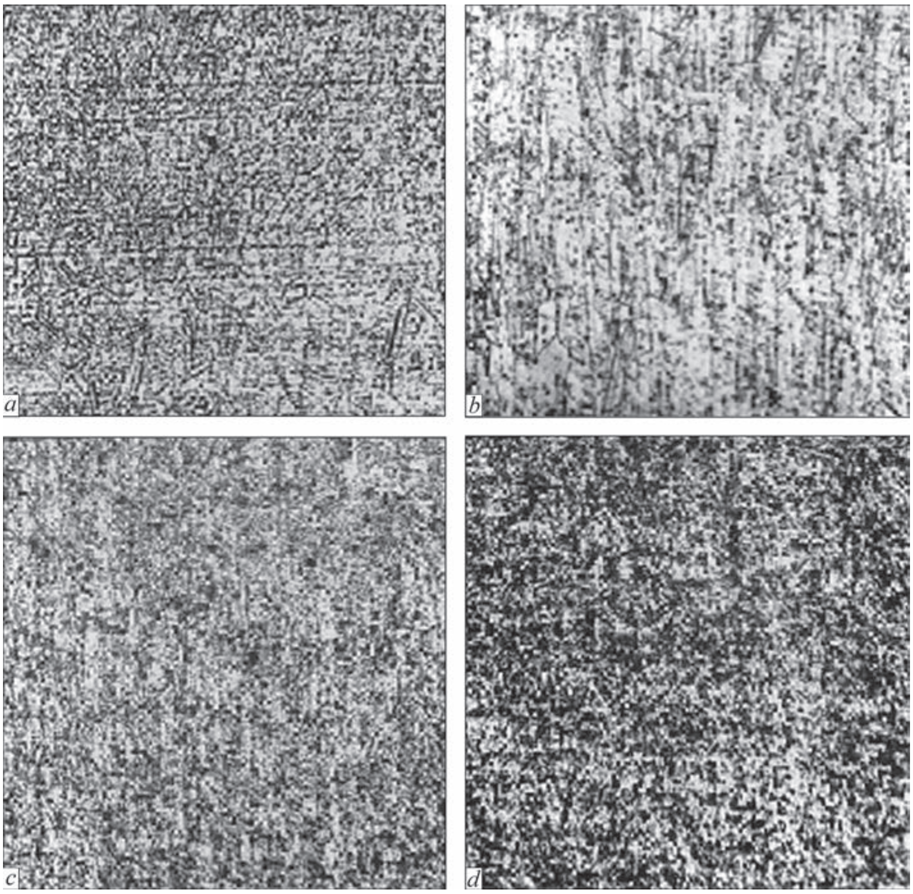

Figure 8. Microstructure of BrKh0.5–ZrO_2 vacuum condensates with different ZrO_2 content, vol.%: *a* — 0.7; *b* — 1.7; *c* — 3.65, ×350; *d* — 5.7, ×900

Comparison of mechanical properties of condensates of Cu–Cr and Cu–ZrO_2 systems at test temperature of 700 °C shows that no drop of strength characteristics is observed in copper-oxide compositions with increase of the strengthening phase content in the concentration range above 0.8 vol.%, as in the case of Cu–Cr system, which is indicative of a higher thermal stability of copper-oxide condensates. This fact leads to the conclusion that in terms of operational reliability under the conditions of long-term action of higher temperatures the condensates of Cu–ZrO_2 system have an advantage over Cu–Cr system condensates. It is also known that dispersion-strengthened materials with a stable strengthening phase have extremely low creep rates at high temperatures.

Cu–0.5Cr–ZrO_2 *SYSTEM*

Metallographic studies of condensates of pure BrKh0.5 chromium bronze produced by electron beam evaporation from one crucible, showed that at its evaporation in a stable mode a condensate forms on the substrate with a structure, similar to the one obtained at simultaneous evaporation of pure copper and chromium from two crucibles. It allowed producing three-phase condensates of Cu–0.5Cr–ZrO_2 system with varying oxide content.

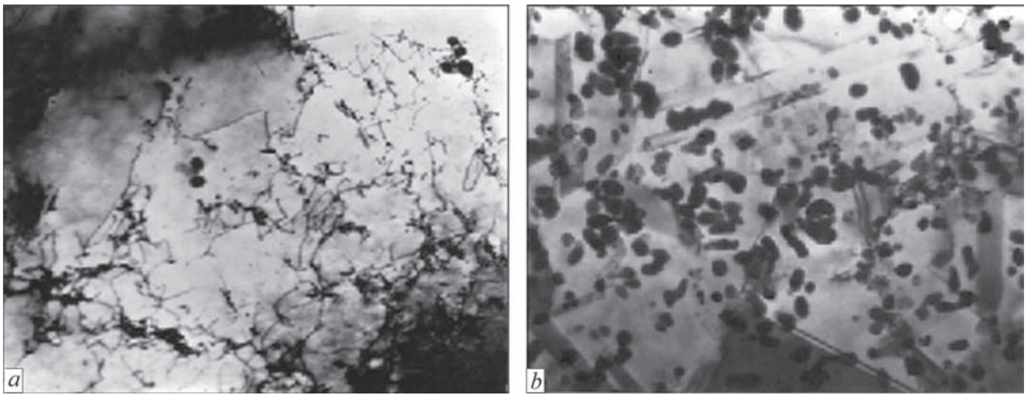

Figure 9. Structure of BrKh0.5–ZrO_2 condensates with different ZrO_2 content, vol.%: *a* — 0.3; *b* — 4.8, ×4000

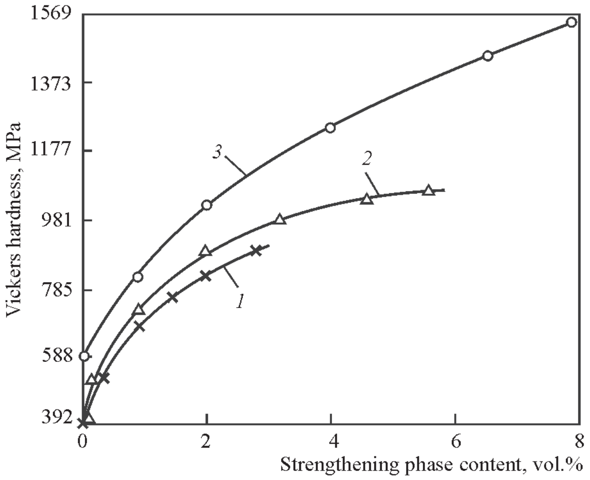

Figure 10. Dependence of hardness of the studied copper condensates on the content of Cu–Cr (*1*), Cu–ZrO_2 (*2*), BrKh0.5 (*3*) strengthening phase

Addition of oxide phase to chromium bronze leads to further refinement of its structure (Figure 8). At 1.0 vol.% oxide content the grain size of bronze-oxide condensate decreases two times, compared to the size condensed bronze crystallites formed at the same substrate temperature (750 °C). Further increase of oxide concentration promotes refinement of the structure of bronze-oxide composite. However, the growth rate of such a process becomes somewhat slower.

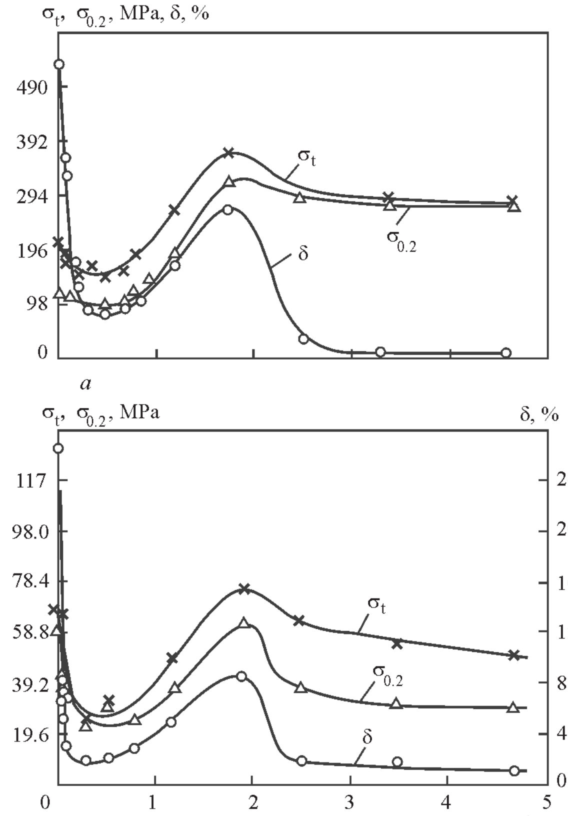

Figure 11. Dependence of mechanical properties of BrKh0.5–ZrO_2 condensates on ZrO_2 content at test temperatures, °C: *a* — 20; *b* — 700

Transmission electron microscopy studies showed that simultaneous presence of strengthening particles of chromium and zirconium oxide in the copper matrix does not influence their morphology at different oxide content (Figure 9). As in the case of copper-based two-phase systems, an increase of the strengthening phase dimensions with increase of its content is also observed in three-phase condensates.

Addition of oxide particles to chromium bronze leads to an increase in its hardness from 60 to 160 kg/mm^2 at 8 vol.% of the oxide (Figure 10), which exceeds the hardness of cast BrKh0.5 chromium bronze after dispersion hardening and 25 % cold deformation (150 kg/mm^2) [7].

Tensile mechanical properties of three-phase condensates were determined at room temperature in air and at 700 °C in the vacuum of $5 \cdot 10^{-5}$ mm Hg (Figure 11). As one can see from the presented graphs, the concentrational dependencies of ultimate strength, yield limit and ductility of dispersion-strengthened bronze are characterized by the presence of a minimum at oxide content of 0.5 vol.%. Test temperature and ambient atmosphere do not influence its position. Simultaneous lowering of strength and ductility of BrKh0.5 bronze at increase of oxide content in it from 0 to 0.5 vol.% is attributable to unfavourable arrangement of the two types of dispersed particles on grain boundaries. Increase of oxide content from 0.5 to 1.8–2.0 vol.% results in an increase of the condensate mechanical properties, but their absolute values do not exceed those for condensates of Cu–Cr system. Further increase of oxide content lowers the mechanical characteristics of three-phase condensates, which is, most probably, due to brittle fracture of the samples.

DISCUSSION OF THE RESULTS

Addition of chromium or zirconium oxide in the amount of 0 to 0.8 vol.% leads to refinement of the copper matrix structure, somewhat more abrupt in the

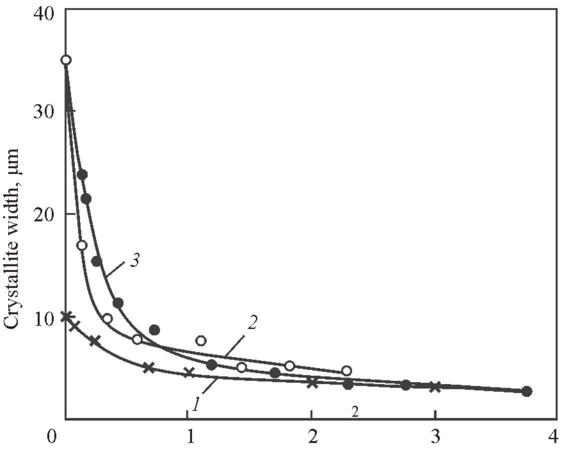

Figure 12. Dependence of crystallite width of the studied copper-based condensates on strengthening phase content: *1* — Cu–0.5 % Cr–ZrO_2; *2* — Cu–Cr; *3* — Cu–ZrO_2

case of chromium (Figure 12). At higher concentrations of the second phase the pattern is reversed, that is attributable to higher dispersion of chromium particles at small amounts of this phase (up to 0.8 vol.%) and higher rate of their coagulation with increase of chromium content. Larger particles have a weaker influence on the structure. Simultaneous addition of strengthening particles of chromium and zirconium oxide to the metal matrix causes a summary refinement of the composite structure.

Hardness measurements of the studied systems indicate that the oxide particles more actively increase the hardness of the two-phase composition, than chromium particles do (Figure 10). At simultaneous addition of chromium and oxide particles to the matrix, the material hardness is increased more intensively, compared to the two-phase compositions that promotes its better polishability.

Investigations of tensile mechanical properties of the composites showed that dispersion-strengthened condensates of Cu–ZrO_4 system have better strength characteristics, compared to dispersion-hardening condensates of Cu–Cr system, particularly at higher test temperatures (700 °C), which is equal to $0.7T_m$ of the matrix. Mechanical tests of three-phase copper-chromium-zirconium oxide condensates did not reveal any evident advantages of metal matrix strengthening by two types of particles, compared to two-phase Cu–Cr and Cu–ZrO_2 condensates.

CONCLUSIONS

1. Cu–Cr, Cu–ZrO_2 and Cu–Cr–ZrO_2 compositions were produced by the method of electron beam evaporation with subsequent vapour mixture condensation on steel substrates.

2. Dispersion-strengthened Cu–ZrO_2 systems have better strength characteristics, compared to dispersion-hardening Cu–Cr alloys.

3. A combination of two types of simultaneous strengthening of the copper matrix by coherent (Cr) and non-coherent (ZrO_2) particles did not show any advantages, compared to two-phase Cu–Cr and Cu–ZrO_2 alloys.

REFERENCES

1. Sami Abualnoun Ajeel, Rabiha S. Yaseen, Asaad Kadhim Eqal (2019) Characterization of micro-structure and mechanical properties of CuCr alloy produced by stir casting. *Diyala J. of Eng. Sci.*, 12(**4**), 82–91. DOI: https://10.26367/DJES/vol.12/NO.4/9
2. Yuan, Yuan, Zhou, Li, Zhu, Xiao et al. (2017) Microstructure evolution and properties of Cu–Cr alloy during continuous extrusion process. *J. of Alloys and Compounds*, **703**, 454–460. DOI: https://10.1016/J. JALLCOM.2017.01.355
3. YuSong, Xu, CuiPing, Jin, Peng, Li, YunHua, Xu. (2014) Microstructure and properties of the dispersion-strengthened Cu–ZrO_2 composite for application of spot-welding electrodes. *J. Advanced Materials Research*, **887–888**, 32–38.
4. Wilms Marcus, B., Rittinghaus Silja-Katharina (2022) Laser additive manufacturing of oxide dispersion-strengthened copper–chromium–niobium alloys. *J. Manufacturing and Materials Processing*, **6**, 102–116. DOI: https://doi.org/10.3390/jmmp6050102
5. Aghamiri, S.M.S., Oono, N., Ukai, S. et al. (2018) Microstructure and mechanical properties of mechanically alloyed ODS copper alloy for fusion material application. *J. Nuclear Materials and Energy*, **15**, 17–22. DOI: https://doi.org/10.1016/j.nme.2018.05.019
6. Demchyshyn, A.V., Kulak, L.D., Yavor, V.A. (2021) Structure and mechanical properties of thick metallic condensates strengthened by dispersed particles of various type. *Poroshk. Metalurgiya,* **1–2**, 142–160 [in Ukrainian].
7. Smiryagin, A.P., Smiryagina, N.A., Belova, A.V. (1974) *Commercial nonferrous metals and alloys.* Moscow, Metallurgiya [in Russian].
8. Aksenov, D.A., Asfandiyarov, R.N., Raab, G.I. et al. (2021) Influence of the chromium content in low-alloyed Cu–Cr alloys on the structural changes, phase transformations and properties in equal — channel angular pressing. *J. Metals*, **11**, 1795–1808. DOI: https://doi.org/10.3390/met11111795
9. Marwa Elmahdya, Gamal Abouelmagdb, Asaad Abd Elnaeem Mazenb (2017) Microstructure and properties of Cu–ZrO_2 nanocomposites synthesized by in situ processing. *J. Materials Research*, 21(**1**), 11. DOI: https://10.1590/1980-5373-mr-2017-0387
10. Fathya, A., Elkady, O., Abu-Oqail, A. (2017) Microstructure, mechanical and wear properties of Cu–ZrO_2 nanocomposites. *J. Materials Sci. and Technology*, 33(**17**), 2138–2146.DOI: https://doi.org/10.1080/02670836.2017.1353668

ORCID

A.V. Demchyshyn: 0000-0002-1572-9385,
A.A. Demchyshyn: 0000-0001-7754-0185

CONFLICT OF INTEREST

The Authors declare no conflict of interest

CORRESPONDING AUTHOR

A.V. Demchyshyn
Frantsevich Institute for Problems of Materials Science of the NASU
3 Omelyan Pritsak Str. 03142, Kyiv, Ukraine.
E-mail: ademch@ipms.kiev.ua

SUGGESTED CITATION

A.V. Demchyshyn, A.A. Demchyshyn, S.P. Egorov (2024) Structure and mechanical properties of thick copper condensates, dispersion-strengthened with chromium, zirconium oxide and their mixture. *The Paton Welding J.*, **4**, 32–39.

JOURNAL HOME PAGE

https://patonpublishinghouse.com/eng/journals/tpwj

Received: 04.12.2023
Received in revised form: 22.02.2024
Accepted: 09.05.2024

DOI: https://doi.org/10.37434/tpwj2024.04.06

NUMERICAL ANALYSIS OF THE REGULARITIES OF THE INFUENCE OF PIPE STEEL DEGRADATION ON THE RELIABILITY OF CORRODED MAIN GAS PIPELINES USED FOR TRANSPORTATION OF GAS-HYDROGEN MIXTURES

O.S. Milenin, O.A. Velykoivanenko, G.P. Rozynka, N.I. Pivtorak

E.O. Paton Electric Welding Institute of the NASU
11 Kazymyr Malevych Str., 03150, Kyiv, Ukraine

ABSTRACT

Transportation of mixtures of natural gas and green hydrogen is one of the promising ways to use the local gas-transportation system under the conditions of a rapid transition to a sustainable economy. For safe operation of available main gas pipelines at transportation of gas-hydrogen mixtures of different compositions, it is necessary to take into account the negative influence of hydrogen on the mechanical properties of pipe metal, in particular at evaluation of their technical condition by the results of flaw detection. In this work, the principles of safe operation of pipelines with detected defects of local corrosion loss of metal were studied. For this purpose, a numerical procedure was developed for evaluation of brittle strength based on finite element modeling of the stressed state and brittle-ductile fracture criteria. It is shown that under the conditions of static loading degradation of brittle fracture resistance of pipeline metal with the detected defect of local metal loss is relatively small and it can be compensated by a change in service load. Under the conditions of cyclic loading by internal pressure, the principles of lowering of the load-carrying capacity of a corroded pipeline were demonstrated, depending on the actual brittle fracture resistance of the pipe steel.

KEYWORDS: gas-hydrogen mixtures, main pipeline, local metal loss due to corrosion, hydrogen degradation, technical condition, brittle fracture, cyclic loading

INTRODUCTION

One of the most intensively growing sectors of the modern power engineering is the production and use of green hydrogen as an environmentally friendly alternative to fossil hydrocarbons. In particular, this is reflected in the European Union's Hydrogen Strategy, as well as in similar documents of other countries, where it is planned to maximise the use of hydrogen for industrial, transport or domestic needs, which is a part of the transformation of the global economy according to the principles of sustainable development [1–3]. It is important to emphasise here that hydrogen is not a fuel itself, but an energy carrier from renewable energy sources (solar, wind or hydroelectric power plants, geothermal sources, etc.) or a raw material (for the chemical industry). Therefore, one of the key challenges in implementing such approaches for green energy is the transportation of hydrogen gas. Building a new pipeline system for these needs is a large-scale and expensive infrastructure project. Therefore, it is rational to use existing gas transportation systems (GTS). However, it is known that diffused hydrogen has a negative impact on the service properties of pipe steel structures caused by hydrogen degradation of metal [4, 5]. Therefore, the direct use of main and distribution pipelines for transporting pure hydrogen is objectively complicated.

As one of the practically possible ways to use the existing gas transportation network for the needs of hydrogen energy, the transportation of mixtures of natural gas and green hydrogen is being considered and gradually implemented [6]. Depending on the composition of the mixture, i.e., on the partial pressure of hydrogen, different levels of additional technological measures are envisaged to maintain the serviceability of individual GTS components. First of all, this concerns the selection of acceptable operating modes, procedure for planning measures to monitor the technical condition and expert reliability evaluation. One of the typical tasks is to evaluate the admissibility of operational anomalies in the pipeline geometry detected by means of non-destructive testing during periodic flaw detection. In the event of significant metal hydrogenation of a defective pipeline, the use of standardised static strength evaluation procedures may be limited, in particular, as a result of changing the prevailing mechanisms of microscopic and macroscopic fracture that determine the conditions of the boundary state of a structure. For example, when analysing the acceptability of crack-like defects in pipelines (or anomalies formally schematised as cracks, such as non-metallic inclusions, pitting, grooves, lacks of fusion in welds, etc.), the limiting state of structures under the operational load is determined by the material's resistance to brittle fracture [7]. Therefore, when evaluating the technical condition of pipelines with crack-like anomalies, it is necessary to take into account the change in the values of the material fracture toughness K_{Ic} and strength characteristics included in the corresponding limiting state criteria. In the case of analysing the admissibility of three-dimensional material discontinuities, among which the most common are local corrosion losses of metal, the limiting state of the pipeline is typically determined by the criteria of ductile fracture [8]. However, in case of significant metal embrittlement, the mechanisms of metal fracture initiation and propagation in the anomaly area may change to brittle-ductile or brittle. Therefore, depending on the composition of the transported gas-hydrogen mixture (and the corresponding saturation of pipeline metal with diffused hydrogen), standard limiting state criteria may be of limited applicability.

The aim of this work is to determine the principles of the influence of the level of hydrogen degradation of pipe steel (changes in fracture toughness and resistance to fatigue failure) on the limiting state of the main gas pipeline with a detected geometric anomaly of a local surface metal loss due to corrosion under the brittle-ductile fracture mechanism. For this purpose, a numerical procedure for evaluation of the stress-strain and limiting states of corroded pipelines based on the method of postulated defects was proposed.

As was already mentioned above, one of the most common types of operational damage in underground main pipelines is local corrosion metal losses in the area of protective insulation damage. Such geometric anomalies are typically schematised as semi-elliptical surface pipe wall thinning (Figure 1). The presence of a geometric anomaly causes local non-uniformity of stresses in the pipe cross-section under the influence of internal pressure and the corresponding heterogeneity in the material's tendency to damage initiation. According to general concepts, the limiting state of pressure vessels with three-dimensional metal discontinuity defects is determined by the ductile fracture mechanism, which consists in the initiation and propagation of microscopic porosity during plastic deformation of the material under external load [9]. However, in the case of significant hydrogenation of the pipeline material during the transportation of gas-hydrogen mixtures, the brittle fracture mechanism is more significant, especially in the presence of crack nuclei in the metal.

To determine the principles of the influence of the level of hydrogen degradation of pipe steel on the brittle strength of the pipe in a non-uniform field of mechanical stresses, it is rational to use numerical modelling methods along with the corresponding limiting state criteria. Thus, in this research, numerical analysis was carried out on the basis of a finite element model of an elastic-plastic continuous medium by formulating and solving the corresponding boundary value problem using the WeldPrediction software package [10]. An increment of the strain tensor components was considered as the sum of the increments of elastic $d\varepsilon_{ij}^{e}$ and plastic $d\varepsilon_{ij}^{e}$ components, $i, j = r, \beta, z$ (Figure 1):

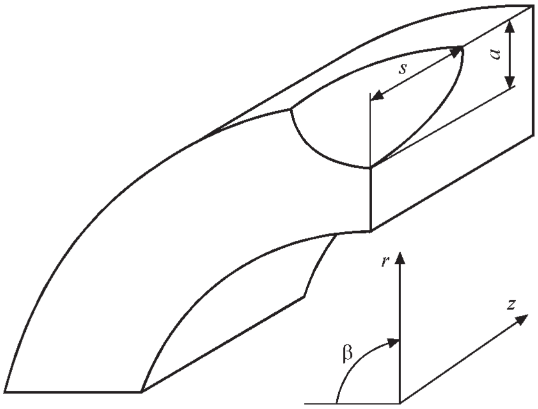

Figure 1. Schematic of pipeline with a surface defect of corrosion wall thinning

$$d\varepsilon_{ij} = d\varepsilon_{ij}^{e} + d\varepsilon_{ij}^{p}. \tag{1}$$

The further analysis of the stress-strain state of the defective pipeline with an increase in the internal pressure was carried out by tracing the accumulation and redistribution of a strain with a gradual increase in loading. During each tracing step, the relationship between the components of the stress (σ_{ij}) and strain (ε_{ij}) tensors was determined using the generalised Hooke's law and the associated plastic flow law [11]:

$$\begin{aligned} \Delta\varepsilon_{ij} &= \Psi\left(\sigma_{ij} - \delta_{ij}\sigma_m\right) + \delta_{ij}K\sigma_m - \\ &-\frac{1}{2G}\left(\sigma_{ij} - \delta_{ij}\sigma_m\right)^{*} + \left(K\sigma_m\right)^{*}, \end{aligned} \tag{2}$$

where δ_{ij} is the Kronecker symbol, $K = (1–2v)/E$, $G = 0.5E/(1+v)$; E is the Young's modulus; v is the Poisson's ratio; the index "*" refers to the variable at the previous step of loading tracing; Ψ is the metal state function, which is determined iteratively based on the actual shape of the yield surface depending on the stress intensity σ_i and yield strength σ_y [11];

$$\begin{aligned} &\Psi = \frac{1}{2G}, \text{ if } \sigma_i < \sigma_y; \\ &\Psi > \frac{1}{2G}, \text{ if } \sigma_i = \sigma_y; \\ &\text{the state } \sigma_i > \sigma_y \text{ is inadmissible.} \end{aligned} \tag{3}$$

At each tracing step, the conditions (3) are implemented, taking into account the history of plastic deformation, including strain hardening.

Simultaneously, at each iteration, the stress field σ_{ij} is calculated for Ψ:

$$\sigma_{ij} = \frac{1}{\Psi}\left(\Delta\varepsilon_{ij} + \delta_{ij}\frac{\Psi - K}{K}\Delta\varepsilon\right) + J_{ij}\,, \qquad (4)$$

where

$$J_{ij} = \frac{1}{\Psi}\left[\left(b_{ij} - \delta_{ij}b\right) + \delta_{ij}K\sigma^*\right],\ \Delta\varepsilon = \Delta\varepsilon_{ii}/3\,,\ b = b_{ii}/3\,.$$

The components of the stress tensor satisfy the equation of statics for inner finite elements (FEs) and the boundary conditions for surface FEs. To form a system of linear algebraic equations for the vector of displacement increments in FE nodes, the following functional is minimised at each step of tracing and iterations by Ψ [11]:

$$L_I = -\frac{1}{2}\sum_V \left(\sigma_{ij} + J_{ij}\right)\Delta\varepsilon_{ij}V_{m,n,r} + \sum_\Theta F_i\Delta\boldsymbol{U}_i\Delta S_P^{m,n,r}, \qquad (5)$$

where $\sum\limits_V$ is the sum operator by inner FEs; $\sum\limits_\Theta$ is the sum operator by FEs over S_p surface, on which the components of the force vector F_i are set. A detailed description of equations (1)–(5) and the software implementation for their solution are given in [12].

The evaluation of the actual reliability of the pipeline under the conditions of varying levels of hydrogen embrittlement of the material under a non-uniform stress field caused by internal pressure and local geometric anomaly was carried out using the postulated defects method. This method assumes the presence of small crack-like defects and the further evaluation of their admissibility. To evaluate the brittle strength of corroded pipelines, taking into account the hydrogen degradation of metal, for each postulated defect, the safety factor n is calculated based on the corresponding internal state criterion for a body with a crack. The typically used criterion is the R6 procedure [13], which is based on a two-parameter brittle-ductile fracture diagram (Figure 2) and can be mathematically described as:

$$nK_r\left(L_r\right) = \begin{cases} \left[1 - 0.14\left(nL_r\right)^2\right]\left\{0.3 + 0.7\exp\left[-0.65\left(nL_r\right)^6\right]\right\}, \\ \text{at } nL_r \le L_{r\max} \\ 0,\ \text{at } nL_r > L_{r\max}. \end{cases}, \qquad (6)$$

where $K_r = K_\mathrm{I}/K_{\mathrm{I}c}$, $L_r = \sigma_\mathrm{ref}/\sigma_\mathrm{y}$; K_I is the stress intensity factor; $K_{\mathrm{I}c}$ is the fracture ductility; σ_ref are the reference stresses. The calculation of K_I and σ_ref is performed according to the algorithms given in [14].

The evaluation of the safety factor n was based on a two-parameter diagram (Figure 2) and consisted of calculating the ratio of the sections' lengths from the beginning of the coordinates to the actual point (K_r, L_r) and its extension to the intersection of the limiting curve.

The use of the developed numerical approach in evaluating the effect of operational load on the corroded element of the main gas pipeline allows not only evaluating the static strength of a structure at different levels of hydrogen degradation, but also taking into account the effect of cyclic loading by internal pressure within the admissible design values. For this purpose, the fatigue growth rate of the postulated cracks was calculated according to the Paris law. If the loading is characterised by a cycle asymmetry with a coefficient R, then the law of growth in crack sizes depending on the number of loading cycles N can be formulated as [15]:

$$\frac{dc}{dN} = \frac{C\left(\Delta K_\mathrm{I}\right)^m}{\left(1 - R\right) - \dfrac{\Delta K_\mathrm{I}}{K_{1c}}}, \qquad (7)$$

where C, m are the Paris coefficients.

Thus, the fatigue growth of postulated cracks under cyclic loading of a pipeline with local corrosion wall thinning and a certain level of hydrogen degradation of metal properties can be quantified by changing the brittle strength safety factor n.

As an example of using the proposed approach, this work considers a typical rectilinear section of a pipeline with a diameter of $D = 1420$ mm and a wall thickness of $t = 20$ mm, the pipe material is X80 pipe steel. Two types of operating loading were analyzed, namely: static internal pressure of the gas-hydrogen mixture (maximum value $P = 7.5$ MPa) and cyclic change of internal pressure in the range of 5.5–7.5 MPa, with a number of up to 1000 cycles. The actual mechanical properties of the pipeline metal depend on the concentration of hydrogen in the transported mixture and the

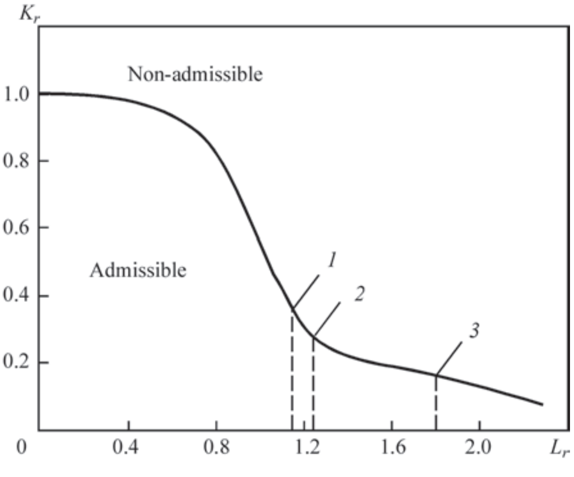

Figure 2. Two-parameter diagram of brittle-ductile fracture of a structure with a crack [13]: *1* — 1.15 (typical low-alloy steels and welded joints); *2* — 1.25 (typical low-carbon steels and austenitic welded joints); *3* — 1.8 (typical austenitic steels)

corresponding level of degradation. According to the available data [16], hydrogen has the most significant negative effect on the resistance of pipe steel to brittle fracture (i.e., a change in K_{1c}) and fatigue failure (which is quantitatively described by changes in the Paris coefficients C and m). At the same time, at a volume concentration of hydrogen in the mixture of up to 50 %, no change in the value of the tensile and yield strength is observed. For pipe steels at hydrogen concentrations in the transported mixture of 5–20 %, Paris coefficients are approximately $C = 2.98 \cdot 10^7$, $m = 2.580$ [17].

As was mentioned above, the size of the postulated crack is an important parameter for the quantitative calculation of pipes for static or fatigue strength. For the considered case, the preliminary calculation showed that when a size of the subsurface elliptical crack is 2.5×0.4 mm, the safety factor of the pipe is approximately 1.92. This conservatively meets the design requirements for the pipeline (1.94). In order to accurately take into account the three-dimensional stress-strain state when calculating the brittle strength, cracks of different orientation relative to the pipe axis (longitudinal, circumferential) were considered, and the minimum safety factor n in the structure cross-section was chosen.

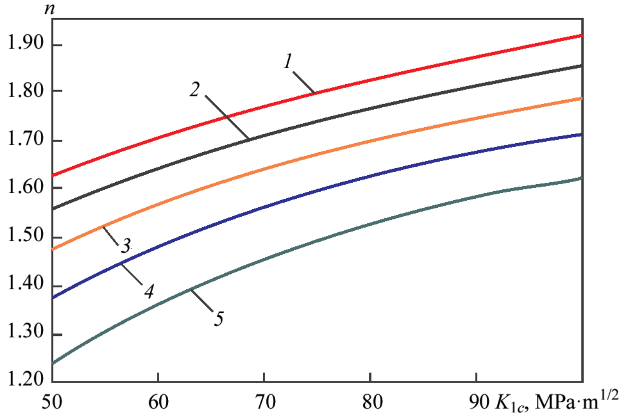

Figure 4. Dependencies of the brittle strength of the pipeline n (1420×20 mm) with local wall thinning ($2s = 200$ mm) at a pressure of $P = 7.5$ MPa on the value of fracture ductility K_{1c} of the material and the depth of the defect α, mm: *1* — 4; *2* — 6; *3* — 8; *4* — 10; *5* —12

The developed numerical approach to determine the brittle strength safety factor was demonstrated on the example of a characteristic defect of local semi-elliptical corrsion wall thinning ($2s = 200$ mm, $a = 4$–12 mm). A comparison was made with standardized algorithms for evaluating the admissibility of such anomalies according to the national standard DSTU-N B V.2.3-21:2008 [18]. This standard is based on the analysis of the residual safety factor of pipelines with local corrosion loss of metal, which makes it appropriate to compare with the proposed calculations. As shown in Figure 3, the correlation between the developed procedure and regulatory requirements is satisfactory.

The results of the numerical analysis of the effect of the the corrosion damage degree (depth of local wall thinning) of the pipeline on its reliability under static loading by internal pressure and at different K_{1c} values are shown in Figure 4. From these data, it can be concluded about the sensitivity of the brittle strength safety factor of the corroded pipeline to the actual fracture toughness of the material at different depths of the corrosion metal loss, which should be taken into account when analysing its serviceability.

Figure 5 shows the calculated dependences of the brittle fracture resistance value on the depth of local wall thinning a for different values of the operating pressure P in the pipeline, the design allowable safety factor $n = 1.617$. These results demonstrate a significant safety factor of corroded gas pipelines when transporting gas-hydrogen mixtures under static loading: in the typical operating pressure ranges of 5.5–

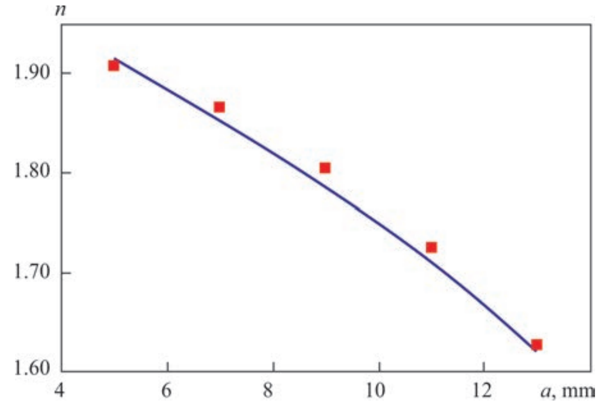

Figure 3. Comparison of the dependence of the brittle strength safety factor n of a pipeline (1420×20 mm) with a defect of local wall thinning ($2s = 100$ mm) on the depth of the defect a calculated by the method of postulated cracks and according to [18]: ■ — according to DSTU-N B V.2.3-21:2008

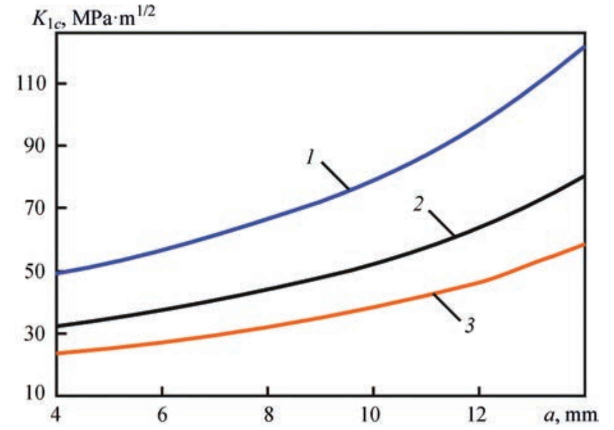

Figure 5. Dependencies of the maximum admissible degradation of the pipeline material (change in K_{1c}) on the depth of the detected local wall thinning a and at different operating pressures P, MPa: *1* — 7.5; *2* — 6.5; *3* —5.5

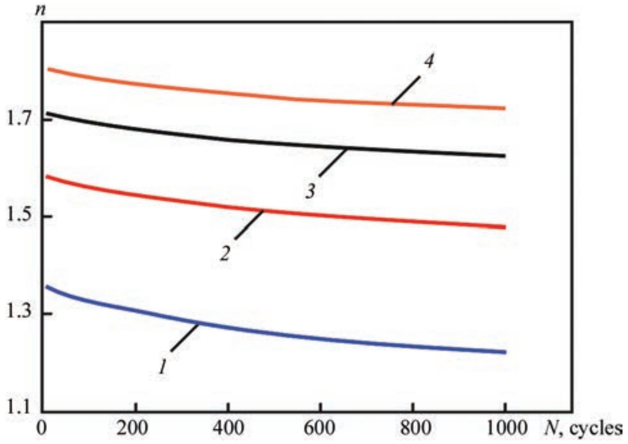

Figure 6. Dependencies of the brittle strength safety factor *n* (1420×20 mm) of a pipeline with a detected defect of local wall thinning ($2s \times a$ = 200×10 mm) on the number of cycles of change in internal pressure from 5.5 to 7.5 MPa and the value of fracture toughness K_{Ic} of the pipe metal, MPa·m$^{1/2}$: *1* — 50; *2* — 75; *3* — 100; *4* — 125

7.5 MPa, a significant reduction in fracture toughness remains acceptable. Thus, the reliability and safety of the operation of a corroded main gas pipeline with a certain level of hydrogen degradation of material properties can be guaranteed by making appropriate adjustments to the operating modes.

For the case of cyclic loading with variable internal pressure (within the design range of 5.5–7.5 MPa), it is necessary to additionally take into account the fatigue growth in the size of postulated cracks. As shown in Figure 6, within 1000 loading cycles, a decrease in the minimum safety factor in the cross-section of the defective pipeline ($2s \times a$ = 200×10 mm) does not exceed 0.2, depending on the value of the fracture ductility K_{Ic}. Therefore, if a particular pipeline has an excessive design strength, the influence of the fatigue mechanism of damage accumulation can be disregarded when evaluating the acceptability of local corrosion-type metal losses.

CONCLUSIONS

1. To predict the reliability of main pipeline elements with geometric anomalies of local semi-elliptical corrosion wall thinning, taking into account the hydrogen degradation of mechanical properties of the material, a numerical procedure for determination of the brittle strength safety factor was proposed. This procedure is based on the finite element analysis of the stress-strain state of the pipeline and the calculation of the brittle strength safety factor based on the postulated cracks method and the two-parameter brittle-ductile fracture criterion. A comparison with the standardised algorithms for evaluating the admissibility of such anomalies in accordance with the national standard DSTU-N B V.2.3-21:2008 was carried out, and a satisfactory correlation between the developed procedure and regulatory requirements was shown.

2. A significant strength safety factor of corroded gas pipelines while transporting gas-hydrogen mixtures under static loading was demonstrated: in the typical ranges of operating pressure of 5.5–7.5 MPa, a decrease in the fracture toughness K_{Ic} remains acceptable. Thus, the reliability and operation safety of a corroded main gas pipeline with a certain level of hydrogen degradation of material properties can be guaranteed by making appropriate adjustments to the operating modes.

3. For the case of cyclic loading with variable internal pressure within the operating range of 5.5–7.5 MPa, fatigue growth in the size of postulated cracks according to the Paris law was additionally taken into account. It is shown that within 1000 loading cycles, a decrease in the minimum safety factor in the cross-section of the defective pipeline (size of thinning defect is 200×10 mm) does not exceed 0.2, depending on the actual value of the fracture toughness K_{Ic}. Therefore, if a particular pipeline has an excessive design strength, the impact of the fatigue mechanism of damage accumulation can be disregarded when evaluating the acceptability of local corrosion-type metal losses.

REFERENCES

1. Aravindan, M., Praveen Kuma, G. (2023) Hydrogen towards sustainable transition: A review of production, economic, environmental impact and scaling factors. *Results in Engineering*, **20**, 101456. DOI: https://doi.org/10.1016/j.rineng.2023.101456
2. Agrawal, D., Mahajan, N., Singh, S.A., Sreedhar, I. (2024) Green hydrogen production pathways for sustainable future with net zero emissions. *Fuel*, **359**, 130131. DOI: https://doi.org/10.1016/j.fuel.2023.130131
3. Falcone, P.M., Hiete, M., Sapio, A. (2021) Hydrogen economy and sustainable development goals: Review and policy insights. *Current Opinion in Green and Sustainable Chemistry*, **31**, 100506. DOI: https://doi.org/10.1016/j.cogsc.2021.100506
4. Zvirko, O. (2022) Anisotropy of hydrogen embrittlement in ferrite-pearlitic steel considering operational degradation. *Procedia Structural Integrity*, **42**, 522–528. DOI: https://doi.org/10.1016/j.prostr.2022.12.066
5. Huakun, W., Tongyao, W., Sheng, Y. et al. (2024) Ductile burst behavior of high pressure X100 steel pipe considering hydrogen damage. *Int. J. of Hydrogen Energy*, **58**, 362–379. DOI: https://doi.org/10.1016/j.ijhydene.2024.01.106
6. *Cakir* Erdener, B., Sergi, B., Guerra, O.J. et al. (2023) A review of technical and regulatory limits for hydrogen blending in natural gas pipelines. *Int. J. of Hydrogen Energy,* 48(**14**), 5595–5617. DOI: https://doi.org/10.1016/j.ijhydene.2022.10.254
7. Makhnenko, V.I., Pochinok, V.E. (2006) *Strength calculation of welded joints with crack-like imperfections*. E.O. Paton Electric Welding Institute, NASU.
8. Zengtao, C., Butcher, C. (2013) *Micromechanics modelling of ductile fracture*. Springer Science + Business Media Dordrecht.
9. Velikoivanenko, E.A., Milenin, A.S., Rozynka, G.F., Pivtorak, N.I. (2016) Simulation of processes of initiation and

propagation of subcritical damage of metal in welded pipeline elements at low-cycle loading. *Tekh. Diagnost. i Nerazrush. Kontrol*, **4**, 14–20 [in Russian].

10. Velikoivanenko, E., Milenin, A., Popov, A. et al. (2019) Methods of numerical forecasting of the working performance of welded structures on computers of hybrid architecture. *Cybernetics and Systems Analysis*, 55(**1**), 117–127. DOI: https://doi.org/10.1007/s10559-019-00117-8
11. Makhnenko, V.I. (2006) *Safe service life of welded joints and assemblies of modern structures*. Kyiv, Naukova Dumka [in Russian].
12. Makhnenko, V.I., Milenin, A.S., Semyonov, A.P. (2007) Mathematical modelling of thermal-deformation processes in braze-welding of butt joints of the titanium-aluminium type. *The Paton Welding J.*, **11**, 5–9.
13. (2013) BS 7910:2013. *Guide to methods for assessing the acceptability of flaws in metallic structures*. BSI Standards Publication.
14. (2016) API 579-1/ASME FFS-1: *Fitness-for-service 2016*. Washington, American Petroleum Institute, American Society of Mechanical Engineers.
15. Zhao, X.-L., Packer, J.A. (2000) *Recommended fatigue design procedure for welded hollow section joints*. IIW Doc. XIII-1772–99/XV-1021–99. Abington Publ., Abington Cambridge UK.
16. Smiyan, O.D. (2018) *Hydrogen and metal fracture of long-term operation objects*. Kyiv, Naukova Dumka [in Ukrainian].
17. Meng, B., Gu, C.H., Zhang, L. et al. (2017) Hydrogen effects on X80 pipeline steel in high-pressure natural gas/hydrogen mixtures. *Int. J. of Hydrogen Energy*, 42(**11**), 7404–7412. DOI: https://doi.org/10.1016/j.ijhydene.2016.05.145
18. (2008) DSTU N B.2.3-21:2008” *Directive. Determination of residual strength of main pipelines with defects*. Kyiv, Minregionbud Ukrainy [in Ukrainian].

ORCID

O.S. Milenin: 0000-0002-9465-7710

CONFLICT OF INTEREST

The Authors declare no conflict of interest

CORRESPONDING AUTHOR

O.S. Milenin
E.O. Paton Electric Welding Institute of the NASU
11 Kazymyr Malevych Str., 03150, Kyiv, Ukraine.
E-mail: asmilenin@ukr.net

SUGGESTED CITATION

O.S. Milenin, O.A. Velykoivanenko, G.P. Rozynka, N.I. Pivtorak (2024) Numerical analysis of the regularities of the infuence of pipe steel degradation on the reliability of corroded main gas pipelines used for transportation of gas-hydrogen mixtures. *The Paton Welding J.*, **4**, 40–45.

JOURNAL HOME PAGE

https://patonpublishinghouse.com/eng/journals/tpwj

Received: 09.02.2024
Received in revised form: 01.03.2024
Accepted: 03.05.2024

DOI: https://doi.org/10.37434/tpwj2024.04.07

AUTOMATED DEFECT DETECTION IN PRINTED CIRCUIT BOARDS BASED ON THE YOLOv5 NEURAL NETWORK

A. Momot, V. Kretsul, O. Muraviov, R. Galagan

National Technical University of Ukraine “Igor Sikorsky Kyiv Polytechnic Institute”
37 Prospect Beresteiskyi (former Peremohy), 03056, Kyiv, Ukraine

ABSTRACT

In this paper, we consider the possibilities of applying the YOLOv5s deep learning model to the task of automating the process of detecting surface defects on printed circuit boards. Modern printed circuit boards are manufactured in large volumes and contain a significant number of elements. The manufacturing process of printed circuit boards is complex, which increases the likelihood of board wiring defects, such as short, open circuits, mouse bites, etc. These defects are superficial and can be detected by visual and optical inspection. Compared to other methods, this type of visual-optical inspection is easier to automate. It is proven that it is promising to use deep learning models to automate the process of detecting objects in images. Modern neural networks can automatically detect surface defects in printed circuit board images with high reliability. The paper considers the class of YOLO models. It is established that the YOLOv5 model has better performance and recognition accuracy than previous modifications. In this study, the YOLOv5s model was implemented and trained to test the effectiveness of this network in the task of automated detection of surface defects on printed circuit boards. The open dataset “PCB Defects” was used for training. A qualitative and quantitative analysis of the performance of the trained network on the test dataset was carried out. It was found that the network can detect surface defects of printed circuit boards with 92.5% reliability in terms of mAP50. Additionally, the results of the recognition of different classes of defects are analyzed and recommendations for further improvement of the system are given. In particular, it is promising to apply augmentation of training data and use a more complex architecture of the deep learning model.

KEYWORDS: PCB defects, object detection, deep learning, YOLOv5

INTRODUCTION

Automation of electronic module production is an important component in the modern production of electronic equipment. Ensuring the quality and reliability of electronic modules is a key stage in this process, and timely detection of defects is an extremely important task. The installation of defective electronic boards in end devices can result in higher overall costs for the production and maintenance of electronic equipment, as well as possible injury to the end user. Therefore, early detection of defects is extremely critical and is essential to ensure the perfect quality and safety of electronic devices.

In today’s environment, there is a tendency to reduce the size of electronic modules and components to make them more compact for the devices in which they will be used. Another important factor is the significant increase of the production of electronic devices. In this regard, there is a need to use the latest methods of automating the process of controlling defects in printed circuit boards. In terms of the optimal combination of information content, speed, and ease of automation, one of the most promising methods for detecting PCB defects is visual and optical inspection.

Visual and optical inspection provides the ability to detect a wide range of surface defects, such as component damage, misalignment or misconnection, soldering defects, and many others. This method provides objective results, which reduces the influence of the human factor. The use of computer vision, image processing algorithms, and machine learning allows the automation of the inspection process with high speed and reliability [1]. Due to this, the method is effectively used in the tasks of quality control of printed circuit boards, even at high production volumes.

Among computer vision methods, one of the most promising is the use of deep learning models. Deep neural networks can achieve high levels of confidence in detecting objects in images [2]. Thanks to the ability of neural networks to learn complex patterns and dependencies, they can effectively cope with the detection of even small and complex defects that can be difficult to identify using traditional methods.

ANALYSIS OF THE PROBLEM

Printed circuit boards are manufactured using a special technology. First, a circuit is designed, which includes components, connection paths, and other elements. This design is then transferred to a base material, which is usually a polymer board. This process creates the physical basis for the components and wires. After the circuit is transferred to the base material, a series of operations are performed to create the PCB. One of the steps is to apply layers of copper to the board. The copper layers form conductive tracks that provide electrical connections between components. After the copper is applied, the board is subjected to an exposure process that allows the contours of the paths and pads to be formed using photosensitive material and masks [3].

After exposure and removal of excess copper layers, the board passes through etching solutions that remove unwanted copper particles. This process allows the formation of clear path and pad outlines, ensuring proper PCB functionality. After etching, other processing steps are carried out, such as mounting component holes, applying a protective layer, and plating the board with solder. These steps provide corrosion protection, increase strength, and add durability to the PCB.

During the production, assembly, and use of printed circuit boards, various types of defects can occur that can affect their functionality and reliability. Conductor defects are among the most common problems on printed circuit boards. The main types of conductor defects are short, open circuit, mouse bite, spur, spurious copper, and missing hole [4]. Since these defects are superficial, they can be detected by visual and optical inspection. Examples of images of some of the listed defects types from the open data sources [5] are shown in Figure 1.

Visual and optical inspection has the important advantage of being an easy to automate process. Thanks to the use of computer vision, image processing algorithms, and machine learning, the software can be developed that can automatically analyze PCB images and detect defects. This significantly reduces the dependence on the human factor, increases the speed and accuracy of control, and reduces the cost of manual work.

The basic principle of deep learning methods is that a neural network is trained on a large set of PCB images that are already labeled with the presence or absence of defects and their positions. Once the training process is complete, the model can automatically analyze new images and perform defect detection. Deep neural networks can be used for a variety of PCB defect detection tasks, such as visual anomaly detection, defect classification, defect detection, and defect region segmentation.

Thus, neural networks are a powerful tool for detecting defects on printed circuit boards. They can learn complex dependencies, automatically identify diagnostic features, and work with large amounts of data. This makes it possible to automate the inspection process to a large extent. The use of neural networks helps to achieve high accuracy and reliability of defect detection, speeds up the inspection process, and reduces production costs.

Paper [6] is devoted to the control of printed circuit boards. The authors consider in detail the problems of quality control of printed circuit boards and propose methods of automated optical inspection to detect defects. The paper begins with an overview of existing methods for controlling defects on printed circuit boards and their limitations. It shows that traditional methods, such as visual inspection, have limited efficiency and can be costly and time-consuming. Therefore, the authors propose the use of automated optical inspection systems based on neural networks to improve the quality and speed of the defect inspection process.

The authors of [7] argue that due to the complexity of the PCB manufacturing environment, most previous work still uses traditional image processing algorithms for automated PCB defect detection. In their work, they proposed an improved approach to PCB defect detection by learning deep discriminant features. This significantly reduced the high requirements for a large data set for the deep learning method.

The results show better performance in defect classification than other traditional methods based on manual feature detection. According to the authors, the proposed method has the highest mean Average Precision (mAP) score of 99.59 %, which is 8 % higher than the second best method based on a combination of Alexnet and SVM. Such a significant increase demonstrates the high efficiency of deep learning in the tasks of detecting surface defects in PCBs. However, in this study, the network was trained on artificially generated training images. Therefore, in a real-world application, the inspection reliability indicators may differ.

Paper [8] argues that traditional algorithms, which are hampered by inefficiency and limited accuracy, do not meet the requirements of modern standards. In contrast, deep learning-based PCB defect detection algorithms demonstrate increased reliability and efficiency. This is

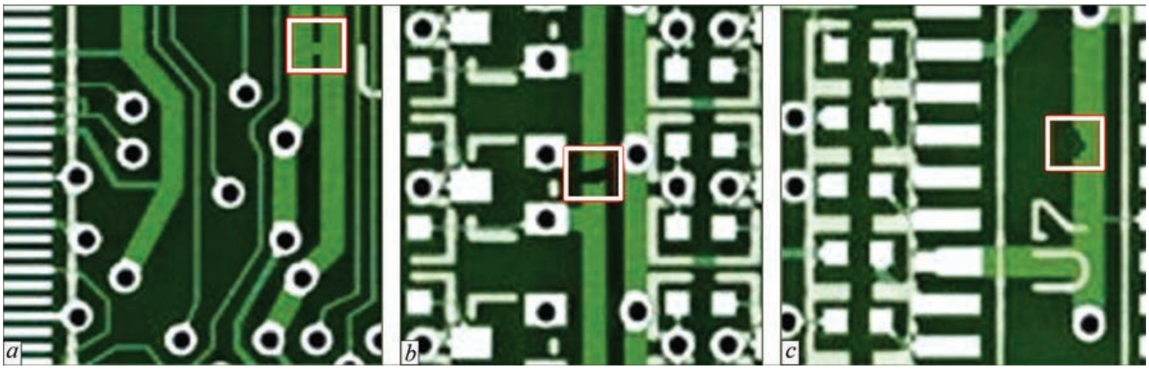

Figure 1. Examples of surface defects on printed circuit boards: *a* — short; *b* — open circuit; *c* — mouse bite

further supported by their ability to learn and recognize new types of defects. The study presents a comprehensive analysis of machine vision-based PCB defect detection algorithms that span the fields of machine and deep learning. The authors note that the introduction of free datasets for PCB defect detection improves the ability to evaluate the effectiveness of algorithms.

According to research, currently, the reliability of detection and correct classification of defects can exceed 95 % mAP with an Intersection over Union (IoU) of 0.5. To potentially improve the results, the authors identified promising areas for future research to solve existing problems in the automation of surface defect detection on printed circuit boards. According to the research results, among the existing deep learning models, the YOLO family of models demonstrates the best efficiency in detecting PCB defects.

In [9], a deep learning algorithm based on the "You Look Only Once" (YOLO) model is proposed for PCB quality control. In the proposed method, skilled quality control engineers first use a video interface to record and label defective PCBs. This data is then used to train a base YOLO model to detect surface defects. In this study, 11,000 training images were used. The neural network proposed by the authors consists of 24 convolutional layers and 2 fully connected layers. The model under consideration achieved a defect detection reliability of 98.79 % in terms of mAP. This result confirms the high efficiency of these models. However, the network architecture considered by the authors is currently outdated. Therefore, there is a need to study more modern modifications of YOLO.

The paper [10] also argues that the traditional method of manual defect detection of printed circuit boards may not meet the required production standards due to the high error rate. In this paper, the authors propose an improved algorithm based on the use of YOLOv4.

The study uses a dataset of PCB defects published by the Peking University Intelligent Robotics Laboratory. This dataset contains a large number of images of different types of defects, which significantly increases the reliability of the model. The authors analyze the distribution of CSPDarkNet53 structural layer features and the distribution of defect sizes in the dataset. At the preprocessing and data entry stage, the image is automatically divided according to the average defect size in the image. This increases the probability that a region contains a defect image. Experimental results show that the improved algorithm based on YOLOv4 has an mAP of 96.88 %.

Despite the benefits, researchers have noted some challenges and limitations of deep learning methods for PCB defect control. For example, the need for a large volume of pre-processed defect images to train models, as well as the difficulty of managing defect diversity and representativeness.

Overall, automated visual and optical inspection using deep learning models is a powerful tool for detecting surface defects on PCBs. Given the rapid progress in machine learning, we can expect further development of this approach for PCB defect inspection. One of the promising areas of research is the use of YOLO family models. These are the models that demonstrate the best results on different training data sets. Of particular interest is the YOLOv5 modification, whose effectiveness in automated PCB defect detection has not been sufficiently covered in scientific publications for today.

STATEMENT OF THE PROBLEM

This study aims to analyze the effectiveness of the YOLOv5 neural network in the task of automated detection of surface defects in printed circuit board images. This approach will allow to detect the location of defects in an automated mode and classify them by type. In a real system, the images of the object under inspection are sent to the intelligent digital processing unit from a special camera installed on the production line or directly above the product. The images are automatically processed by a neural network. The output of the neural network module is an image in which defects are framed and classified by type.

DESCRIPTION OF THE NEURAL NETWORK MODEL

YOLO is a neural network architecture for object detection and classification that has made significant advances in speed and accuracy over its predecessors. One of the main advantages of this model is that it has a high speed of image processing. This allows it to be used for real-time work on mobile devices. In addition, YOLO shows high accuracy in object detection on different datasets. The basic version of the YOLO architecture is described in [11].

However, the initial version of YOLO also has some drawbacks. For example, the architecture may have trouble detecting small objects or objects whose shape may change. There may also be problems with object localization, especially when objects overlap or have similar features. Therefore, this model has a large number of modifications that improve its performance.

YOLOv5 (You Only Look Once version 5) is an updated version of the YOLO algorithm that was introduced in 2020 [12]. YOLOv5 has several model sizes, such as YOLOv5s, YOLOv5m, YOLOv5l, and YOLOv5x, which differ in the number of layers and computing power. For example, the YOLOv5x model has about 88 million parameters. The generalized architecture of YOLOv5 is described in work [13] and shown in Figure 2.

YOLOv5 is also distinguished by its high object detection accuracy. For example, the YOLOv5x model

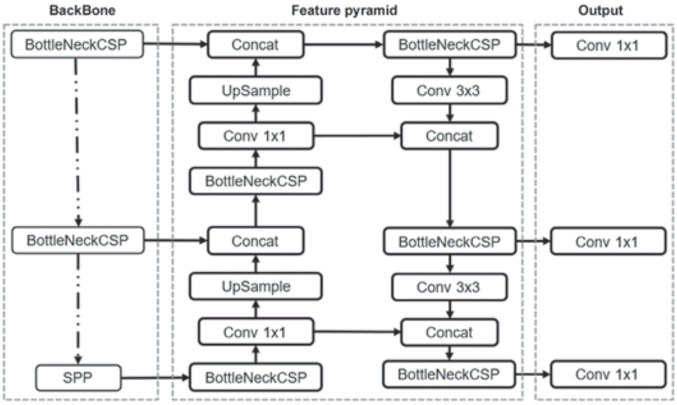

Figure 2. YOLOv5 architecture

achieves about 47 % mAP (Mean Average Precision) on the MS COCO dataset when using a 640×640 resolution and training for 300 epochs. Number of internal parameters: Depends on the model size, from XS (14 million parameters) to XL (177 million parameters). Performance may also vary depending on model size.

The YOLOv5 model uses the Mish activation function. The Mish activation function is a nonlinear function used to introduce nonlinearity in a neural network. It is defined by the following formula:

$$\mathrm{Mish}(x) = x \cdot \tanh(\mathrm{softplus}(x)). \tag{1}$$

The Mish activation function has a smooth gradient, which helps to avoid the problem of gradient decay that can occur in other activation functions such as Sigmoid or ReLU. It also allows more information to be retained in the output signal, which can improve model accuracy.

Compared to YOLOv1 and YOLOv3, YOLOv5 has better speed and accuracy. It also provides a simpler and easier to use architecture, making it a convenient option for developers and researchers. A comparison of the quantitative characteristics of the different YOLO modifications is shown in Table 1. All these models were trained and tested on the MS COCO dataset [14].

To summarise, YOLOv5 is a better choice than previous versions. It strikes a balance between accuracy and performance, making it a popular solution for a variety of object detection tasks.

METRICS FOR OBJECT DETECTION

The following metrics are used to compare and evaluate the performance of object detection algorithms. They help to determine how accurately and completely the objects are detected, as well as how the algorithm handles different object sizes and orientations. Using these metrics, you can assess the quality of the algorithm and compare it with similar solutions. The most popular metrics are IoU, Precision, Recall, mAP50, and mAP50-95 [15]. The value of all these metrics can range from 0 to 1, with 1 being the perfect result.

IoU (Intersection over Union) is a metric used to evaluate the overlap between two regions. In the context of object detection, IoU measures the degree of overlap between the predicted region (the detected object) and the reference region (the ideal or annotated region of the object).

$$\mathrm{IoU} = \frac{\text{Area of overlap}}{\text{Area of union}}. \tag{2}$$

Precision (P) — measures the proportion of objects detected by the algorithm that are correct. It is calculated as the ratio of the number of correctly detected objects to the total number of objects detected by the algorithm. A high P means a small number of incorrectly detected objects.

$$\mathrm{P} = \frac{\mathrm{TP}}{\mathrm{TP} + \mathrm{FP}}, \tag{3}$$

where TP is the number of correctly detected objects, FP is the number of incorrectly detected objects.

Recall (R) — measures the proportion of really present objects detected by the algorithm. It is calculated as the ratio of the number of correctly detected objects to the total number of actual objects. A high R means that the algorithm detects most of the objects.

$$\mathrm{R} = \frac{\mathrm{TP}}{\mathrm{TP} + \mathrm{FN}}, \tag{4}$$

where TP is the number of correctly detected objects, FN is the number of missed objects.

mAP (Mean Average Precision) at a threshold of 50 % IoU (mAP50) — measures the quality of classification of detected objects. mAP50 means that an object is considered to be correctly detected if its overlap with

Table 1. Comparison of YOLO modifications

Parameter	YOLOv1	YOLOv3	YOLOv5
Performance	45–60 FPS	20–30 FPS	20–40 FPS
Hyperparameters	45.0 M	61.0 M	85.0 M
mAP	63 %	57 %	70 %

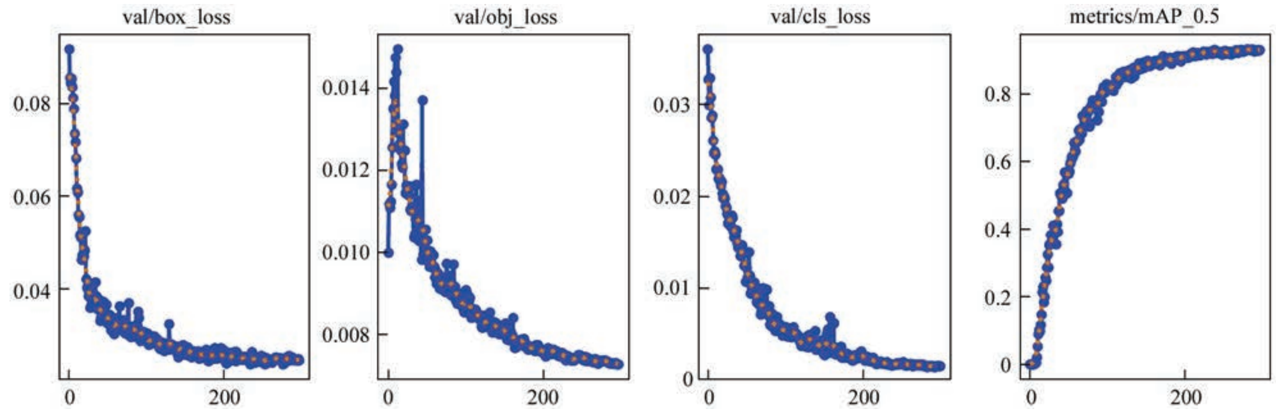

Figure 3. Graphs of the learning process

the predicted boundary (IoU) is at least 50 %. A higher mAP50 indicates better object classification accuracy.

$$\text{mAP50} = \frac{(\text{AP50\_1} + \text{AP50\_2} + \ldots + \text{AP50\_N})}{\text{N}}, \quad (5)$$

where AP is the average Precision across classes.

mAP in the range from 50 to 95 % IoU (mAP50-95) — measures the quality of object detection in the IoU range from 50 to 95 %. It evaluates the algorithm's ability to detect objects consistently at different levels of overlap. A higher mAP50-95 indicates better robustness of the algorithm to changes in object size and orientation.

$$\text{mAP50} - 95 = \\ = \frac{(\text{AP50-95\_1} + \text{AP50-95\_2} + \ldots + \text{AP50-95\_N})}{\text{N}}. \quad (6)$$

DESCRIPTION OF MODEL TRAINING PARAMETERS

The open dataset "PCB defects" was used to train the neural network. The initial dataset consists of 1386 images representing 6 types of defects on printed circuit boards: missing hole, mouse bite, open circuit, short circuit, spur, and parasitic copper. Each type of defect is evenly represented in the dataset, which allows for a variety of tasks related to defect detection. The dataset is described in detail in [5].

However, the original images in this set have too high a resolution. Therefore, it was decided to split each image into 600×600 pixels. The final training set contains 9920 images, while the testing set contains 2508 images.

The neural network is implemented using the PyTorch framework, which is one of the most popular and powerful tools for developing and training neural networks. PyTorch provides flexibility and simplicity in working with tensors, which makes it easy to build, train, and validate a neural network model.

The YOLOv5s model was trained using the following parameters: input image size — 416×416, batch size — 16, number of epochs — 300, weights of the trained model — yolov5s on the MS COCO set. Other hyperparameters are left by default for the base YOLOv5 network.

The learning curves are shown in Figure 3. It can be concluded that the training was completed successfully, with no signs of overlearning.

RESULTS AND DISCUSSION

Examples of the results of the trained network for detecting defects in images from the test set are shown in Figure 4. It can be seen that the network is able to successfully detect defects of different classes and sizes. In particular, even small defects are successfully detected. Since PCB images contain many different structural elements, finding defects manually would take considerable time and require a lot of attention and operator experience. Instead, the processing speed of one image by the neural network was 14.7 ms.

The evaluation of the neural network performance also includes quantitative metrics. The results of quantifying the model's performance on the test set are shown in Table 2.

The YOLOv5s model demonstrated high performance in detecting objects in images. The overall precision (P) is 0.941, which means that most of the detected objects are correct. However, the recall (R) is 0.894, which indicates that some objects may be missed or under-detected.

Among the specific defect classes, the missing hole demonstrates high precision (P = 1.000) and recall (R = 0.997), indicating that the model is able to detect this type of defect. Similar results are observed for the "short" class with precision P = 0.989 and recall R = 0.969. These results confirm the model's effectiveness in recognizing these specific defect classes.

At the same time, some classes, such as "open circuit", "spur" and "spurious copper", show lower precision and recall values. For example, "open circuit" has a value of P = 0.838 and R = 0.800. This may indicate that the model may need additional training or optimization to detect these types of defects.

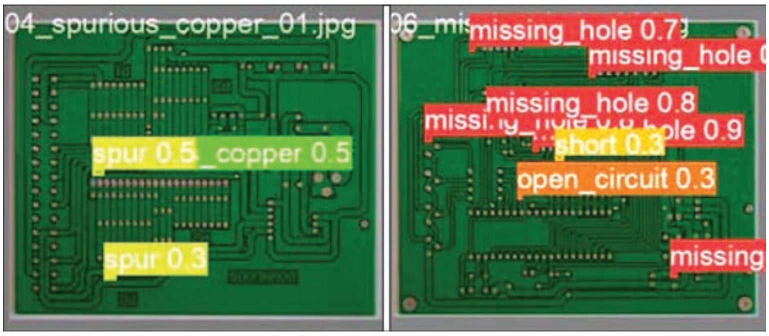

Figure 4. Examples of detecting different classes of defects

Table 2. Results of model evaluation

Defect class	Samples	P	R	mAP50	mAP50-95
All	596	0.941	0.894	0.925	0.459
Missing hole	105	1.000	0.997	0.995	0.561
Mouse bite	104	0.894	0.888	0.918	0.450
Open circuit	100	0.838	0.800	0.884	0.411
Short	90	0.989	0.969	0.981	0.487
Spur	98	0.953	0.829	0.861	0.424
Spurious copper	99	0.970	0.879	0.910	0.424

In addition, the mAP50 and mAP50-95 metrics also indicate the overall reliability of the defect classification. The value of mAP50 is 0.925, which indicates a good ability of the model to classify objects at IoU = 50 %. However, the value of mAP50-95 is 0.459. This means that the model decreases the proportion of correct classifications with increasing IoU.

Taking into account the qualitative evaluation, which shows good quality of object detection in images, and the quantitative evaluation, which indicates the speed and efficient use of resources, we can conclude that the YOLOv5s neural network is highly effective in detecting surface defects in PCB images.

Based on the data presented here, we can also suggest several ways to further develop automated systems for detecting surface defects in printed circuit boards. The first direction is to use more powerful models: It is worth considering the use of more advanced neural network architectures that have high object detection accuracy on standard datasets, such as MS COCO. Potentially, these models can provide better detection quality and the ability to recognize a wider range of objects.

Another area for further research is data augmentation. The use of various augmentation methods will expand the training dataset and improve the model's ability to generalize and recognize defects in different imaging conditions.

Finally, an important task is to optimize the hyperparameters of the selected deep learning model. It is worth conducting additional experiments to investigate the effect of batch size, activation functions, backpacks, and other parameters on the efficiency of defect detection. This will help to find the optimal values in terms of control reliability that will ensure better defect detection quality and model performance.

The choice of specific ways to improve the method of automated surface defect detection of printed circuit boards should depend on the context, resources, and development goals. The result will be influenced by the survey conditions, the characteristics of the object under inspection, the architecture of the deep learning model, etc.

CONCLUSIONS

The paper presents a detailed analysis of the effectiveness of automated detection of surface defects of printed circuit boards using the YOLOv5 neural network. Existing studies confirm the relevance of using artificial intelligence methods to automate the processing of data from visual and optical inspection of printed circuit boards. Compared to previous versions, the YOLOv5 modification has increased performance and reliability of the results.

The considered method of automated detection of surface defects of printed circuit boards based on the YOLOv5 neural network has shown high efficiency. The network is capable of detecting even small defects and classifying them with a reliability of mAP50 = 92.5 %. The study results indicate the system's potential for use in industrial environments. It should also be noted that the model was trained on images captured by a camera with a resolution of 8 MP. The minimum size of defects that the model can detect depends on a large number of factors, such as the shooting conditions, image clarity, model scale, selected model hyperparameters, etc.

The YOLOv5s model in question is the best at detecting critical defects such as hole skipping and short circuits. However, an important defect such as “rupture” is detected with lower reliability. This can be explained by the visual similarity between defective discontinuities and the required track discontinuities provided by the board design. For the same reason, defects such as “excess copper” may not be detected reliably. The “spur” defect is identified with the lowest reliability, but this type of defect does not have a significant impact on the reliability of the board under normal operating conditions. In general, the system under consideration only helps to detect defects in an automated manner. The final diagnostic decision on their criticality and impact on the stability of the board should be made by a qualified specialist.

Automation of visual and optical inspection of printed circuit boards remains an important area of research. The further development of new image processing algorithms, the use of artificial intelligence, and hardware improvements can significantly improve the speed, accuracy, and reliability of the inspection process. The latest YOLOv7 and YOLOX modifications are also currently available and will require further study in the future.

References

1. Steshenko, Y., Momot A., Protasov A., Muraviov O. (2023) Automation of the process of segmentation of images of metal surface defects using the neural network U-Net. *Tekh. Diahnost. ta Neruiniv. Kontrol*, **2**, 34–40 [in Ukrainian]. DOI: https://doi.org/10.37434/tdnk2023.02.05
2. Ling, Q., Isa, N.A. (2023) Printed circuit board defect detection methods based on image processing, machine learning and deep learning: A survey. *IEEE Access*, **11**, 15921–15944 [in English]. DOI: https://doi.org/10.1109/access.2023.3245093
3. Khandpur, R.S. (2006) *Printed circuit boards: Design, fabrication, assembly and testing*. New York, McGraw-Hill.
4. Zhou, Y., Yuan M., Zhang, J. et al. (2023) Review of vision-based defect detection research and its perspectives for printed circuit board. *J. of Manufacturing Systems*, **70**, 557–578. DOI: https://doi.org/10.1016/j.jmsy.2023.08.019
5. Akhatova, A. (2021) *PCB defects*, *Kaggle*. https://www.kaggle.com/datasets/akhatova/pcb-defects
6. Cao, X. (2023) A real-time automated visual inspection system for printed circuit boards missing footprints detection. *Int. J. of Advanced Computer Sci. and Applications,* 14(**5**). DOI: https://doi.org/:10.14569/ijacsa.2023.0140537
7. Zhang, C., Shi W., Li X. et al. (2018) Improved bare PCB defect detection approach based on Deep Feature Learning. *The J. of Eng.*, **16**, 1415–1420. DOI: https://doi.org/:10.1049/joe.2018.8275
8. Chen, X., Wu Y., He X., Ming W. (2023) A comprehensive review of deep learning-based PCB defect detection. *IEEE Access,* **11**, 139017–139038. DOI: https://doi.org/10.1109/access.2023.3339561
9. Adibhatla, V.A., Chih H., Hsu C. et al. (2020) Defect detection in printed circuit boards using you-only-look-once convolutional neural networks. *Electronics*, 9(**9**), 1547. DOI: https://doi.org/10.3390/electronics9091547
10. Xin, H., Chen, Z., Wang, B. (2021) PCB electronic component defect detection method based on improved Yolov4 algorithm. *J. of Physics: Conf. Series*, 1827(**1**), 012167. DOI: https://doi.org/10.1088/1742-6596/1827/1/012167
11. Redmon, J., Divvala S., Girshick R., Farhadi A. (2015) You only look once: Unified, real-time object detection. *Computer Vision and Pattern Recognition*. DOI: https://doi.org/:10.48550/arXiv.1506.02640
12. Zaidi, S.S., Ansari, M., Aslam, A. et al. (2022) A survey of modern deep learning based object detection models. *Digital Signal Processing*, **126**, 103514. DOI: https://doi.org/10.1016/j.dsp.2022.103514
13. Xu, R., Lin, H., Lu, K. et al. (2021) A forest fire detection system based on Ensemble Learning, *Forests*, 12(**2**), 217. DOI: https://doi.org/10.3390/f12020217.
14. Jiang, P., Ergu, D., Liu, F. et al. (2022) A review of YOLO algorithm developments. *Procedia Computer Sci.*, **199**, 1066–1073. DOI: https://doi.org/10.1016/j.procs.2022.01.135
15. Skladchykov, I., Momot, A., Galagan, R. et al. (2022) Application of YOLOX deep learning model for automated object detection on thermograms. *Information Extraction and Proc.*, **50**, 69–77. DOI: https://doi.org/10.15407/vidbir2022.50.069

ORCID

A. Momot: 0000-0001-9092-6699,
V. Kretsul: 0009-0009-3763-1969,
O. Muraviov: 0000-0002-7699-0245,
R. Galagan: 0000-0001-7470-8392

CONFLICT OF INTEREST

The Authors declare no conflict of interest

CORRESPONDING AUTHOR

A. Momot
National Technical University of Ukraine
“Igor Sikorsky Kyiv Polytechnic Institute”
37 Prospect Beresteiskyi (former Peremohy),
03056, Kyiv, Ukraine.
E-mail: drewmomot@gmail.com; asnk@kpi.ua

SUGGESTED CITATION

A. Momot, V. Kretsul, O. Muraviov, R. Galagan
(2024) Automated defect detection in printed circuit boards based on the YOLOv5 neural network.
The Paton Welding J., **4**, 46–52.

JOURNAL HOME PAGE

https://patonpublishinghouse.com/eng/journals/tpwj

Received: 14.03.2024
Received in revised form: 15.04.2024
Accepted: 13.05.2024